Dynamic behavior of correlated electrons in the insulating doped semiconductor Si:P

Inaugural-Dissertation
zur Erlangung des
Doktorgrades der Naturwissenschaften
der Justus-Liebig-Universität Gießen,
Fachbereich 07
(Mathematik und Informatik, Physik,
Geographie)

vorgelegt von

Elvira Ritz

aus Archangelsk

Gießen, März 2009

Dekan   Prof. Dr. Bernd Baumann

I. Berichterstatter: Prof. Dr. Werner Scheid
II. Berichterstatter: Prof. Dr. Dr. h.c. Peter Thomas

Tag der mündlichen Prüfung: 04. Juni 2009

Contents

Chapter 1

Introduction

It is a remarkable fact, that in a material like Si:P, frequently encountered as an academic example for a negatively doped semiconductor and widely employed in the electronics industry, there are still discussions open about the low-energy excitations from the ground state. Crystalline silicon, doped to various levels with phosphorus by established techniques, presents a favorable object of fundamental research in the field of disordered solids. In particular, the influence of electron-electron interactions on the hopping transport in doped semiconductors at temperatures close to zero has attracted much attention since decades [1]-[5]. Beside the electronic correlation effects, critical behavior in the vicinity of the metal-insulator transition (MIT) as $T \rightarrow 0$ is another key issue in the physics of disordered solids [6, 7]. Even in clearly defined systems like heavily doped semiconductors, where disorder stems from the statistical distribution of donor (or acceptor) atoms with concentration n in the single-crystalline host, the behavior of the complex electrical conductivity σ is hardly understood, when the critical donor concentration n_c of the zero-temperature MIT is approached. The direct current conductivity σ_{dc} of doped semiconductors has been well documented on the insulating side of the metal-insulator transition [8, 9]. The temperature-dependent dc conductivity for $n < n_c$ has been observed to follow a variable-range hopping behavior $\sigma_{\mathrm{dc}}(T) = \sigma_0 \exp[-(T_0/T)^m]$, where m is predicted to be 1/4 by Mott [10, 11] for non-interacting electrons and 1/2 by Efros and Shklovskii [2, 12] if one includes electron-electron interactions. The ac conductivity $\sigma(\omega)$ of the insulating doped semiconductors, however, is still not fully understood, and we have focused on this intriguing subject in the course of the present thesis.

At concentrations of phosphorus in silicon below the critical value of $n_c = 3.5 \times 10^{18}$ cm^{-3} [8], the donor electron states are localized due to a disorder in the Anderson sense [2, 6, 11, 13] (in contrast to the extended Bloch states typical of a periodical atomic lattice). This leads to the insulating behavior, defined by the vanishing dc conductivity, $\sigma_{\mathrm{dc}}(T \rightarrow 0) = 0$, as zero temperature is approached. For such a system, theoretical models yielded meaningful analytical formulae for

the $T \to 0$ frequency-dependent response $\sigma(\omega)$ of interacting electrons in the past decades [1, 2, 3, 5]. Compared to the theoretical work done, the experimental data on the ac conductivity of the insulating doped semiconductors still remain scarce and the results, obtained by different groups and in different parameter ranges, lack consistency. Especially the microwave range (with the frequency of electromagnetic radiation from tens of megahertz till tens of gigahertz corresponding to the photon energy from 0.1 μeV to 0.1 meV), best suited to study the Coulomb interaction of the charge carriers, is hardly accessible in an experiment, where the dynamic response $\sigma(\omega)$ at low temperature needs to be studied. Long time, no better means than the resonator technique, a precise method restricted to the fixed frequency of the resonator cavity in use, has been available to measure the frequency-dependent conductivity $\sigma(\omega)$ of doped semiconductors in the gigahertz range. Each frequency point required a different cavity.

At the same time, the rapid development of communication as well as industrial and medicine technologies demands an accurate characterization of components at ever increasing frequencies, beyond the extensively explored radio frequency range, which reaches up to 1 MHz. This becomes, in particular, relevant for insulating and semiconducting materials [5, 14], employed in electronic devices and in low-noise sensors, operating at low temperature. On a macroscopic scale and under steady-state conditions, the interaction of a material with the electric field is determined by the electric conductivity σ_1 and the dielectric permittivity ε_1, both combined in a complex quantity $\sigma = \sigma_1 + i\sigma_2$ (alternatively, $\varepsilon = \varepsilon_1 + i\varepsilon_2$) via the Eq. (2.16). The desired broadband characterization of those parameters becomes quite challenging with rising frequency, because losses and spatial variation of current and voltage then gain importance. To be concrete, we briefly outline here the scope of the arising problems and our solutions to overcome them, developed in the course of the work constituting the present thesis[1].

The material characterization up to the megahertz range turns out to be comparably simple: the voltage drop is measured when a current homogeneously passes through the specimen; lock-in technique allows the determination of the complex response. As soon as the gigahertz range is approached, the wavelength becomes comparable to the leads and specimen dimensions (however, still being four to six orders of magnitude too large to admit optical techniques, based on the free field propagation); waveguides have to be utilized, as shown in Fig. 1.1, and the reflection (or transmission) coefficient is measured [17]. In this spectral range, a vector network analyzer (VNA) is a suited and powerful tool. It allows a phase sensitive measurement of the reflection coefficient Γ, which is directly related to the complex impedance Z of the sample (provided, the transmission

---

[1]Parts of this thesis are already published in our articles in the Journal of Applied Physics [15] and in the Physica Status Solidi C [16].
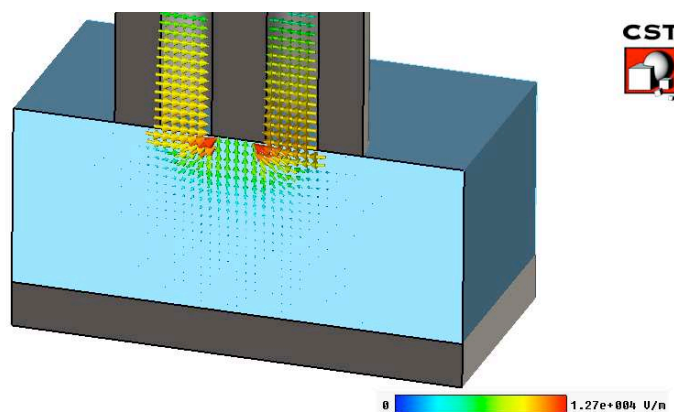
Figure 1.1: Electromagnetic field with the frequency $f = 5$ GHz is guided by a coaxial waveguide to an insulating Si:P sample with dimensions $5 \times 5 \times 2$ mm^3 (as in Fig. 5.2) and with relative dielectric permittivity $\varepsilon_1 = 40$. The sample is mechanically pressed against the probe, as shown in detail in Fig. 3.1. The reflected signal is measured by a vector network analyzer (VNA). The electric field distribution inside the sample is shown at its oscillation maximum. While analytical expressions for the vector field are discussed in Chapter 4, this picture is obtained by a computer simulation using a commercial software CST.

line is properly calibrated).

While the standard circuit theory applies to radio frequencies, in the microwave range, the wavelength becomes as short as a few millimeters and, thus, a careful treatment of the electromagnetic field distribution within the sample is necessary to obtain the material parameters (conductivity and dielectric function) from the impedance Z, gained by the measurement. Whereas the evaluation is straightforward for metallic and superconducting samples under investigation [18]-[20], there is no direct solution in case of an insulating material. This severe complication is due to a non-trivial electromagnetic field distribution inside an insulating sample at the aperture of a coaxial waveguide, as demonstrated in Fig. 1.1 for a semiconducting sample. Only some approximate solutions and models have been developed in the past to treat the dielectric materials [21]-[31], in most cases liquids or soft matter at ambient conditions.

Thus, up to now the powerful technique of measuring the broadband microwave reflection coefficient Γ with a VNA could be successfully applied to determine the complex conductivity $\sigma(\omega)$ of solid samples only in the case of metals or superconductors, while the complicated current distribution inside an insulating semiconductor at low temperature prohibited the data evaluation for that material class. In the course of our work on the present thesis, we revisited the existing approaches to familiar as well as to complementary problems, and

elaborated a complete and rigorous evaluation procedure for such a measurement of an insulating semiconductor with an optimized theoretical and experimental complexity [15]. We applied this developed method to study the complex ac conductivity $\sigma = \sigma_1 + i\sigma_2$ of the doped semiconductor Si:P in the broadband frequency range from 0.1 to 5 GHz, at temperatures of 1.1 K and above, in a broad interval of dopant density n below the metal-insulator transition [16].

With those measurements we have addressed the following issues:

1. Influence of the Coulomb interaction on the hopping transport in the localized donor electron system (i.e. in the insulating regime) at effectively zero temperature. The correlation effects are encoded in a power law α of the dynamic conductivity $\sigma_1(\omega) \sim \omega^\alpha$.

2. It is an additional advantage of a phase sensitive measurement, that the dielectric function $\varepsilon_1(\omega, n)$ is simultaneously obtained from the imaginary part $\sigma_2(\omega, n)$ of the complex conductivity $\sigma(\omega, n)$. The diverging behavior of the donor electron contribution to the dielectric function of the system, as the metal-insulator transition is approached, is a controversial topic in literature, as concerns the scaling exponent of the divergence. With a reflection measurement technique, we are capable of approaching the metal-insulator transition much closer than those predecessors, who measured in transmission with quasioptical techniques in the terahertz range [32]-[34]. While a transmission measurement is suited deep in the insulating regime, it prohibits approaching the MIT by too high losses. On the contrary, measuring the reflection coefficient, we can go close to the critical donor concentration n_c.

3. Behavior of the conductivity and the dielectric function, as the temperature is elevated from 1.1 K.

The contents of this thesis are organized as follows:

In Chapter 2, we summarize the information on the basic research issues outlined above, provided by the theory. We have tried to give in each Section of this Chapter an appropriate reference to the relevant experimental results, those of the other groups and of our own.

In Chapter 3, our experimental techniques are described. We start with a general solid sample, terminating a coaxial waveguide, and give in Sec. 3.1 a brief survey of the established evaluation methods for metallic and superconducting materials. In Sec. 3.2, the problems are formulated, which arise in the case of a sample with nonmetallic conductivity. In Sec. 3.3 we describe the broadband

microwave spectrometer based on a pumped [4]He-bath cryostat, which we constructionally and methodically extended from its original scope [20] to the new material class, the insulating semiconductors, in order to perform the measurements on Si:P reported here. In Sec. 3.4 we present a new broadband microwave spectrometer, based on a pumped [3]He-bath cryostat. In the course of the present work, this new spectrometer was constructed and built up to the first thermal tests with the new microwave measurement insert, which resulted in a significantly lower base temperature of 450 mK, than that (1.1 K) achievable at the [4]He-setup.

Our solution to the data evaluation problem for a broadband reflection coefficient measurement of an insulating semiconductor is presented in Chapter 4. A simple static model for the current distribution inside a semiconducting sample is developed as a first try, which we later proved to be valid in the low-frequency range up to 1 GHz; this is presented in Sec. 4.1. It is followed in Secs. 4.2 and 4.3 by a rigorous solution to the problem, where we made no severe simplifications in a strictly determined parameter range.

Results of our measurements of the insulating Si:P samples are presented and discussed in Chapter 5. In Chapter 6 we give an outlook for the further development of the project of this thesis, in particular concerning the behavior of the system across the metal-insulator transition.

Chapter 2

Theoretical background

2.1 Zero-phonon hopping transport in Si:P

2.1.1 Structure of electronic states

To begin with, we briefly recall the electronic structure of the material under investigation, Si:P. At low temperature most of the electronic properties of a crystalline semiconductor are determined by impurities. (For a detailed treatment of this topic, the standard textbook by Shklovskii and Efros [2] can be consulted, the more general classical work by Mott and Davis [11], as well as an up to date and comprehensive book edited by Baranovski [5].) An impurity can be of either donor or acceptor type. A donor atom is able to donate an electron to the conduction band of the host semiconductor, while an acceptor impurity rather captures one electron from the valence band, leaving a mobile hole behind. In many cases, the type of impurity is merely determined by the relative position of the involved elements in the periodic table.

 Placed in the tetrahedral lattice of the Group IV element silicon, a phosphorus atom has an excess fifth electron, relatively weakly bound to the impurity center by an attractive potential similar to that of a hydrogen atom. The situation is schematically depicted in Fig. 2.1. Due to the screening of the core Coulomb potential by the host semiconductor matrix, the wave function of a donor electron has a spatial extension 10 to 100 times the size of a hydrogen atom. One speaks of a shallow impurity. While it is easily ionized at ambient conditions, the conduction band is inaccessible for donor electrons in the temperature range around 1 K, to which we restrict our considerations. For an isolated impurity, the wave function for the donor electron can be determined in the effective-mass approximation, where the energy spectrum close to the minima of the conduction band in k-space is used to construct the solutions [2]. The resulting electronic wave functions of isolated donors are Bloch functions at the bottom of the conduction band, modulated by large-scale hydrogen-like envelope functions.
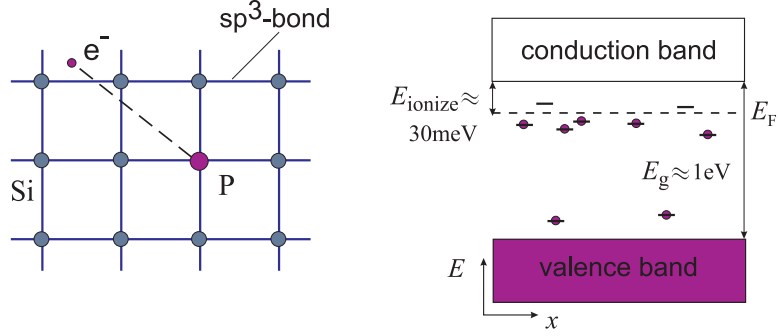
Figure 2.1: Left: a simplified schematic picture of the Si:P crystal, in reality diamond structure. Right: a simplified energy state diagram at $T = 0$; in reality, the bottom of the conduction band and the top of the valence band are bent following the long-range potential of the charged impurity sites. The dashed line depicts the position of the Fermi level, lying in the region of the impurity states in doped semiconductors.

Since P atoms are distributed at random in the host Si crystal, the assembly of the donor electrons exhibits disorder, in contrast to a regular crystalline structure. As a consequence of disorder, at low concentrations of phosphorus in silicon the donor electron functions are localized in Anderson sense [2, 6, 11, 13]. We will return to that subject in more detail in Sec. 2.2.1. The electron probability density of a localized state falls off as $\exp(-r/\xi)$ with the distance r from the donor center. The localization radius ξ determines the characteristic dimensions of the wave function and is of the order of at least 10 times the atomic distance in the host crystal. (The Bohr radius of an isolated donor electron in Si:P is known to lie between $20\,\text{Å}$ and $30\,\text{Å}$, cf. [35]-[37], while the Si atoms in the host Si crystal with diamond structure a just separated by $2.35\,\text{Å}$, corresponding to the lattice constant of $5.43\,\text{Å}$.) At low concentrations of phosphorus in silicon, isolated energy levels are found close to the bottom of the conduction band. Part of them are empty, since there are always some impurities of the opposite type present which accept the neighboring donor electrons, so that hopping transport can take place between the occupied and the empty donor sites, cf. Sec. 2.1.2. The ground state configuration of Si:P is schematically outlined in Fig. 2.1. All impurities are assumed to be fixed in space, but electrons can pass from one site to another, so that the electronic system attains thermodynamic equilibrium determined at $T = 0$ by the condition of minimum electrostatic energy [2],

$$
\begin{aligned}
H_{\text{electrostatic}} \;=\; \frac{e^2}{\varepsilon_1} \Bigg[& \frac{1}{2} \sum_{j}^{\text{don}} \sum_{j' \neq j}^{\text{don}} \frac{(1-p_j)(1-p_{j'})}{r_{jj'}} \\
& - \sum_{j}^{\text{don}} \sum_{k}^{\text{acc}} \frac{1-p_j}{r_{jk}} + \frac{1}{2} \sum_{k}^{\text{acc}} \sum_{k' \neq k}^{\text{acc}} \frac{1}{r_{kk'}} \Bigg],
\end{aligned}
\qquad (2.1)
$$

where ε_1 is the real part of the full dielectric function ε of the Si:P crystal, cf. the Eq. (2.16). p_j is the occupation number for donor j: if the latter is ionized, $p_j = 0$; for a neutral donor $p_j = 1$. Each acceptor captures an electron from a donor and becomes negatively charged, since we assume the number of acceptors N_a to be much less than the number of donors N_d, $N_a/N_d \ll 1$.

At the critical concentration $n_c = 3.5 \times 10^{18} \text{cm}^{-3}$ of phosphorus in silicon [8], the overlap of the localized electronic functions becomes so strong, that they spread out over the entire solid in spite of disorder: transition to a metallic state takes place. While theoretical predictions applicable to the metal-insulator transition in Si:P are subject of Sec. 2.2, the current Section mainly concerns the dynamic transport and effects of electron-electron interactions in a strongly localized system, i.e. relatively far from the MIT. The corresponding experimental results are discussed in Chapter 5.

The Hamiltonian of the system on the insulating side of the MIT can be written as follows (magnetic effects excluded), cf. Ref. [4],

$$
\begin{aligned}
H &= \sum_j E_j a_j^+ a_j + \sum_{j \neq j'} I_{jj'} a_j^+ a_{j'} \\
&+ \sum_j U_j a_{j\uparrow}^+ a_{j\uparrow} a_{j\downarrow}^+ a_{j\downarrow} + \sum_{j < j'} U_{jj'} a_j^+ a_j a_{j'}^+ a_{j'}.
\end{aligned}
\tag{2.2}
$$

Here, a and a^+ are the annihilation and creation operators, respectively, of the local donor electron wave functions which are assumed to be appropriately orthogonalized. The first term describes the energies E_j at the single donor sites j, differing from the energy of an isolated donor E_0 by the influence of the surrounding charged impurities, cf. Eq. (2.1). The second contribution comes from quantum tunneling between j and j', the third term stands for the repulsion between the electrons on the same site (the arrows denote specific spin states), and the last term represents the intersite Coulomb interactions. In the discussion of the hopping transport in Sec. 2.1.2, a strongly localized electron system is concerned at low excitation energies, so that the second term in the Eq. (2.2) becomes negligible while the strong on-site repulsion implies energies outside our range and the third term can be omitted either. On the other hand, close to the metal-insulator transition in Sec. 2.2 the overlap term gains some crucial importance (Anderson transition) and so does the third term (Mott transition), while the long-range Coulomb interaction term four may be neglected.

A useful characteristic of the electron states is the density of states $g(E)$ that can be applied to the description of both ordered solids and solids with arbitrarily strong disorder [38]. The quantity $g(E)\mathrm{d}E$ denotes the number of states in a unit volume, available for an electron with a given spin direction with
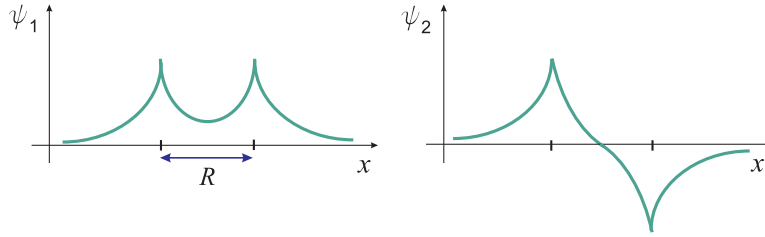
Figure 2.2: In case of energetic degeneracy of two localized quantum states φ_1 and φ_2, two linear combinations of opposite parity are formed. The energy difference of the new states ψ_1 and ψ_2 is proportional to the magnitude of the overlap integral $I(R)$ between the initial wave functions, $|E_1 - E_2| = 2I(R)$.

an energy between E and $E + \mathrm{d}E$. $g(E)f(E)\mathrm{d}E$ is the number of occupied states per unit volume, where f is the Fermi distribution function

$$f(E) = \frac{1}{1 + \exp\{(E - E_F)/k_\mathrm{B}T\}} \, . \tag{2.3}$$

The Fermi energy E_F separates the occupied states from the empty ones at zero temperature. $g(E)$ is defined as a continuous function with finite values also in the energy intervals, where all states are localized. The density of states can be determined experimentally, for instance by scanning tunnelling spectroscopy or by photoemission. The shape of the density of states function in our concrete case of the donor states in the crystalline Si:P sensitively depends on both, the dopant density and the compensation by the acceptor atoms. Therefore we return to $g(E)$, as it is expected from the theory, in more detail further below in Secs. 2.1.2 and 2.2.1, where its knowledge is needed and the underlying experimental situation is clearly set.

2.1.2 Dynamic conductivity

In systems, where the density of states at the Fermi level does not vanish, but electronic states just below E_F are localized, the static conductivity σ_dc vanishes as $T \to 0$ [5, 6, 11]. In other words, such an electronic system is an insulator. Elastic electron tunnelling throughout the solid in an applied static electric field cannot take place, because there will always be a finite energy difference from site to site as long as the corresponding localized wave functions overlap in space. The reason is the Pauli principle, and the mechanism, that prohibits energetic degeneracy of two localized quantum mechanical states, is the formation of two linear combinations of opposite parity and finite energy separation out of them, cf. Fig. 2.2. Let φ_1 and φ_2 be the wave functions of the bound states of two isolated atoms, with an equal energy in the absence of each other. The overlap integral is defined as the matrix element of the full system's Hamiltonian H between both

states,

$$I = \int \varphi_1^*(\vec{x}) H \varphi_2(\vec{x}) \mathrm{d}^3 x \,. \tag{2.4}$$

It is also called transfer integral in literature, since its square is proportional to the transition probability between the states described by φ_1 and φ_2. As long as $I \neq 0$, two superpositions are formed with split energies $|E_1 - E_2| = 2I(R)$,

$$\psi_1 = \frac{1}{\sqrt{2}}(\varphi_1 + \varphi_2)\,, \quad \psi_2 = \frac{1}{\sqrt{2}}(\varphi_1 - \varphi_2)\,. \tag{2.5}$$

In either state ψ_1 and ψ_2 the electron is equally shared by the sites, no matter how big the spatial separation R between them, just because both initial states have identical characteristics. The overlap integral itself decreases with distance R exponentially the same way as the envelope of an isolated state φ_j does,

$$I(R) = I_0 \exp(-R/\xi)\,, \tag{2.6}$$

where ξ is the localization length introduced above.

Since localized eigenstates have discrete energies, transition between them can take place only by inelastic electron tunneling (hopping transport). In the case of direct current, the necessary energy is provided by the interaction with the vibrations of the atomic matrix (phonons), leading to an exponential dependence of electronic transition probabilities to higher energetic levels on temperature [35]. Expressions for thermally activated hopping conductivity in various temperature ranges are treated in detail in the textbooks [2], [11] and [39]. The temperature-dependent dc conductivity of doped crystalline semiconductors at low temperature has also been extensively studied in experiments, being in accord with theoretical predictions. As for the photon-activated hopping transport, the relevant energy range between the radio and the optical frequencies has been technically inaccessible for a long time and experiments still remain scarce, cf. the next Chapter. At the same time, intense interest from the side of the theorists has existed since decades and concrete models yielded analytical and numerical results, without unambiguous experimental information available. That is why our main issue in the present work is the dynamic conductivity $\sigma_1(\omega)$ at effectively zero temperature in Si:P on the insulating side of the metal-insulator transition. Throughout this thesis, the index 1 denotes the real part of the otherwise complex-valued quantity,

$$\sigma_1(\omega) \sim \omega^\alpha\,, \quad \sigma = \sigma_1 + i\sigma_2\,. \tag{2.7}$$

(The imaginary part σ_2 of the complex conductivity is related to the dielectric function ε_1 of the material via the Eq. (2.16) further below.) Encoded in the
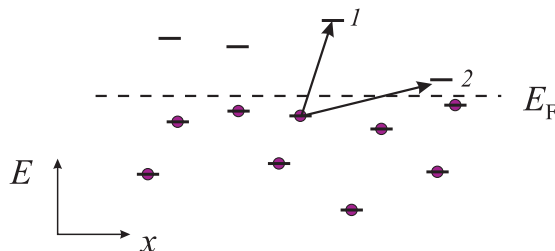
Figure 2.3: Two alternative hopping transitions between occupied and unoccupied states. The dashed line depicts the position of the Fermi level. The first transition corresponds to the nearest-neighbor hopping, the second to the variable-range hopping regime, cf. Ref. [39].

power law of the frequency-dependent conductivity at $T = 0$, there is conclusive information about the influence of electronic correlations on the hopping transport [1, 3]. While at very low frequencies the possibility of several hops during half a period of the ac field must be taken into account (multiple hopping regime, cf. [38]), in the high frequency range, as is the case in our experiment, the so-called pair approximation applies. The theory of resonant photon absorption by pairs of states, one of which is occupied by an electron and the other one is empty, yields distinct limiting results for the conductivity power law in cases, where one of the relevant energy scales of the problem dominates over the others.

For the non-interacting system, where the photon energy prevails over the electronic correlations, Mott was the first to deduce the well-known sub-quadratic frequency dependence of the conductivity [11, 40],

$$\sigma_1(\omega) = \eta e^2 g_F^2 \, \xi \, r_\omega^4 \hbar \omega^2 \,. \tag{2.8}$$

Here, η is a numerical coefficient [1, 11] and g_F is the state density at the Fermi level. The frequency-dependent length r_ω is the most probable hopping distance,

$$r_\omega = \xi \ln(2I_0/\hbar\omega) \,. \tag{2.9}$$

It corresponds to the resonant case $\hbar\omega = 2I(r_\omega) = 2I_0 \exp(-r_\omega/\xi)$, where the energy separation of the hopping partners equals the photon energy, cf. Fig. 2.2 and Eq. (2.6). This means that at low frequencies the most effective pairs for the hopping transport are not necessarily those placed on the neighboring sites, as shown in Fig. 2.3. Charge transport of this kind is called variable-range hopping, it was first introduced by Mott [10, 11, 41]. This term is also used in the case of thermally activated hopping at low temperature, while our focus here is on the photon-activated transport in the zero-phonon regime.

Taking into account the Coulomb repulsion $U(r_\omega)$ if both states in a pair would be occupied by an electron, Shklovskii and Efros corrected the picture of
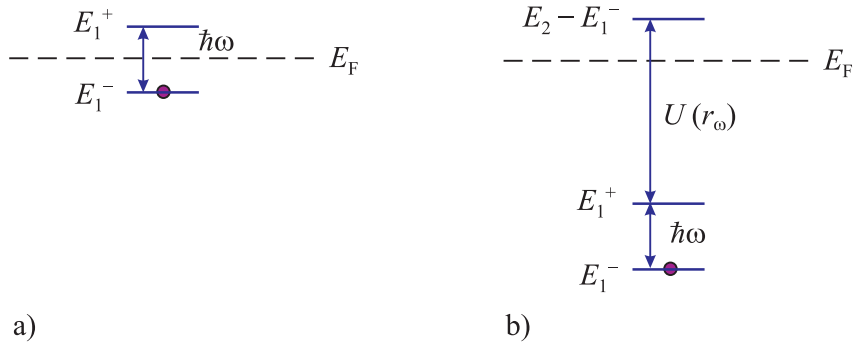
Figure 2.4: Energy scheme of resonant absorption by a pair separated by r_ω, (a) neglecting the Coulomb interaction (Mott's result); (b) accounting for the Coulomb interaction of a second electron in the hopping pair with the first one, after [1]. As a result of this correlation, the energy of the second electron $(E_2 - E_1^-)$ exceeds the final energy E_1^+ of the single electron in the pair by $U(r_\omega) = e^2/\varepsilon_1 r_\omega$.

the energy levels before and after a photon is absorbed (Fig. 2.4) and derived $\sigma_1(\omega)$ to be a sublinear function of frequency, as long as the Coulomb interaction term dominates over the photon energy [1],

$$\sigma_1(\omega) = \eta e^2 g_F^2 \xi \, r_\omega^4 \omega \left[\hbar\omega + U(r_\omega) \right], \qquad (2.10)$$

$$U(r_\omega) = \frac{e^2}{\varepsilon_1 r_\omega} \, .$$

At higher frequencies, in the opposite limit, the sub-quadratic behavior known from Mott (2.8) is recovered. Shklovskii and Efros explain their result as follows. Disregarding the electron-electron interaction, Mott has assumed that the pair has only one electron and, thus, can participate in the absorption only if $E_1^- < E_F$ and $E_1^+ > E_F$, cf. Fig. 2.4 (a). Shklovskii and Efros argue, that the energy of the second electron in a pair $(E_2 - E_1^-)$ needs to lie above E_F in order that there is no second electron in that pair, cf. Fig. 2.4 (b). As a consequence, the final energy E_1^+ of a single electron dips below the Fermi level to a depth up to $U(r_\omega)$, and the level E_1^- to $(\hbar\omega + U(r_\omega))$. This last quantity gives the energy range, over which E_1^- needs to be integrated in the calculation of the transition probability, cf. [1], and, thus, enters as a factor into the final expression for the conductivity (2.10).

In experiments by Helgren et al. [32, 33] and Hering et al. [34], performed on Si:P beyond the microwave range with the quasioptical transmission measurement technique applicable from 50 GHz to a few terahertz, a crossover from a linear to a quadratic frequency dependence of the conductivity σ_1 could be observed. Being in qualitative agreement with the formula (2.10), those experimental data suggest a sharper kink in the crossover region between the interacting and non-interacting regime than the smooth curve described by the analytical
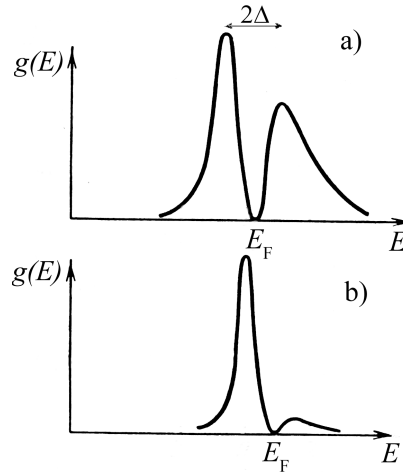
Figure 2.5: Coulomb gap $\triangle$ in the density of the localized donor states at (a) intermediate degree of compensation $N_a/N_d = 0.5$; (b) low degree of compensation $N_a/N_d = 0.1$, after [47].

formula by Shklovskii and Efros. To clarify the issue, Matulewski et al. [42] performed computer simulations on strongly localized electronic system with long-range Coulomb correlations, which do not suffer from approximations necessary in the analytical description. The simulation results exhibit a crossover from a linear to a quadratic dependence of the conductivity $\sigma_1(\omega)$, which is stronger than predicted by Efros and Shklovskii, but quite well reproduces the results of the experiment performed by Helgren et al. [32, 33].

An unresolved issue we have addressed with our experiment, cf. Chapter 5, is that of the conductivity power law in the interacting regime. While a slightly sublinear frequency dependence $\sigma_1(\omega) \sim \omega^\alpha$, $\alpha < 1$ follows for interacting electrons from the Eq. (2.10) (going over into a slightly subquadratic dependence at higher frequencies), most of the few reported experiments in the zero-phonon regime documented a slightly superlinear conductivity power law $\alpha > 1$ [34, 43, 44]. This indicates the importance of the following effect, also analytically accounted for by Shklovski and Efros [1]:

The formula (2.10) implies an assumption that the density of states g_F is energy-independent in the vicinity of the Fermi level. However, Pollak [45] and Efros and Shklovskii [12] have predicted that the long-range electron-electron interaction reduces the density of states at E_F at low temperatures, forming the so-called Coulomb gap $\triangle$. If localized states participating in the hopping transport fall inside this energy region, the frequency dependence of the conductivity is further modified and is described by the Eq. (2.15) as proposed by Shklovskii and Efros [1]. Using simple semi-quantitative arguments, Efros and Shklovskii

[12] suggested a parabolic shape for the Coulomb gap, cf. Eq. (2.13) further below. At low, but not vanishingly low degrees of compensation $K = N_a/N_d$, there is no small parameter for an analytical treatment of the problem and one has to use computer simulations. Baranovski et al. [46] proposed the first successful simulation method, where the total energy is directly minimized with respect to one-electron transitions. This, in turn, made it possible to calculate the impurity band of a real semiconductor in a wide range of degrees of compensation [47]. In Fig. 2.5 the result of those calculations for $g(E)$ is shown for $K = 0.1$ and $K = 0.5$.

The reason for the emergence of the Coulomb gap lies in the definition of the states below E_F as all filled in the ground state and the calculation of those above E_F under this condition, while in reality an empty site is left behind in a hopping process. Writing down the photon energy, necessary for an electron to hop from the donor level E_1^- below E_F to the empty level $(E_2 - E_1^-)$ above the Fermi energy (cf. Fig. 2.4 (b)),

$$\hbar\omega = (E_2 - E_1^-) - E_1^- - e^2/(\varepsilon_1 r) \overset{!}{>} 0 \,, \tag{2.11}$$

we have to subtract the electronic repulsion energy $e^2/\varepsilon_1 r$. The latter is redundant in the expression for $\hbar\omega$, because the energy $(E_2 - E_1^-)$ had been calculated under the assumption of the level E_1^- also being occupied after the absorption of the photon, in other words under ground state assumption which is violated by the hopping process.
From the requirement that the absorbed photon energy be positive we obtain the inequality,

$$r \overset{!}{>} \frac{e^2}{\varepsilon_1((E_2 - E_1^-) - E_1^-)} \,. \tag{2.12}$$

It is this inequality, which gives rise to the Coulomb gap in the density of states $g(E)$. It follows from the Eq. (2.12) that states, which are close to the Fermi level from different sides, must be located at a considerable distance apart from each other. In particular, for states converging to E_F, $((E_2 - E_1^-) - E_1^-) \to 0$, the spatial separation r diverges and, thus, $g(E_F)$ vanishes. Carrying this reasoning forward, Efros and Shklovskii [12] suggested the following formula for the Coulomb gap in three dimensions (as we have it in our case of Si:P),

$$g(E) = \frac{\alpha_3 \varepsilon_1^3 (E - E_F)^2}{e^6} \,. \tag{2.13}$$

Here, α_3 is a numerical coefficient, evaluated in the computer experiments [46] to be $\alpha_3 = 3/\pi$. The width Δ of the Coulomb gap in three dimensions directly follows from setting the right-hand side of the Eq. (2.13) equal to the unperturbed density of states g_0,

$$\triangle = \frac{e^3 g_0^{1/2}}{\varepsilon_1^{3/2}} \,. \tag{2.14}$$
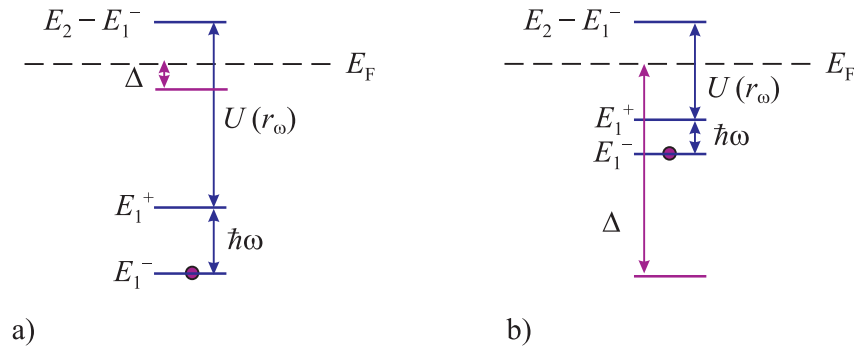
Figure 2.6: Energy scheme of resonant absorption by a pair separated by r_ω in the presence of the Coulomb gap. (a) the gap width $\triangle$ is small compared to the Coulomb interaction energy $U(r_\omega)$; (b) the Coulomb term $U(r_\omega)$ falls inside the gap.

While the density of the donor electron states vanishes at the Fermi level at low temperatures, with rising temperature the Coulomb gap is expected to disappear. This is known from theoretical studies both by analytical calculations and by computer simulations [39, 48], verified by measurements of the integrated density of states in Si:As which contain an indirect but clear-cut information on $g(E, T)$.

The above arguments refer only to systems with localized electronic states, and no Coulomb gap is formed in good metals [2]. However, as was shown by Altshuler and Aronov [49], in disordered metals the density of states has a minimum at the Fermi level. This minimum is associated with the electron-electron interaction and its depth increases with the amount of disorder. If the system's disorder grows so large that electronic states become localized, cf. Sec. 2.2.1 further below, then $g(E)$ vanishes at E_F and the dip turns into the Coulomb gap. A survey of experimental and theoretical work on the problem of Coulomb interactions in a Mott-Anderson insulator (see Sec. 2.2.1 for the latter term) is presented for instance in Ref. [4].

The Coulomb gap has been, for instance, measured in Si:B with varying boron-doping around the metal-insulator transition, using electron tunnelling experiments [50]. In all insulating samples at low temperature ($T \leq 1.2$ K), the quadratic dependence of $g(E)$ on energy has been confirmed, and the full width of the parabolic Coulomb gap $2\triangle$ has been determined which has values around 1 meV.

As concerns the dynamic conductivity at low temperature, no effect on $\sigma_1(\omega)$ is expected, as long as $U(r_\omega)$ largely exceeds the gap width $\triangle$, i.e. as long as the states participating in the hopping transport lie outside the Coulomb gap, cf. Fig. 2.6 (a). In contrast to that, for the conductivity of interacting electrons,

where the Coulomb term $U(r_\omega)$ dominates over the photon energy but falls inside the Coulomb gap as in Fig. 2.6 (b), the reduction of the density of states leads to a stronger, slightly superlinear power law [1],

$$\sigma_1(\omega) \sim \omega / \ln(2I_0/\hbar\omega) \,. \tag{2.15}$$

2.1.3 Dielectric function

It is an additional advantage of a phase sensitive measurement to gain the dielectric function (or dielectric permittivity) ε_1 from the imaginary part of the complex conductivity $\sigma = \sigma_1 + i\sigma_2$ [18, 51] [1,2],

$$\varepsilon = \varepsilon_1 + i\varepsilon_2 = 1 + i\frac{\sigma}{\varepsilon_0\omega} \,. \tag{2.16}$$

We denote by ε the full complex dielectric function of Si:P, relative to the permittivity ε_0 of vacuum, and use the SI units throughout this text. As the MIT is approached upon doping n, the localization radius ξ diverges as a power law in $(n_c - n)$ [2],

$$\xi \sim |n - n_c|^{-\nu} \,. \tag{2.17}$$

As a consequence, the electronic contribution to the dielectric constant $\varepsilon_1(\omega = 0, n)$ is also expected to diverge following a power law when the MIT is approached [55],

$$\varepsilon_1 - \varepsilon_{\mathrm{Si}} \sim |n - n_c|^{-\zeta} \,, \tag{2.18}$$

where $\varepsilon_{\mathrm{Si}} = 11.7$ is the dielectric constant of the host material Si [56].

Mott and Davis [7] put forward microscopic arguments for the divergence of the dielectric constant near the metal-insulator threshold. Dubrov et al. [57] studied a classical percolation[3] transition in a two-component system with metallic and dielectric parts. Using the effective medium approximation, they obtained the formula (2.18) with the exponent $\zeta = 1$, independent of space dimensionality. Their qualitative interpretation of this phenomenon is as follows. Near the metal-non-metal transition, approached from the non-metallic side, the metallic clusters are separated by thin dielectric regions. Each pair of nearest clusters thus forms

---

[1]Gaussian (cgs) units are employed in the references [18] and [51] , while we hold to the SI (mks) system throughout the whole text.

[2]We hold to the convention $\exp[i(\vec{k}\vec{x} - \omega t)]$ in the integrand of the Fourier transformed of the electromagnetic field in accordance with Refs. [18], [51]-[53]. The opposite sign convention is used in Refs. [17, 25, 54] and by the network analyzer. For detailed comparison of both sign conventions see Appendix A.

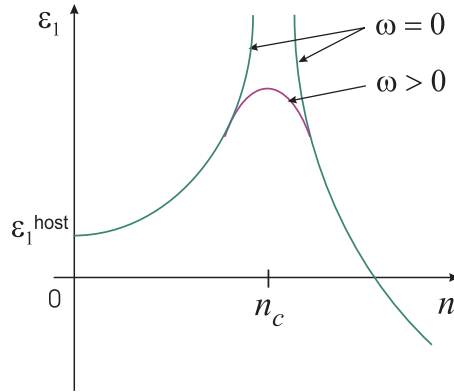[3]The term percolation is explained at the end of the Sec. 2.2.1.

Figure 2.7: Dielectric function $\varepsilon_1(\omega, n)$ in a system consisting of randomly distributed metallic and dielectric regions, after Ref. [55]. n denotes the fraction of the metallic regions, n_c is the percolation threshold, corresponding to the metal-insulator transition. $\varepsilon_1^{\text{host}}$ is the dielectric constant of the purely dielectric system with $n = 0$. For $\omega = 0$ the dielectric constant $\varepsilon_1(0, n)$ diverges at n_c, at a finite frequency $\omega > 0$ the dielectric function $\varepsilon_1(\omega, n)$ is a continuous function of n in the transition point n_c.

a capacitor whose effective surface tends to infinity, resulting in the diverging effective capacity of the whole system. Efros and Shklovskii [55] showed that the dielectric constant diverges near the percolation threshold and determined the critical indices to be $\zeta_3 \approx 1$ in three dimensions and $\zeta_2 = 1.3$ in 2D, without the restrictive use of the effective medium approximation.

For any small but non-zero value of frequency ω, the dielectric function is expected to have a finite value at the transition point n_c and $\varepsilon_1(\omega, n)$ is expected to be a continuous function of the driving parameter n, as Efros and Shklovskii showed [55]. In Fig. 2.7 this is demonstrated at the example of a model system consisting of randomly distributed metallic and dielectric regions, where n denotes the fraction of the metallic regions. At the critical value n_c the percolation threshold in this system is reached, corresponding to the metal-insulator transition. Although there is no divergence for the dielectric function $\varepsilon_1(\omega, n)$ at a finite frequency $\omega > 0$, the Eq. (2.18) stays valid as long as the following inequality holds [55],

$$\varepsilon_1(\omega, n) \ll \varepsilon_1(\omega, n_c). \tag{2.19}$$

Thus, analysis of the high-frequency measurements of the dielectric function (like those in Refs. [33, 34] measured in the terahertz range, as well as our results reported in Chapter 5) allows interpretation via Eq. (2.18) as long as the donor concentrations n in Si:P are not too close to the critical value n_c in the sense of the Eq. (2.19) and the Fig. 2.7. To study the divergence of the dielectric constant $\varepsilon_1(\omega = 0, n)$ more precisely, the frequency range should be further lowered

(cf. e.g. the standard textbook by Dressel and Grüner [18]).

Efros and Shklovskii [55] pointed out, that the scaling laws for the dielectric function (2.18) and the conductivity on both sides of a metal-insulator transition, as well as universal (i.e. dependent only on space dimensions number) relations connecting the corresponding critical exponents can be established more generally, from the assumption of the regularity of the complex conductivity as a function of the driving parameter n and from the Kramers-Kronig relations. However, the numerical values for the relevant exponents are only known for the two-component systems with a percolation threshold, or from the experiments, cf. Chapter 5.

2.2   Metal-Insulator Transition in Si:P

As mentioned at the beginning of the Chapter, at low dopant densities $n \ll n_c$ the donor electron states in Si:P are bound in the vicinity of each impurity center, while at high doping $n \gg n_c$ the wave functions spread over the whole solid without decay. Driving the system through the critical value n_c brings about a transition from an insulating to a metallic state[4] [2, 6, 11, 13], [58]-[60]. In the current Section, we take a closer look at what happens to the donor electron functions while the system is tuned through the critical donor concentration.

Suppose first, impurities were not randomly distributed in the silicon crystal, i.e. phosphorus atoms would form a regular crystal lattice (impurity sublattice) with a much larger period R than the host lattice constant. In a perfect crystal with a periodic potential, electronic wave functions are of the Bloch form,

$$\psi_{\vec{k},m} = u_{\vec{k},m}(\vec{x}) \exp(i\vec{k}\vec{x}), \tag{2.20}$$

where $u_{\vec{k},m}(\vec{x})$ has the periodicity of the lattice, m is the band index and the wave vector $\vec{k}$ is the crystal momentum of the electron. Introducing disorder into the crystal structure is one of the ways to reduce the mean free path l of the electrons. As was first emphasized by Ioffe und Regel [61], there is a lower limit for the mean free path value l for a given crystal momentum k, since the inequality $kl < 1$ would be forbidden by the uncertainty principle, or l cannot become less than the de Broglie wavelength. In other words, sufficient disorder results in

---

[4]At the absolute zero of temperature, the metal-insulator transition in such a system is restricted to the one critical value n_c of the driving parameter n. This is the case considered in the current Section; it is appropriate in the scope of the current thesis, which is mainly concerned with the insulating phase of Si:P at effectively zero temperature (see Chapter 5 further below). At elevated temperature, the metal-insulator transition becomes gradual. Nevertheless, those thermal effects only become relevant if the critical donor concentration n_c is approached more closely (see Chapter 6).

characteristic solutions of the Schrödinger equation, which are substantially different from the Bloch functions (2.20) having characteristic quantum numbers $\vec{k}$. Those states are localized, or trapped in space, with the consequence that elastic electron tunnelling throughout the solid, necessary for a non-vanishing $T = 0$ dc conductivity, is not possible for them, cf. Sec. 2.1.2 above. Anderson [13] was the first to prove the absence of diffusion in certain random lattices and to give a quantitative criterion for localization.

The electron energy spectrum of noncrystalline materials is known to retain characteristic features of the band spectrum known from crystals: regions of high electron density of states correspond to the bands in a crystalline solid [38]. As Mott pointed out, the degree of disorder can be different for electron states with different energies, so that extended and localized states may coexist in the same system at different energies. Typically, the states in the middle of the band remain extended, while those states near the band edges are localized due to disorder. Following Mott [40], one may introduce the energy E_c that separates extended from localized states and plays the role of a localization threshold, it is called mobility edge. A metal-insulator transition in a disordered material occurs as the Fermi energy E_F crosses the mobility edge E_c passing from the extended to the localized states, as shown in Fig. 2.9.

Since we study a three-dimensional system, we always implicitly mean 3D, in all the models discussed. Anderson's result is strictly applicable only to the three-dimensional case. We briefly comment on the known deviations in case of lower dimensions at the end of Sec. 2.2.1. The presence of the Coulomb gap $\triangle$ in the density of localized donor states, described in Sec. 2.1.2, is omitted in the current Section for the reason that $\triangle$ closes as the metal-insulator transition is approached from the insulating side, cf. Eqs. (2.14) and (2.18).

2.2.1   Anderson localization and Anderson transition

It is a common way to treat the problem of electronic localization in disordered solids [2, 11, 13] starting with the tight-binding method [51, 62, 63] for an artificially periodic impurity sublattice. The hydrogen-like potentials of N isolated donor centers are thought of as arranged at equal distances in space, while the overlap $I(R)$ between the ground state wave functions remains small. In such a case, considering just the ground state with the energy value E_0 at each site is sufficient to construct the ground state band. Since the particular shape of the attractive potentials is not crucial for the localization property, they can be approximated by potential wells, as shown in Fig. 2.8. Such an arrangement results in an effective periodic single-electron potential for the Hamiltonian for each of the N electrons. Solutions of the Schrödinger equation in the Bloch form (2.20) are constructed as superpositions of the single-site wave functions. The energies
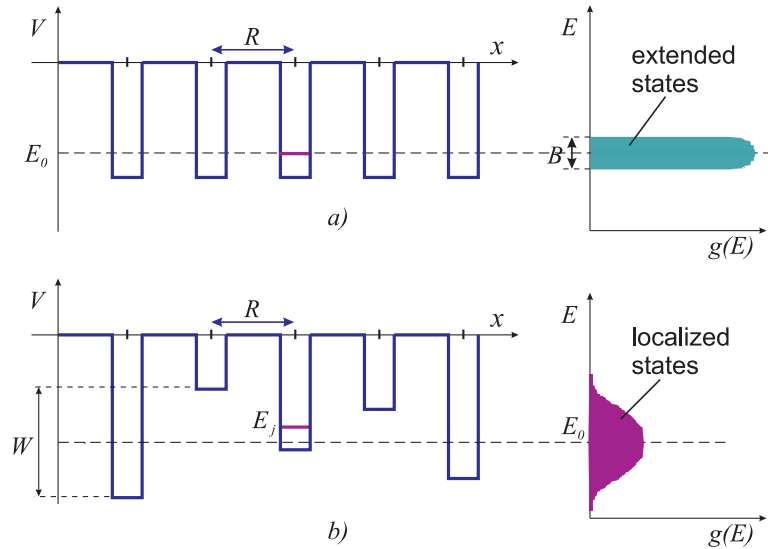
Figure 2.8: Potential wells and the density of states $g(E)$ for a crystalline lattice (a) and for the Anderson lattice at a high degree of disorder, when all states are localized (b).

to the N possible essentially different values of the $\vec{k}$-vector partially split [51],

$$E_{\vec{k}} = E_0 + 2I(R)(\cos k_x R + \cos k_y R + \cos k_z R). \qquad (2.21)$$

A narrow band of delocalized states with the width $B = 12\,I(R)$ forms in place of the initially localized identical states with energy E_0, as depicted in Fig. 2.8 (a). As the impurity center separation R is reduced, the band width B exponentially broadens proportionally to the overlap integral $I(R)$, cf. Eq. (2.6).

So far we have left aside those states, available on each impurity site for the second (missing) electron with the opposite spin orientation. They give rise to an empty band, that forms around the energy value $E_0 + U_0$, where U_0 is the on-site Coulomb repulsion in case two electrons occupy an isolated donor center. (We should note, that this on-site interaction energy is orders of magnitude larger than the long-range Coulomb interaction $U(r_\omega)$ between two electrons on two different donor sites separated by the hopping distance r_ω, discussed in Sec. 2.1.2.) As long as those two bands do not overlap, the hypothetic regular crystalline system just described stays as insulator. But as a consequence of further increased overlap $I(R)$ with growing donor concentration n, both bands at some point merge into one, producing a half-filled band and, thus, metallic conduction. This limiting case of the metal-insulator transition, that takes the on-site Coulomb repulsion into account but leaves disorder apart, is known as the Mott transition, cf. for instance Ref. [2]. It is usually studied with the help of the Hubbard model, in

which electrons repel each other only if they are located at the same site, and the sites are periodically arranged in space. In our work, we apply the complementary model for the metal-insulator transition in a doped semiconductor, developed by Anderson. Following Anderson, we assume the upper Hubbard band to be out of reach on our energy scales, and concentrate on disorder, that can effectively be tuned by the donor concentration n (i.e by the overlap $I(R)$, see the Anderson effective disorder parameter W/I further below). The real transition will have features of both idealized models, cf. Ref. [4], and is sometimes termed the Mott-Anderson transition in literature. In both models, the excitation energy for the electron transport in the insulating phase continuously vanishes on approaching the transition point, which establishes a continuous, or second order phase transition [64].

Now we turn to Anderson's model for a disordered solid. There are two types of disorder present in the assembly of the impurity states. First, the "impurity sublattice" lacks periodicity, for the donor atoms are distributed at random in space. Second, the potentials experienced by the donor electrons at different centers are not identical, as a consequence of the irregular arrangement of surrounding donors and acceptors. To get along with the mathematical treatment of such a sophisticated system, Anderson maintained the periodicity in the positions of the potential wells, but let their depths vary at random, as shown in Fig. 2.8 (b). The energy distribution of the ground states E_j at the single sites j is assumed to be uniform in some interval W around the mean value E_0 of an isolated donor; i.e., the distribution function $P(E_j)$ is of the form

$$P(E_j) = \left\{ \begin{array}{ll} 1/W \,, & |E_j - E_0| < W/2 \,, \\ 0 \,, & |E_j - E_0| > W/2 \,. \end{array} \right.$$

The system's Hamiltonian in the site representation,

$$H_{\text{Anderson}} = \sum_{j=1}^{N} E_j a_j^+ a_j + \sum_{j=1}^{N} I(a_j^+ a_{j+1} + a_j^+ a_{j-1}) \,, \tag{2.22}$$

consists of the electron energies on the single donor centers plus the energy overlaps between the neighboring sites, denoted by I for brevity (it corresponds to $I(R)$ from above). Unfortunately, Anderson's model does not admit of an exact solution, in spite of the simplifications. Nevertheless, he managed do launch two reliable mathematical tools to analyze such a problem, that yield at least an undoubtedly reliable qualitative understanding of the phenomenon of localization, supported by results gained from computer experiments.

Anderson was the first to introduce a mathematical criterion, that allows to distinguish a localized electronic state from an extended, this alone being already a non-trivial step. Anderson's condition is the following. Suppose, at time
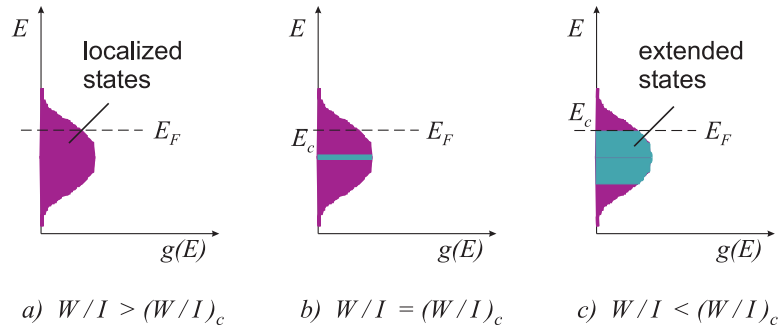
Figure 2.9: Anderson localization and Anderson transition in 3D. (a): If disorder is high, all electronic wave functions are all localized. (b): With decreasing disorder, the critical value of the disorder parameter $(W/I)_c$ is first reached by those states with the highest state density: a narrow band of extended states forms at the peak of $g(E)$. (c) Transition to a metallic state takes place as soon as the mobility edge E_c crosses the Fermi level, at the critical dopant concentration n_c in Si:P. In the middle of the band the disorder parameter W/I is already far below its critical value $(W/I)_c$.

$t = 0$ the electron wave function coincides with the wave function of the single donor center with the index j. Since this is not an eigenstate of the full system's Hamiltonian given by (2.22), the probability density of the electron will change with time. The absolute value squared $|\Psi_j(t)|^2$ of the wave function at large t would be obtained by solving the Schrödinger equation. If states are not localized, the initial wave packets spread out over the infinite system and one would have $\lim_{t\to\infty} |\Psi_j(t)|^2 = 0$. If, however, the wave function is localized, no spreading occurs, and the initial wave function only acquires "tails" on neighboring sites with exponentially small amplitudes. At all times the electron will remain localized in approximately the same region of space as it was initially, so that the limit $\lim_{t\to\infty} |\Psi_j(t)|^2$ will remain finite.

Further, there is a dimensionless parameter W/I in the Anderson model, that represents disorder weighted by the overlap, or the effective disorder in a diffusion problem. Anderson's result for 3D, later confirmed by numerous investigations, consists in the following: For sufficiently large values of W/I all states are localized. There exists a critical value $(W/I)_c$ of the order of 10, at which delocalized states begin to appear in the energy range with the highest state density, cf. Fig. 2.9. At still smaller values of W/I the delocalized state region broadens, a band of extended states forms.

In our particular case of a doped semiconductor, high effective disorder W/I corresponds to low donor concentration n. With growing doping, the overlap integral (2.4), (2.6) rises exponentially and diminishes the value of W/I, that can thus be tuned through the critical value of $(W/I)_c$. The degree of disor-
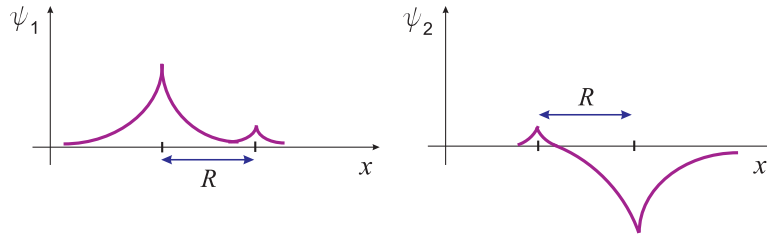
Figure 2.10: Two potential wells with significantly different ground state energies $|\epsilon_1 - \epsilon_2| \gg I(R)$ are brought together at the distance R. In either of the resulting quantum states ψ_1 and ψ_2, the electron strongly prefers one of the sites and avoids the other one.

der W/I is not the same for different energy regions, it is lowest for the highest state density regions, so that $(W/I)_c$ is first reached at the maximum of $g(E)$, as shown in Fig. 2.9 (b). However, formation of a narrow band of extended states in the middle of the impurity states region does not immediately result in metallic conductivity, if the Fermi level E_F stays in the localized region of $g(E)$. This is what we expect in our case of low degree of compensation by acceptor atoms, cf. Figs. 2.1, 2.9. If we denote by E_c the energy that separates the localized electron states from the non-localized, then σ_{dc} at zero temperature becomes finite only as the E_F passes through this boundary, as in Fig. 2.9 (c). This type of metal-insulator transition is called Anderson transition in literature [2, 11]. In our system, Si:P, it takes place at the critical donor concentration n_c. In the theory of amorphous solids, E_c is known as the mobility edge. It separates the localized states, always found in $g(E)$ at the bottom of the conduction band, from the extended states.

To obtain a better feeling for Anderson's result, an auxiliary problem of just two potential wells is already helpful, which allows a quantum-mechanical solution (cf. for instance Ref. [35]). Here again, one starts with the regular case of two identical wells separated by the distance R, with identical ground state wave functions φ_j and energies $\epsilon_1 = \epsilon_2$, each in the absence of the other. The nature of the solution described in Sec. 2.1.2 and depicted in Fig. 2.2 varies little, when weak disorder $|\epsilon_1 - \epsilon_2| \ll I(R)$ is introduced. The electron stays almost equally shared by the sites. In the opposite limit, $|\epsilon_1 - \epsilon_2| \gg I(R)$, the picture is entirely different, as shown in Fig. 2.10. As before, two linear combinations emerge from the initial site functions,

$$\psi_1 = A\varphi_1 + B\varphi_2\,, \quad \psi_2 = B\varphi_1 - A\varphi_2\,. \tag{2.23}$$

However, in either state the energy E_j is close to ϵ_j and the wave function ψ_j is close to φ_j. It holds,

$$\frac{A}{B} \simeq \frac{|\epsilon_1 - \epsilon_2|}{2I(R)}\,. \tag{2.24}$$
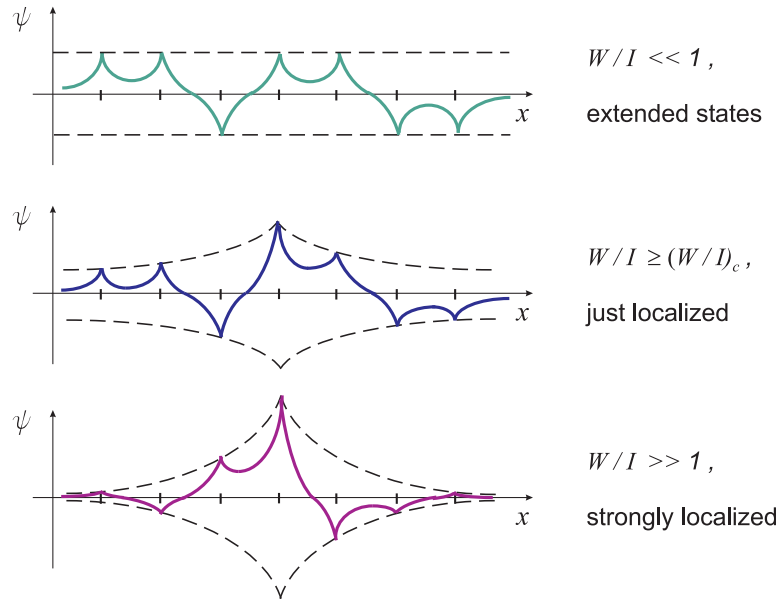
Figure 2.11: Form of the wave functions in the Anderson model.

The solutions for the wave functions of just two electrons in two potential wells can now be graphically extended to the more complicated case of several electrons coming from several sites, as depicted in Fig. 2.11.

There is a classical analogy to the change from localized to extended states in what is known as percolation problem, as pointed out first by De Gennes et al. [65] and taken on further by Ziman [66]. Suppose that we have a system which consists of cells, within each of which the potential has a constant value ε_j, and these potentials are random and independent. A particle of energy E described by classical mechanics can go from one cell to a neighboring cell if it has enough energy. Sites with energy $\varepsilon_j > E$ are not available to it. If the energy E is small, the few available cells will mostly be isolated from one another, but a small part will be members of a cluster of two or more cells. One can calculate the probability of any particular size and shape of clusters, formed by adjacent available sites. As E is increased, the probability of the larger clusters increases, and eventually there are clusters spreading through the whole system. This is a site percolation problem, complementary to the bond percolation problem, see for instance Ref. [2].

By now we have only considered the three-dimensional case, as in our system of a Si:P crystal. The Anderson criterion for the localization of the electronic states is known to be strictly applicable only to three-dimensional systems [2]. For systems with reduced dimensionality, this is different. Obviously, percolation never occurs in one dimension until all sites are available. It is also known, that

in a one-dimensional quantum system states are always localized in presence of disorder, no matter how small it is [67]-[69]. This also proves to be true in the two-dimensional case [2].

2.2.2 Quantum Phase Transitions

The $T = 0$ metal-insulator transition, driven by disorder, falls into the category of quantum phase transitions (QPTs), where changing some parameter in the Hamiltonian takes the system between two distinct ground states [64]. In Si:P, this driving parameter is the dopant density n. Interest in the theory of the zero-temperature quantum phase transitions in condensed matter systems arose as early as 1975 through the works of Young and Suzuki on quantum Ising models [70, 71] and the more general theoretical work of Hertz [72]. The recent proliferation of experimental research facilities has led to further famous examples of QPTs like the transitions between the quantized Hall plateaus, the superconductor-insulator transition in Josephson-junction arrays and magnetic transitions of cuprates or heavy-Fermion alloys.

In contrast to QPTs, phase transitions taking place at some finite critical temperature T_c, are considered "classical", even in highly quantum-mechanical systems like superfluid helium or superconductors [73]-[75]. The order parameter of those systems is of a quantum-mechanical nature, but it coherently fluctuates at ever increasing length and time scales as the classical phase transition is approached. Thus, the quantum fluctuations take place at lower and lower frequencies, as the transition point is approached. Modes, whose frequencies fall below $k_{\mathrm{B}}T_c/\hbar$, become occupied by many quanta, with the consequence that they behave classically. At the same time, this argument shows that QPTs, where $T_c = 0$, can only be described in the framework of quantum statistical mechanics. In those systems, critical fluctuations at all frequencies down to zero are quantum fluctuations.

Chapter 3

Broadband microwave spectroscopy on solids at low temperature

For our measurements of the frequency-dependent electric conductivity $\sigma_1(\omega)$ and the dielectric permittivity $\varepsilon_1(\omega)$ of Si:P, we employed the experimental arrangement schematically depicted in Fig. 3.1, where material under investigation is placed at the aperture of a coaxial probe. Using a vector network analyzer 8510, a phase sensitive measurement of the reflection coefficient is performed in a broadband frequency range from 45 MHz to 20 GHz, from which the complex impedance Z of the sample is obtained by established techniques of microwave engineering, cf. Appendix B. The signal from the source of the VNA travels along the coaxial waveguide to the sample, which electrically terminates the microwave line. The reflected signal returns the same way back and is detected by the test set of the VNA. In case of solid matter, some smart jig is needed to press the flat

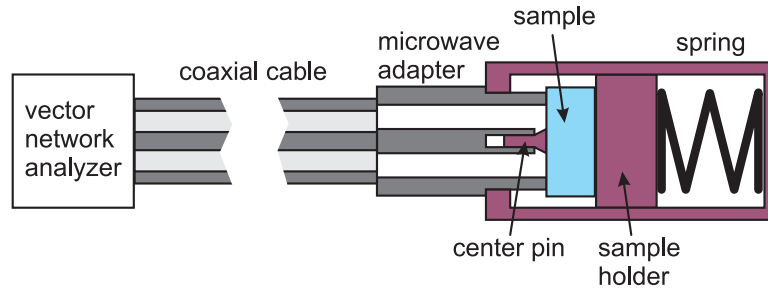Figure 3.1: Schematic picture of a broadband microwave spectrometer that employs a vector network analyzer (VNA) and a coaxial waveguide (for concrete implementation see Figs. 3.6 and 3.9). A solid sample terminates the otherwise open-ended coaxial line (after Ref. [19]). The sensor can be inserted into a temperature-controlled environment for low-temperature measurements, as shown in Fig. 3.5.

31

sample surface against the sensor [19, 20]. A strong spring at the back side of the sample holder, as in Fig. 3.1, and a resilient center conductor of a commercial microwave adapter in combination with a conical metallic pin, provide a proper mechanical connection between sample and probe. Metallic contact layer (gold or aluminum) is usually evaporated on top of the solid specimen, matching the inner and outer conductors of the coaxial probe in shape and size, as shown in Figs. 3.2 and 4.1. This is needed to achieve a proper electrical contact between the sample material and the probe; at the same time, the evaporated contacts define the sample surface area, which is exposed to the signal. The sensor can be inserted into a temperature-controlled environment (described in Secs. 3.3 and 3.4 of this Chapter) and, for a given probe size, there is a useable frequency range as broad as two orders of magnitude.

The problem of extracting the interesting material parameters from the measured reflection coefficient data can be solved in two steps: first, one needs to obtain the complex sample impedance Z from the measured reflection coefficient Γ_m, and second, the complex conductivity $\sigma(\omega)$ has to be calculated from the impedance. The second task is equivalent to extracting the complex dielectric function $\varepsilon(\omega)$ from Z, cf. Eq. (2.16).

3.1 Complex conductivity of metallic samples

The evaluation of metallic samples has been developed and experimentally tested in the recent years [19, 20].

The first task is to obtain the complex sample impedance Z from the reflection coefficient Γ_m, measured by the test set of the network analyzer, like the HP 8510. The general error model for a reflection measurement [19, 76] results in the following relation (see Appendix B.2 for more details),

$$\Gamma_m = E_D + \frac{E_R \Gamma}{1 - E_S \Gamma} \, , \tag{3.1}$$

between the measured complex reflection coefficient Γ_m and the actual reflection coefficient Γ at the sample surface. (The latter is directly related to the sample impedance Z by the well-known high-frequency engineering formula (3.2), see Appendix B.1 for details.) The three independent complex values E_R, E_S, and E_D comprise the contribution of the microwave line. To determine those values, measurements of three independent calibration samples with known actual reflection coefficients Γ as functions of frequency and temperature are required. We use bulk aluminum samples as short, Teflon samples as open and thin metallic NiCr films as load standards.

For the short standard, the perfect value $Z^{\text{short}} = 0$ is assumed in the whole frequency and temperature range, that corresponds to $\Gamma^{\text{short}} = -1$ via the Eq. (B.4), or Eq. (3.2). For a NiCr calibration sample, Γ^{load} is calculated using the Eq. (B.4) from its frequency-independent impedance $Z^{\text{NiCr}} = R_{\text{dc}}^{\text{NiCr}}$, which is measured between the outer and center conductors of the waveguide by the test set of the VNA, simultaneously with the measurement of the corresponding reflection coefficient spectrum, Γ_m^{load}. The value $R_{\text{dc}}^{\text{NiCr}}$ of a given NiCr film sample depends only on the temperature T of the measurement, but it differs from sample to sample due to the details of the NiCr film evaporation. For the two-point dc resistance R_{dc} measured by the test set, there is an offset due to the contribution of the long (almost 1 m) microwave line. It is eliminated by subtracting the measured dc resistance $R_{\text{dc}}^{\text{short}}$ of the short standard, which is by far dominated by the contribution of the coaxial line. Any open standard acts as a complex capacitor. For metallic samples under investigation, the corresponding frequency dependence of Γ^{open} turns out to be of no significant effect on the calibrated spectra. The trivial dc assumption $Z^{\text{open}} = \infty$, corresponding via Eq. (B.4) to $\Gamma^{\text{open}} = 1$, is sufficient in that case.

The sample impedance Z is directly related to the reflection coefficient Γ at the sample surface via [17] (see Appendix B.1 for more details),

$$Z = \frac{1 + \Gamma}{1 - \Gamma} Z_0 \ , \tag{3.2}$$

where Z_0 is the characteristic impedance of the microwave line with a common value of 50 Ω (which is also inherent for all of our microwave components), cf. the Eq. (B.3).

The way to extract the complex electric conductivity σ of a metallic sample from its complex impedance Z is straightforward, if the thickness of the specimen d either significantly exceeds the skin depth[1] δ or vice versa:

- $d \ll \delta$. (Fig. 3.2 a)) In the case of a thin film evaporated on an insulating substrate, the electric field strength stays nearly constant throughout the whole film thickness d. The relation between the conductivity σ and the impedance Z depends only on the geometry of the contacts. For the ring of inner radius a and outer radius b between the contacts, it reads,

$$Z = \frac{1}{\sigma} \frac{\ln(b/a)}{2\pi d} \ . \tag{3.3}$$

---

[1]The skin depth δ characterizes the exponential decay of the electromagnetic field strength in a metal, cf. e.g. Ref. [17].
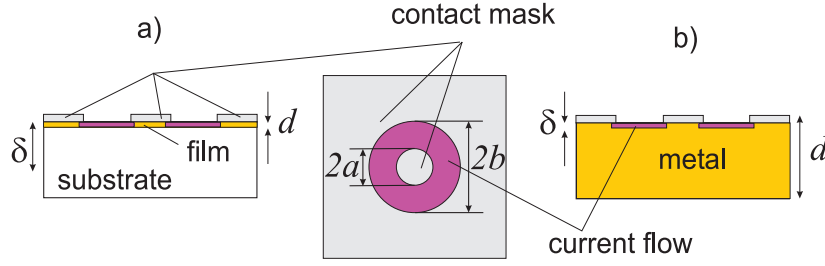
Figure 3.2: Current flow (dark magenta area) in a metallic sample (bright yellow) with a contact mask (light grey) on top of it; in our case, $2a = 0.6$ mm and $2b = 1.75$ mm. The relevant limiting cases (a) $d \ll \delta$ and (b) $d \gg \delta$ lead to a simple evaluation procedure ($\delta < 1\,\mu$m is the skin depth in a good metal, in the gigahertz frequency range).

- $d \gg \delta$. (Fig. 3.2 b)) For typical microwave frequencies of a few gigahertz, the amplitude of the electromagnetic wave in a thick metallic sample is already significantly damped (below $1/e$) at the depth of 1 μm by the skin effect. Hence, the interaction with the incident wave takes place in a thin layer at the sample surface. Boundary effects at the edges of the relatively broad contact area (cf. Fig. 3.2) are negligible, and the concept of the surface impedance Z_S based on the assumption of plane wave propagation works well [18]. The surface impedance is the field impedance evaluated at the surface of the sample; in SI units it is given by

$$Z_S = \left(\frac{\mu_0}{\varepsilon_0 \varepsilon} \right)^{1/2} , \tag{3.4}$$

  with the vacuum permeability μ_0. Throughout this text, ε is the complex dielectric function of the material under investigation, relative to the free space permittivity ε_0. Z_S can also be obtained as the two-dimensional counterpart of the volume resistivity in three dimensions and is, thus, related to the sample impedance Z by a factor that accounts for the geometry of the sample surface. In the case of a ring with inner and outer radii a and b, this relation between the surface impedance Z_S and the sample impedance Z is readily obtained by a geometrical integration, similar to the derivation of the Eq. (3.3),

$$Z = Z_S \frac{\ln(b/a)}{2\pi} . \tag{3.5}$$

  Inserting the relation between the complex conductivity and the complex dielectric function, described by Eq. (2.16), into the Eq. (3.4) yields the formula to extract the conductivity from the sample impedance Z for a
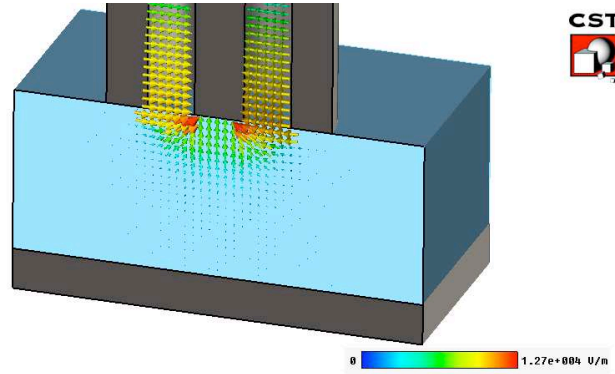
Figure 3.3: The electromagnetic field with the frequency $f = 5$ GHz is guided by a coaxial waveguide, which is terminated by an insulating Si:P sample with dimensions $5 \times 5 \times 2$ mm^3 (cf. Fig. 5.2), which is mechanically pressed against the probe (cf. Fig. 3.1). The reflected signal is measured by a VNA. The electric field distribution inside the sample is shown at its oscillation maximum, for the case of the relative dielectric permittivity $\varepsilon_1 = 40$ of the sample. While analytical expressions for the vector field are discussed in Chapter 4, this picture is obtained by a computer simulation using the commercial software CST.

thick metallic sample [77],

$$\begin{aligned} \sigma &= \frac{\omega}{i} \left(\frac{\mu_0}{Z_S^2} - \varepsilon_0 \right) \\ &= \frac{\omega}{i} \left(\frac{\mu_0 (\ln(b/a))^2}{(2\pi Z)^2} - \varepsilon_0 \right) . \end{aligned} \tag{3.6}$$

3.2 Formulation of the problem for semiconducting materials

For materials with nonmetallic conductivity, none of the simple assumptions valid for metallic samples hold and both steps of the evaluation procedure, outlined in the previous Section, contain additional challenge [15]:

1. For the calibration of the microwave line, the open standard, which comprises a complex capacitor with a known dielectric constant, is as significant as the short and the load standards, when insulating samples are measured. The dc assumption $Z^{\text{open}} = \infty$, corresponding via Eq. (B.4) to $\Gamma^{\text{open}} = 1$, is not sufficient at higher frequencies. The correct frequency dependence of the reflection coefficient Γ^{open} is indispensable, as demonstrated in Fig. 4.4 and described in Section 4.3 of the next Chapter.

2. Extraction of the material parameters (conductivity and dielectric function) from the calibrated impedance data Z is a difficult task, if material is
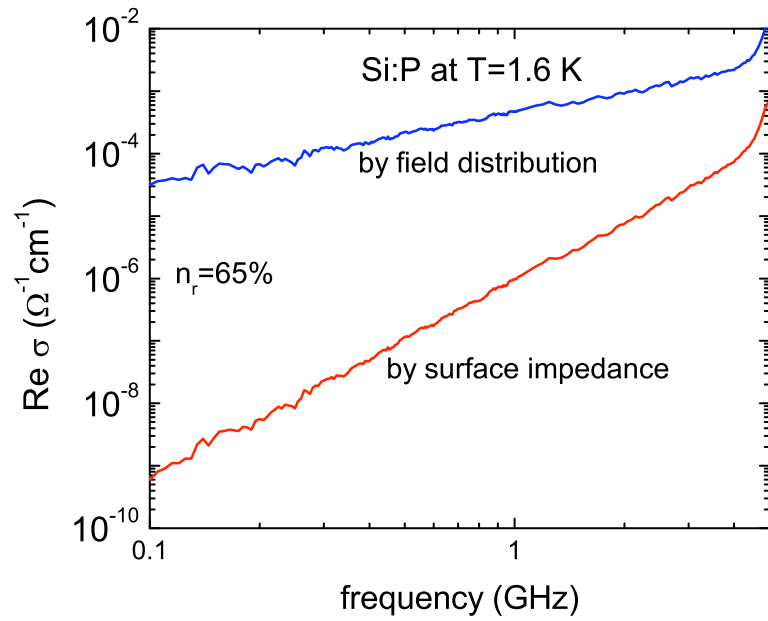
Figure 3.4: Frequency-dependent conductivity of a thick insulating Si:P sample with the donor concentration of 65 % relative to the critical value at the MIT, measured at 1.6 K. In the first case (red line), the evaluation of the impedance data was done by the surface impedance concept using Eq. (3.6), which leads to a wrong (far too strong) frequency dependence of the conductivity σ_1. By using the correct field distribution (Chapter 4), a significantly different frequency dependence (blue line) is obtained from the same raw data.

an insulator. Attempts to apply the straightforward evaluation concepts, appropriate for metals and described in Sec. 3.1, fail here:

- The surface impedance concept yields a far too strong frequency dependence of the conductivity, as demonstrated in Fig. 3.4, namely a cubic power law, while approximately linear dependence is expected from the theory, cf. Chapter 2.

- Treatment of very thin Si:B samples (0.2 mm thick) on the insulating side of the metal-insulator transition like thin metallic samples yields not a quite unexpected frequency dependence [78], but values of the conductivity lie about three orders of magnitude above those obtained in similar compounds with resonator techniques [43, 44] and at higher frequencies by established optical techniques [32]-[34]. This experiment by Lee and Stutzmann [78] is to our knowledge the only reported predecessor measurement of the complex conductivity of an insulating semiconductor with a broadband technique in the microwave range and it was performed at very low temperatures of 0.08 K only achievable in a dilution refrigerator.

The electromagnetic wave penetrates deep into a nonmetallic sample, because – in contrast to a metal – the real part of the dielectric permittivity ε is positive for an insulator. With the change from the negative to the positive sign of the dielectric constant ε in the wave equation for the electric field E oscillating with the frequency ω (Helmholtz equation),

$$\nabla^2 E + \frac{\omega^2}{c^2}\varepsilon E = 0\,, \tag{3.7}$$

(where $c = 1/\sqrt{\mu_0 \epsilon_0}$ is the speed of light in the vacuum), the spacial solution for the electric field changes from the exponentially decaying to the oscillating function, i.e. the electric field solution propagates in space inside the insulating material. Field decay in such a sample is only caused by the finite dimensions of the electric contacts, cf. Fig. 3.3, and only to some minor degree by the weak absorption through the relatively small imaginary part of the dielectric function ε. In case of a 2.4 mm coaxial probe, the electric field strength falls below 1 % of its original value at the sample surface only after penetrating more than 2.5 mm, for frequencies up to 5 GHz and for relative dielectric constant ε_1 up to 50 (this comprises all our reported Si:P samples, cf. Fig. 5.7). In other words, the penetration depth of the electric field is of the order of the contact area dimensions (compare Fig. 3.3) and rapidly increases with rising frequency f and permittivity ε_1 (the latter is due to the reduction of the wavelength via $\lambda \sim 1/\sqrt{\varepsilon_1}$). Thus, in contrast to the metals, the spatial field distribution which forms inside an insulating semiconductor is significantly different from that of a plane
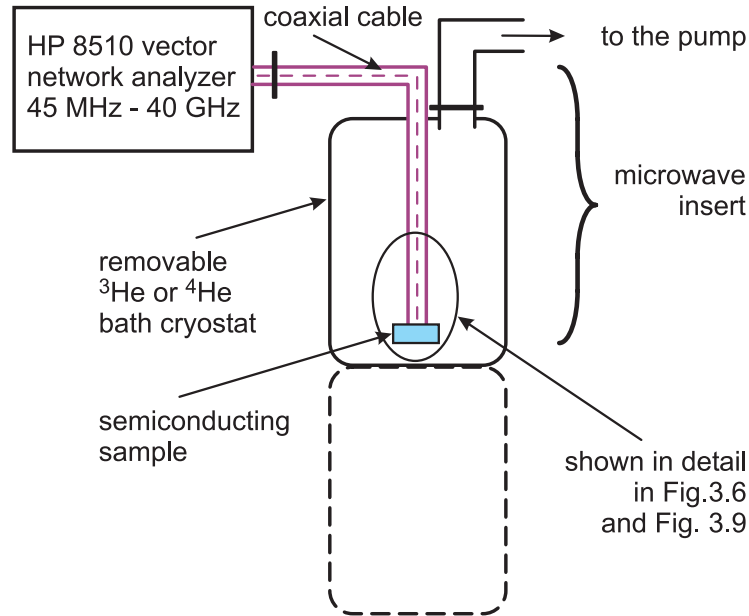
Figure 3.5: Schematic representation of a low-temperature experiment, that employs a vector network analyzer (VNA) and a coaxial waveguide for a reflection coefficient measurement (after [19, 20]). To exchange the sample, the cryostat can be removed from the microwave insert without disconnecting the microwave connections. This is necessary for a proper low-temperature calibration of the spectrometer.

wave, cf. Fig. 3.3, and it strongly depends on frequency, cf. Figs. 4.6 - 4.8. Its knowledge is essential to extract the complex conductivity σ (or the complex permittivity ε) of such a sample from its complex impedance Z. Integral equations, implying the accurate solution for the electromagnetic field in the insulating sample, cannot be directly solved for ε. Hence, approximations are required or simplified models need to be developed, with a limited range of validity for the frequency and the dielectric constant.

In the next Chapter, we present our solution to the problem of extracting the material parameters of a semiconducting sample from the complex impedance data, which is already published in our paper [15].

3.3   Spectrometer based on a ^{4}He-bath cryostat

The measurements of the complex microwave conductivity $\sigma(\omega, n, T)$ of Si:P for the present thesis, which are reported in Chapter 5 further below, were performed at temperatures down to 1.1 K in a pumped ^{4}He-bath cryostat. The original spectrometer, we had at our disposal at the beginning of the work presented here, had been built and optimized for broadband microwave measurements at superconducting and metallic specimens at temperature down to 1.7 K by M. Scheffler
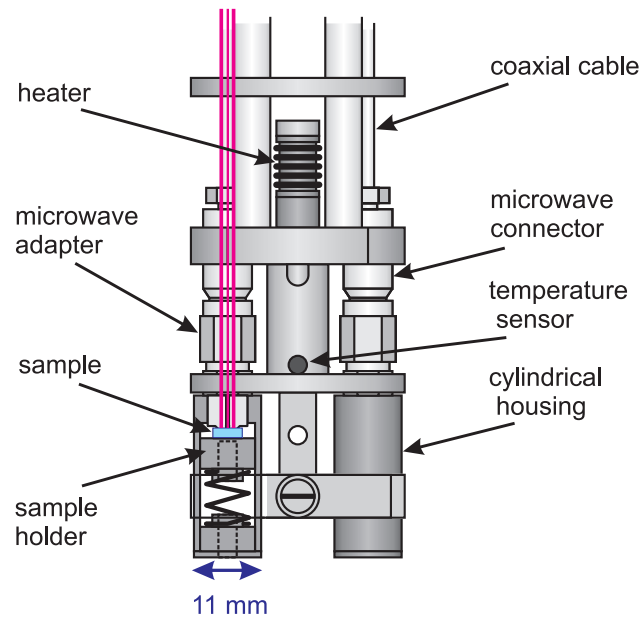
Figure 3.6: Sketch of the microwave measurement insert for the setup, based on a ^{4}He-bath cryostat, after [19, 20].

[20], after the one developed by Booth et al. [19] in the group of S. Anlage in Maryland, USA. In the course of the work constituting the current thesis, that spectrometer has been further developed and accomplished, in order to extend the scope of the measurable materials to the insulating and semiconducting solids and to reduce the base temperature from 1.7 K to 1.1 K, while the possible limit achievable with a pumped ^{4}He-bath cryostat is about 1 K [79].

A schematic representation of a low-temperature setup for broadband microwave spectroscopy is shown in Fig. 3.5. The microwave insert for measurements in a standard four-wall glass ^{4}He-bath cryostat[2] (which can be seen as a part of a ^{3}He-bath cryostat in Fig. 3.8) is shown in Fig. 3.6. It allows a simultaneous reflection coefficient measurement of two samples in two electrically independent microwave channels, provided by the two-port vector network analyzer HP 8510. To avoid thermal instabilities, due to the pumping process, and for an independent control of the thermal link between the microwave insert and the ^{4}He liquid and vapour in the bath, the measurement insert is protected by a thin-walled stainless steel cylinder, filled with a contact ^{4}He gas, whose pressure is controlled separately from the bath pressure. To perform a low-temperature calibration of the spectrometer, three independent measurement cycles with three calibration standards need to be performed, cf. Appendix B.2. To maintain

---

[2]Compact and comprehensive information on the low-temperature measurement techniques can be found, for instance, in the book by F. Pobell [79].

the microwave properties of the whole transmission line, such as standing waves stemming from all the partially reflecting interfaces, no microwave connections are disconnected to exchange the sample between two low-temperature measurements. Instead, the cryostat is carefully removed from the probe with a pneumatic arrangement, as soon as the set up is heated up to room temperature [20].

The temperature is controlled by the Lakeshore 340 Temperature Controller, using a temperature sensor [80] and a heater, thermally connected to the sample. The uncertainty of the temperature measurement depends on the considered temperature range. In the low-temperature interval below 5 K, which is particularly relevant for the current thesis, the uncertainty is below the limit set equal to 50 mK by the computer program, which controls the measurement procedure. Due to the constructional spacial separation between the temperature sensor and the sample, cf. Fig. 3.6, a small spatial temperature gradient (which cannot be avoided in a continuous automatized procedure of recording the microwave spectra, where the setup is gradually heated up with the heater) leads to slightly different values of temperature at the sample and at the sensor position. The temperature calibration is simply done by using any dilutely doped Si:P sample with a strong temperature-resistance dependence to assign the corresponding values obtained during the slow cool down (where no significant temperature difference is expected due to a good thermal connection between sample and sensor) and during the subsequent automatized heating up.

The following modifications have been performed to accomplish the original spectrometer in the course of the work, constituting the current thesis. The first two modifications were done to reduce the base temperature from 1.7 K to 1.1 K. The third technical improvement was needed to expand the range of measurable materials from metals and superconductors to semiconductors and insulators, like Si:P at low doping.

1. The stable and reproducible base temperature of 1.7 K of the original spectrometer has been reduced to a stable and reproducible base temperature of 1.1 K by exchanging the standard copper coaxial cable [81] against the specially manufactured coaxial cable, whose outer conductor is stainless steel and the inner conductor is silver plated BeCu alloy [82]. This combination has been selected, as the best trade-off between the desired minimum thermal conductivity λ_{thermal}, needed to minimize the thermal link of the probe to the room temperature environment, and the good metallic conductivity σ_{metal} (low resistivity ρ_{dc}), needed to minimize the high electric losses in the almost 1 m long microwave cable. Since both quantities are proportional in a metal, $\lambda_{\text{thermal}} \sim \sigma_{\text{metal}}$, the standard copper coaxial cable has nice electric characteristics, as can be seen in Tab. 3.1, but transports more heat from the environment into the cryostat than the cooling power

of pumped liquid [4]He can compensate to achieve temperatures below 1.7 K.

Table 3.1: Comparison of thermal and electrical characteristics of the metals, available as the material of commercial coaxial cables suited for high-frequency application up to 50 GHz. Sources of information are the NIST (National Institute of Standards and Technology) and book by O. V. Lounasmaa [83]. The transmission power ratio P/P_0 for signal propagation along the 1 m long cable and back, based on the typical attenuation values from the Micro-Coax Catalog [84], are listed for the standard commercial coaxial cables with the same material used for the inner and the outer conductor, respectively.

property	stainless steel (SS 304)	BeCu (Alloy 25)	Cu (pure commercial)
electrical resistivity $\rho_{dc}(300 \text{ K})$ ($\mu \Omega$ cm)	72	7.81	1.71
thermal conductivity $\lambda_{\text{thermal}}(\frac{W}{Km})$ at low T	$0.15 \cdot T$	$0.45 \cdot T$	$150 \cdot T$
relative power P/P_0, for bidirectional transmission, 20 GHz, 1 m length	0.04 (UT 85-SS)	0.16 (UT 85-B-B)	0.22 (UT 85C-TP-LL)

A critical comparison of the standard coaxial cables [81, 85, 86], with the same kind of material used for the center and the outer conductor, respectively, is shown in Tab. 3.1. Each of those cables exhibits too bad characteristics for our goal, either for the electrical or for the thermal aspect. Thus, we have selected and specially ordered a modified model [82]. Reasoning, that the center conductor area (proportional to $(0.51 \text{ mm})^2$) only amounts to 0.13 of the outer conductor area (proportional to $(2.2 \text{ mm})^2$– $(1.68 \text{ mm})^2$), the contribution of the former to the thermal transport is 10 times less in comparison to the latter. At the same time, the center conductor is by far the major contributor to the electrical attenuation, as can readily be calculated as well. Thus, the most judicious combination to minimize thermal link by preserving tolerable electric conduction, is the least thermally conducting material (stainless steel) for the outer conductor with the medium thermally and electrically conducting material (BeCu) for the center conductor.

Once the outer conductor of the coaxial cable was chosen to be made of stainless steel instead of copper, it turned out to be quite a challenge to solder microwave connectors to it. The biggest problem is that stainless steel is not wetted by tin; the second (and minor) problem is that steel is very hard to cut, especially if one does it by hand for precision reasons, required by a microwave spectrometer construction. The standard method to assembly and solder a microwave connector to a coaxial cable is provided in detail, with all the necessary mechanical equipment, by the manufacturer of the microwave components [87]; but it only applies to the standard tin-plated copper coax [81]. In the case of stainless steel, we needed to meet all the precision requirements even more strictly, since due to the much higher electrical losses in comparison to the copper coax, the calibration of the microwave line is much more sensitive to any deviation from the perfect electric connection between the microwave components. To this end, we have [88] developed an individual tailoring and soldering technique for the stainless steel coaxial cable, which involves plating of the cable surface with the special solder and flux [89]. The result can be seen at the very low base temperature of 1.1 K, as well as at the quality of the Si:P spectra presented in this work, all of which were obtained after completing the technical modification of the setup, described here.

2. A new glass ^{4}He-cryostat has been build, with better characteristics as the old one at the original setup. The principal structure of the new cryostat staying the same as shown in Fig. 3.8, the depth of the ^{4}He-bath is increased by 14 cm, and the insulation is improved compared to the old one. Without increasing the length of the microwave insert, we make use of the additional depth and the lower base temperature at the bottom of the new cryostat by employing a cooling finger, made of copper and thermally connected to the insert.

3. An additional mechanical fixing arrangement, made of aluminum, has been constructed and built [90] to fix the microwave insert for the time the sample is exchanged. After the cryostat and the contact gas cylinder are removed, the microwave insert is hanging over 70 cm down free in space and can easily be deflected by several angular degrees, if inadvertently pushed from the side. The metallic samples, measured with the original spectrometer by our predecessors, allowed an in situ calibration by using the superconducting phase as a short standard, while the other two calibration standards had a vanishingly small influence on the resulting spectra. In contrast to that, all three calibration measurements exhibit a significant contribution to the result of a measurement of an insulating material like Si:P. Thus, in the current project, the requirement for the stability of the microwave line between the independent low-temperature measurements became crucial.
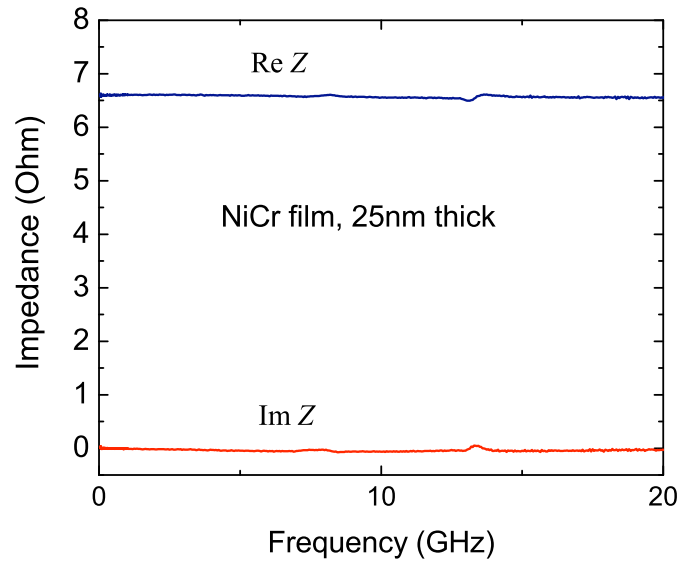
Figure 3.7: Test measurement of a thin metallic NiCr film, 25 nm thick, at 1.1 K.

Analyzing and testing the residual (i.e not completely eliminated by the calibration) standing waves[3] present in the final spectra, we found the origin of the problem to be of mechanical nature and fixed it.

To ascertain the proper function of the spectrometer, various tests have been performed close to the reported measurements. The most important ones are the following:

- The most sensitive test to detect any electrical problems in the microwave line (like lost calibration quality or disconnected contacts) is the measurement of thin (25 nm thick) metallic NiCr films, whose real-valued impedance of 6 to 8 Ω is frequency-independent in the microwave range. An example of a NiCr film spectrum at 1.1 K is shown in Fig. 3.7. Since we also use the NiCr films as a load calibration standard, as described in Sec. 3.1, this test is performed on a regular basis within several days from each sample measurement.

- In order to exclude any self-heating effect in the semiconducting insulating Si:P samples, we tested the power dependence of the spectra at 1.1 K and at 4.2 K. Measuring with the source power of -10 dBm, which corresponds to 0.1 mW, we irradiate the sample with the microwave power equal to 20 μW, following from the known electrical losses in the 1 m long coaxial cable. Self-heating effects, if present, would depend on the microwave power. Varying the source power by the factor of 2 below and above the value 0.1 mW

---

[3]Any pair of microwave connections in the coaxial waveguide acts as a bad Fabry-Perot resonator due to inevitable partial reflection of the electromagnetic wave at each interface.
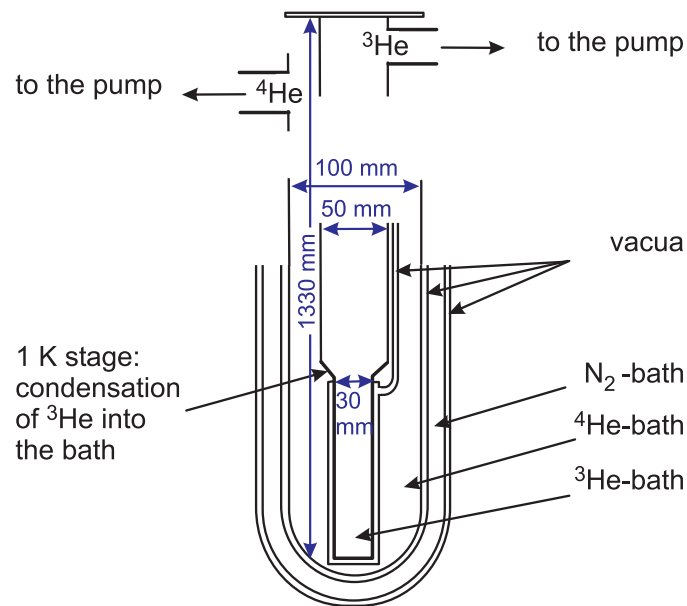
Figure 3.8: Principal structure of the old ^{3}He-bath cryostat [91], reactivated in this work to set up a new broadband microwave spectrometer, as described in Sec. 3.4. A stainless steel ^{3}He-vessel is immersed into a four-wall glass ^{4}He-cryostat. The condensation of the ^{3}He-gas into the ^{3}He-bath is achieved by pumping on the ^{4}He-bath, until the base temperature of approximately 1 K is reached at the 1 K stage. The new microwave insert, constructed for this ^{3}He-cryostat, is depicted in Fig. 3.9.

(corresponding to -13 dBm and -7 dBm), we have detected no change in the measured reflection coefficient spectra for all the Si:P samples reported.

3.4 Spectrometer based on a ^{3}He-bath cryostat

Parallel to the work at the ^{4}He-setup, described in the previous Section, a development of a new microwave spectrometer has been started in the course of the work presented here, on the basis of an old ^{3}He-bath cryostat, which was built in the works of M. Welte [91] and F. Maier [92] and is schematically depicted in Fig. 3.8. Our ultimate goal with this apparatus is to set up a broadband microwave spectrometer, running in a similar way to the one based on the pumped ^{4}He-cryostat, but with a significantly lower base temperature. It turned out to be 450 mK with the equipment, I set up in the reported work, which is quite satisfactory, considering the theoretical limit of 0.3 K for this kind of cryostat [83] and the reported base temperature of 0.55 K by our predecessors at that particular cryostat [92]. The motivation came for several reasons. The fruitful results, that could be achieved with the ^{4}He-spectrometer in a broad scope of materials from superconductors to insulating semiconductors, encouraged us to expand the project to a second setup with the following additional features. First, studying the low-energy phenomena like the electronic correlation effects or the critical behavior close to the zero-temperature metal-insulator transition, it is desirable to measure at temperatures as low as possible. The theoretical quantum limit $k_\mathrm{B}T \ll \hbar\omega$ can be strictly reached in the GHz range only at temperatures below 1 K, since 1 K corresponds to 20 GHz. Second, there is a constructional possibility to apply a magnetic field at the ^{3}He-setup, which allows to further expand the parameter space of our broadband microwave spectroscopic technique (cf. Chapter 6).

In contrast to the compact and mobile ^{4}He-cryostat at the setup, described in the previous Section, the ^{3}He-cryostat as a whole cannot be moved away from the measurement insert. In addition to the pumped glass ^{4}He-bath, it contains a pumped ^{3}He-vessel (Fig. 3.8), which is made of stainless steel and is a part of a spacious ^{3}He-cycle with a separate pump system and two ^{3}He-tanks. Still, a possibility to exchange the sample between the low-temperature measurements without disconnecting the microwave connections, as in Fig. 3.5, is crucial for the extremely sensitive calibration procedure of a broadband spectrometer, as argued in the previous Section. Additional electric losses in a much longer (1.5 m instead of 1 m at the ^{4}He-setup) microwave line, corresponding to the size ^{3}He-cryostat, make this requirement even more urgent. Thus, we constructed and built [88] a mechanical equipment, which can move the microwave measurement insert together with the vector network analyzer out of the stationary ^{3}He-cryostat and back into it, without disconnecting the microwave line, i.e. the new setup is also
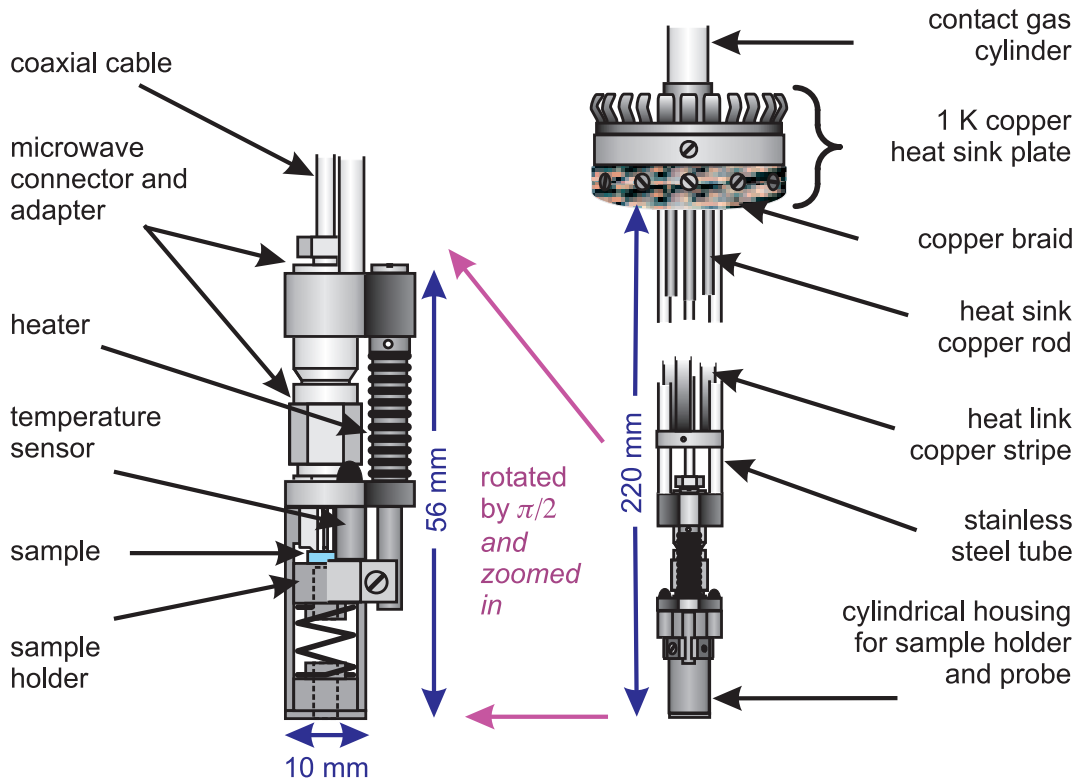
Figure 3.9: Sketch of the microwave measurement insert, designed and built in the course of the current thesis as a basis of a new broadband microwave spectrometer, employing the ^{3}He-bath cryostat shown in Fig. 3.8. To the left, the probe head is shown again, enlarged by a factor of 2 and rotated around the insert's axis by $\pi/2$.

consistent with the Fig. 3.5.

The microwave insert for the new ^{3}He-setup was developed in the present work with a huge support of the mechanical and low-temperature workshops foremen G. Dietrich and J. Maurer [93, 94]. The principal structure and elements are depicted in Fig. 3.9. To the left, the probe head is shown once again, enlarged and rotated around the insert's axis by $\pi/2$. In spite of an extreme scarceness of the space, imposed by the dimensions of the existing ^{3}He-vessel shown in Fig. 3.8, we decided to use a thin-walled stainless steel cylinder filled with a ^{3}He contact gas, to protect the probe of thermal instabilities due to the varying level of the liquid ^{3}He and to have a pressure control independent from the ^{3}He-bath. The contact gas cylinder is shown in Fig. 3.9 only above the 1 K copper link plate. The 1 K copper link plate is build of massive copper and is pressed against the funnel-shaped 1 K stage of the ^{3}He-vessel, shown in Fig. 3.8. This is the last and the coldest thermal link of the ^{3}He-vessel to the ^{4}He-bath, below that funnel a vacuum section thermally disconnects the ^{3}He-bath from the ^{4}He-bath. The latter is constantly held at its base temperature of approximately 1 K by pumping

on the ^{4}He-liquid, while the former is further cooled down by pumping on the condensed ^{3}He. Inside the ^{4}He-bath, the 1 K stage is thermally connected to the bottom of the ^{4}He-cryostat by a copper coat (not shown in Fig. 3.8) to ensure it is constantly at 1 K.

The thermal link of all the cables and wires of the measurement insert to the 1 K stage is essential for cooling the insert with ^{3}He. Due to the linear dependence of metals thermal conductivity λ_{thermal} on temperature, cf. Tab. 3.1, the temperature inside a coaxial cable or a wire drops in a cryostat not linearly with distance, but rather as a square root function of the distance x from the cold end. As a result, without extra thermal sinking on the cables way down to the bottom of the cryostat, its temperature at the level of the 1 K plate would be as high as 117 K (calculation performed for our concrete case of the stainless steel coaxial cable [82] and the dimensions of our ^{3}He-cryostat). The cooling power of the ^{3}He-evaporation would be far too weak to cool down an insert with such a huge thermal transport from the outside. Thus, careful thermal sinking of all the cables and wires by connection to the ^{4}He-bath is indispensable. As depicted in Fig. 3.9, it is done in the new microwave insert by well-known techniques [95], using bulk copper, coper rods, copper braid and copper stripes, as well as elastic stripes [96].

Not shown in Fig. 3.9 is the part of the contact gas cylinder, which is put on the insert from below and screwed to the 1 K copper plate, using a low-temperature elastic metallic sealing [97]. To facilitate the cooling of the sample by the liquid ^{3}He, the lower part of the contact gas cylinder (30 mm high), which is immersed into the ^{3}He-liquid when all of the ^{3}He-gas is condensed, is made of copper. The microwave components employed at low temperature are listed in Refs. [82, 87], additional parts used at the room-temperature end of the coaxial cable are listed in Refs. [81, 98].

For precise, accurate, low noise and low excitation temperature measurement and control at temperatures down to 0.3 K, a new 370 AC Resistance Bridge [99] was provided by the DFG (Deutsche Forschungsgemeinschaft). This device allows up to 16 temperature sensors being scanned, while we necessarily need at least three at that stage of our experiment. Two Cernox sensors, suited for ^{3}He-temperatures down to 0.3 K [100], are symmetrically placed in good thermal connection (by bulk copper) to the sample, as depicted in Fig. 3.9. One of those sensors is commercially calibrated by LakeShore for temperatures down to 0.3 K and is employed to calibrate the second sensor. The thermally identical positioning of two identical temperature sensors provides a perfect control of possible instabilities or damages in the temperature measurement equipment. One further sensor [80] is employed to control the temperature of the ^{4}He-bath at the stage of the 1 K copper heat sink plate.

Having developed and built up the described mechanical movement mechanism and the microwave measurement insert, with the support of the mechanical and the low-temperature workshops [88, 93, 94], I brought the ^{3}He-setup up to the final thermal tests with the new insert. At that stage, my successor K. Steinberg assisted me with the final preparations like connecting the cables and wires, as well as with the cooling tests, in order to take over the setup and ultimately bring it to the broadband microwave measurements later on her own. The first thermal tests with the new insert, provided with all the components necessary for the future microwave spectroscopic measurement including a sample, resulted in a stable and reproducible base temperature of 450 mK, which could be held constant for over 10 minutes.

Chapter 4

Self-consistent evaluation procedure, developed for broadband complex conductivity measurements of semiconducting materials

In this Chapter, we present our solution to the problem of extracting the material parameters - the electric conductivity σ_1 and the dielectric permittivity ε_1, both combined in a complex quantity σ (alternatively, ε) via the Eq. (2.16), - from the broadband microwave measurement of the complex impedance Z of an insulating semiconductor. This analysis method has already been published in our article in the Journal of Applied Physics [15]. The corresponding measurement technique, the comparatively simple data evaluation for metallic samples and severe problems, which arise for semiconducting materials under test, were described in the previous Chapter 3. Our experimental results for the doped semiconductor Si:P will be discussed in the next Chapter 5; they are also already published in our article in the Physica Status Solidi C [16].

We first suggest in Sec. 4.1 a simple static model for the electric current distribution inside a semiconducting sample, which proves to yield a good approximation to the rigorous solution in the low-frequency range up to 1 GHz. In Sec. 4.2, we make use of the results by Levine and Papas [53] and Misra [25] to relate the complex impedance Z of a semiconducting sample to its complex permittivity ε. In the subsequent Sec. 4.3, the rigorous electromagnetic field distribution from Sec. 4.2 is used to determine the frequency dependence of the reflection coefficient Γ^{open} for the open standard, which is essential in the calibration procedure of an insulating sample, as was pointed out in the Sec. 3.2 of the previous Chapter.

4.1   Our static model for the relation between the complex impedance and the complex conductivity

As a first approach to extract the complex conductivity σ of a low-loss semiconducting sample from its impedance Z, we developed a simple static model for the current distribution in a sample, based on the following assumptions [15]:

1. The response is local,

$$\vec{j}(\vec{r}) = \sigma \cdot \vec{E}(\vec{r}), \tag{4.1}$$

   where $\vec{j}$ is the electric current density and $\vec{E}$ is the electric field vector. This assumption implies that the electric field does not significantly vary at the distances of the mean free path ℓ, which in the case of hopping transport is the mean separation of the hopping partners.

2. The dependence of the electric field $\vec{E}(z, \rho)$ on the cylindrical coordinates z and ρ, as in Fig. 4.1, can be separately accounted for. There is no dependence on the angular coordinate φ due to the radial symmetry of the problem.

3. Inside the coaxial line the principal TEM mode is excited; thus, only the radial component of the electric field $E(\rho)$ exists. The Gauss theorem yields $E(\rho) = \text{const}/\rho$. With the voltage U between the mask contacts of radii a and b (Fig. 4.1), it follows

$$E(\rho) = \frac{U}{\ln(b/a)} \cdot \frac{1}{\rho}. \tag{4.2}$$

4. As far as the z dependence of the electric field strength is concerned, we assume that the field is concentrated at the surface and gets weaker for further depth because the path length for the corresponding current element dI increases. To calculate the total current flowing through a sample, we have chosen the cross section of the sample at the mid-distance between the Al contacts (Fig. 4.2). The single current line is approximated by a triangle shape with the apex at the mid-distance cross section. Hence, we consider each infinitesimal current line at its lowest point designated by the z coordinate and assume for the corresponding electric field $E(\rho, z)$ to be reciprocally proportional to the length of the current line in order to keep the voltage U constant,

$$E(\rho, z) = E(\rho) \cdot \frac{l(0)}{l(z)}, \tag{4.3}$$

   where $l(z) = l(0)\sqrt{1 + [2z/l(0)]^2}$.

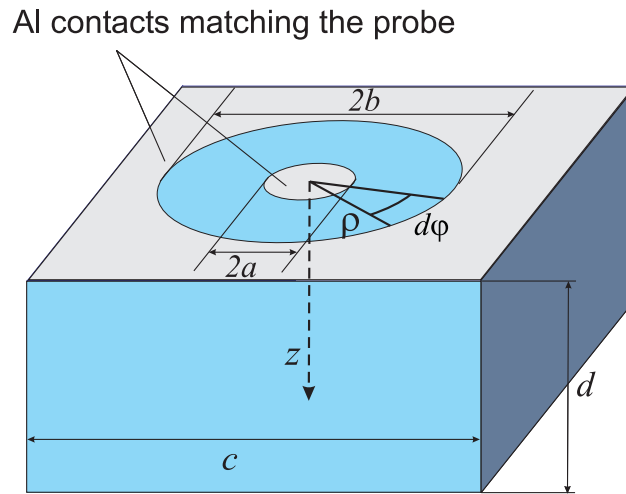Figure 4.1: Sketch of an insulating semiconducting sample with the aluminum contact layer (light grey) on top. $2a = 0.6$ mm, $2b = 1.75$ mm, corresponding to a 2.4 mm microwave coaxial adapter, $c = 5$ mm, $d = 2$ mm.
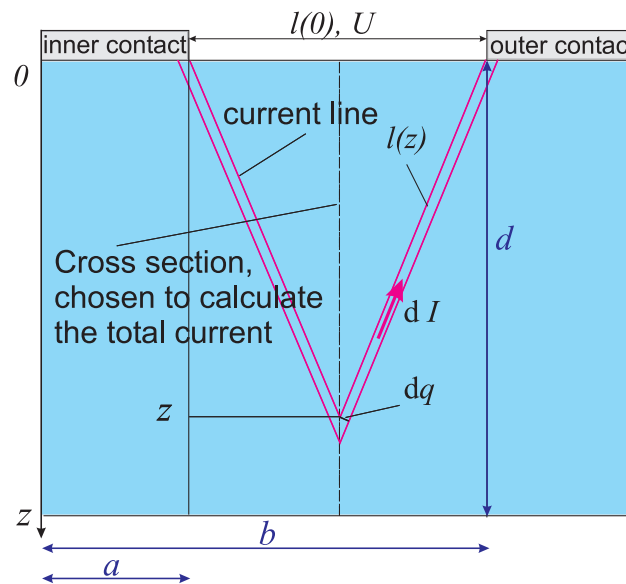

Figure 4.2: Geometry of the current distribution in a semiconducting sample of thickness d, with metallic contacts at distance $l(0) = (b - a)$ (cf. Fig. 4.1), as assumed in the static model.

Now that $E(\rho, z)$ is constructed, we can calculate the total current I flowing through a semiconducting sample using Eqs. (4.1)-(4.3). The integral is taken over the entire mid-distance cross section (see Fig. 4.2) with the infinitesimal element $dq = dz/\sqrt{1 + [2z/l(0)]^2}$,

$$
\begin{aligned}
dI(\rho, z) = j(\vec{r}) \cdot \rho \, d\varphi \, dq &= \sigma \cdot E(\rho, z) \cdot \rho \, d\varphi \, dq \\
&= \frac{\sigma \cdot U}{\ln(b/a)} \cdot \frac{d\varphi \, dz}{1 + [2z/l(0)]^2} \ , \\
I = \int_0^{2\pi} \int_0^d dI(\rho, z) &= \frac{\sigma \cdot l(0) \, \pi U}{\ln(b/a)} \arctan\left[\frac{2d}{l(0)}\right],
\end{aligned}
$$

where $l(0) = b - a$ (Fig. 4.2). Thus, we have obtained a relation between the complex impedance $Z = U/I$ at the sample surface and the complex conductivity σ,

$$
\sigma = \frac{1}{Z} \cdot \frac{\ln(b/a)}{\pi(b - a) \arctan[2d/(b - a)]} \ . \tag{4.4}
$$

In the limiting case of a thin conducting film, there is a simple geometrical relation between the conductivity and the impedance because the z dependence of the electric field and the boundary effects can be neglected. This allows us to check the above formula in the limit of $d/l(0) \to 0$, where we recover the Eq. (3.3).

The static model has been applied to analyze frequency-dependent impedance measurements of Si:P at low temperatures. As demonstrated by the dash-dotted lines in Figs. 4.3 and 4.4, the results of Eq. (4.4) agree very well with the rigorous solution outlined in the following sections. Deviations can be noticed only above 1 GHz in the dielectric constant.

4.2   Rigorous treatment of the relation between the complex impedance and the complex permittivity of a semiconducting sample

4.2.1   General considerations

A large variety of methods has been developed in the past to extract the properties of low-loss and lossy dielectrics from a reflection coefficient measurement in the radio-frequency and microwave range. Simple ingenious models and analytical solutions, which are valid in a limited parameter range, have been suggested; time-consuming but arbitrarily precise numerical approaches have been treated depending on the specific practical goals. A comprehensive list of references is available in review articles such as Ref. [31].

In studies of soft and liquid materials, the coaxial probe was frequently modeled as an equivalent circuit consisting of several fringe-field capacitors in the
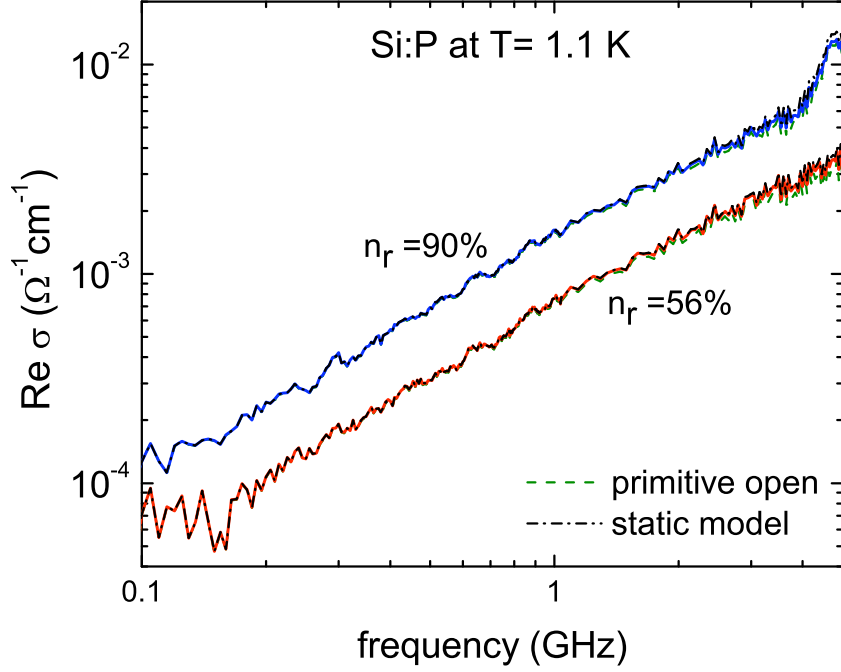
Figure 4.3: Frequency-dependent conductivity of Si:P samples with relative donor concentrations $n/n_c = 0.56$ and 0.9 (which correspond to the limiting doping values reported in this thesis, cf. Tab. 5.1) at $T = 1.1$ K, measured with the spectrometer described in Sec. 3.3. The solid colored line (red for $n/n_c = 0.56$ and blue for $n/n_c = 0.9$) represents in either case the conductivity obtained by our complete evaluation procedure, presented in Secs. 4.2 and 4.3. For comparison, the dash-dotted lines are plotted for either doping value, which stem from evaluating the complex impedance data using the formula (4.4) of the static model. To test the influence of the open calibration standard, the dashed lines are plotted for either doping value, obtained from the calibration based on the primitive assumption $\Gamma^{\mathrm{open}} = 1$ for the open calibration standard. One can see that, concerning the conductivity, all the three lines for either concentration n/n_c (n_c is the concentration value at the zero-temperature metal-insulator transition $n_c = 3.5 \times 10^{18}$ cm^{-3}) are virtually identical, with only slight effects above 1 GHz.
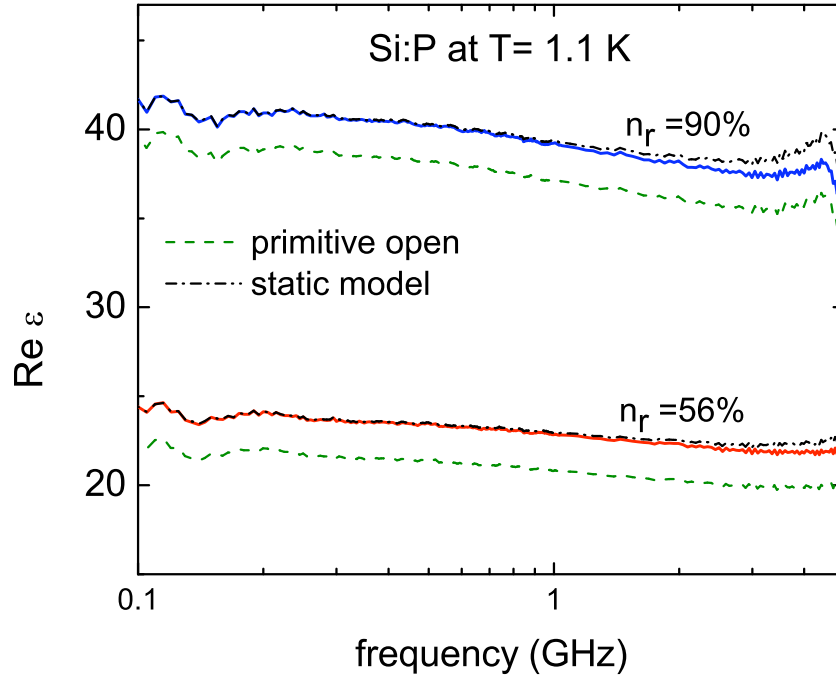
Figure 4.4: Typical permittivity spectra of Si:P samples with limiting doping values of 0.56 and 0.9 relative to the donor concentration at the metal-insulator transition $n_c = 3.5 \times 10^{18}$ cm^{-3} (cf. Tab. 5.1), measured at $T = 1.1$ K with the spectrometer described in Sec. 3.3. The solid lines (red for $n/n_c = 0.56$ and blue for $n/n_c = 0.9$) correspond to our complete evaluation procedure described in Secs. 4.2 and 4.3. For comparison, the dash-dotted lines are plotted for either doping value, which stem from evaluating the complex impedance data using the formula (4.4) of the static model. To test the influence of the open calibration standard, the dashed lines are plotted for either doping value, obtained from the calibration based on the primitive assumption $\Gamma^{\text{open}} = 1$ for the open calibration standard. Above 1 GHz, the spectra obtained by the simple static model start to deviate from the rigorously evaluated data, this deviation becoming stronger with growing frequency. Assuming the primitive (frequency-independent) dc value for the open calibration standard homogeneously shifts the ε_1 spectra to significantly lower values, with respect to the rigorous evaluation of the data.

lumped-element approach [21, 26, 28, 29]. In Ref. [26], a comprehensive, detailed and critical revision of this method can be found. The most striking point is the strong dependence of the model capacitances on the permittivity of the material that terminates the coaxial line; thus, the approach is limited to specimens with dielectric properties close to those of the reference materials available.

Here, we consider a convenient analytical way to extract the complex conductivity σ (or, equivalently by Eq. (2.16), the complex permittivity ε) from the sample impedance Z based on the works of Levine and Papas [53] and Misra [25]. The method is valid at least up to 5 GHz for the 2.4 mm probe and relative dielectric constant values up to 50; an extension to higher frequencies is possible with certain numerical procedures added. As an intermediate result, there is an integral expression for the sample admittance $Y = 1/Z$ as a function of the material dielectric function ε, which is well suited to determine the frequency dependence of the open calibration standard in a closed manner (cf. Secs. 3.2 and 4.3). The theoretical expressions for the electromagnetic field on both sides of the sensor aperture, found in the Ref. [53] for the case of the free space, are rewritten for the case of a medium with an arbitrary complex permittivity ε in the sample half-space. For the parameter range considered here [101], we regard the variational principle applied by Levine and Papas as preferable to the precise but time-consuming numerical method of point-matching proposed by Mosig *et al.* [22] and Grant *et al.* [26].

4.2.2 Solution in the form of an integral equation

In the following, the coaxial waveguide with a center conductor of radius a and an outer conductor of radius b is terminated by an infinite-plane conducting flange at $z = 0$ (Fig. 4.5). By choosing the dimensions a and b of the coaxial line to be small enough, the assumption of a single propagating mode (the principal TEM mode) in the coaxial region is justified in the covered frequency range. This system is amenable to a detailed theoretical analysis [53] that yields the electromagnetic field distribution in the half-space $z > 0$ and a relation between the aperture admittance Y (current-to-voltage ratio at $z = 0$) and the complex wave vector $\vec{k}$ of the free space $z > 0$.

We may assume an insulating sample to fill the half-space $z > 0$ by choosing its finite dimensions to be large enough for the electromagnetic field strength, so that the sample boundaries are negligible (cf. Sec. 3.2 and Ref. [102]). The results for the free space found in Ref. [53], then, transform into a relation between the admittance $Y = 1/Z$, measured at the sample surface $z = 0$ in our experiment, and the complex dielectric function ε of the sample. This relation (which is crucial for our evaluation method and with whose derivation we a concerned in the current Section) has the form of an integral equation with respect to the complex wave
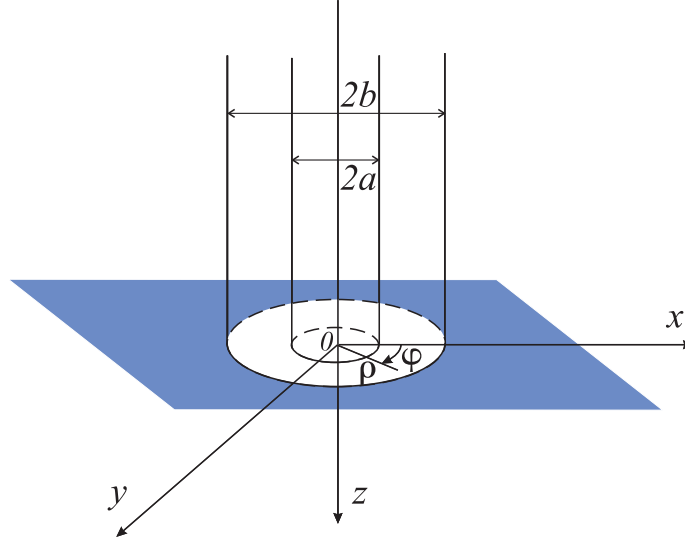
Figure 4.5: The plane $z = 0$ constitutes the interface between the coaxial waveguide ($z < 0$) and the sample space ($z > 0$), shown in Fig. 4.1. It serves as a reference plane, at which the reflection coefficient Γ, the impedance Z, and the admittance $Y = 1/Z$ of the sample are defined.

vector $\vec{k}$, that contains the searched complex dielectric function ε [1,2],

$$\frac{Y}{Y_0} = \frac{-ik^2}{\pi k_c \ln(b/a)} \int_a^b \int_a^b \int_0^\pi \cos\varphi \, \frac{\exp(ikr)}{r} \, \mathrm{d}\varphi \, \mathrm{d}\rho \, \mathrm{d}\rho', \qquad (4.5)$$

where

$$r = (\rho^2 + \rho'^2 - 2\rho\rho' \cos\varphi)^{1/2}, \qquad (4.6)$$
$$k^2 = \omega^2 \mu_0 \varepsilon_0 \varepsilon, \qquad (4.7)$$

and k_c and ε_c are, respectively, the wave vector and the dielectric constant of the insulation in the coaxial line with the characteristic admittance $Y_0 = 1/Z_0$, given by the Eq. (B.3).

For the sake of completeness of the present analysis, as well as due to the different sign conventions used in the relevant sources (cf. Ref. [103]) and the free-space case alone treated in the basic work by Levine and Papas [53], we briefly outline the four steps leading to the central equation (4.5), following in principle the Ref. [53].

---

[1]The dielectric function ε is defined relative to the vacuum permittivity ε_0 throughout this thesis.

[2]Throughout this thesis, a harmonic time dependence $\exp(-i\omega t)$ is assumed for the electromagnetic field, cf. Ref. [103].

Due to the radial symmetry of the waveguide and of the principal TEM mode, the only non-vanishing electromagnetic field components in the cylindrical coordinates are H_φ and E_ρ. The magnetic field component H_φ serves as a basic scalar function, and E_ρ is readily obtained using the Maxwell equations. Current and voltage in any cross section of the coaxial guide are given, respectively, by the line integrals of H_φ around the center conductor and of E_ρ between inner and outer conductors.

First, the field component $H_\varphi(\rho, z)$ is constructed separately for the coaxial region $z < 0$ and in the sample space $z > 0$, the latter as an integral expression in terms of the aperture electric field $E_\rho(\rho, 0)$. Next, one demands the continuity of those expressions for $H_\varphi(\rho, z)$ from both sides at the interface $z = 0$ and, thus, obtains an integral equation for the aperture field $E_\rho(\rho, 0)$. In the third step, the integral equation is rewritten in order to introduce current I and voltage U into it, and results in a variational expression for the aperture (or sample) admittance $Y = I/U$. As the last step, the variational principle is applied, i.e. an approximate solution for $E_\rho(\rho, 0)$ is inserted into the equation while the corresponding change in Y is kept small.

In the coaxial region, $a \le \rho \le b$, $z \le 0$, the expression for $H_\varphi^{(-)}(\rho, z)$ is

$$H_\varphi^{(-)}(\rho, z) = \frac{A_0}{\rho} \exp(ik_c z) + \Gamma \frac{A_0}{\rho} \exp(-ik_c z)$$

$$+ \sum_{n=1}^{\infty} A_n R_n(\rho) \exp(\gamma_n z) \quad , \tag{4.8}$$

$$k_c = \omega \sqrt{\mu_0 \varepsilon_0 \varepsilon_c} \quad . \tag{4.9}$$

The first two terms of Eq. (4.8) represent the incident and the reflected waves, and Γ is the reflection coefficient at the sample surface. The infinite series describes the exponentially damped higher order modes ($\gamma_n > 0$, $z \le 0$). The radial functions $R_n(\rho)$ describe the radial dependence of the higher order modes of the magnetic field, the concrete expressions for them are available in Ref. [104]. Together with $R_0(\rho) = 1/\rho$, the functions $R_n(\rho)$ constitute a complete orthonormal basis $\{R_n(\rho)\}$ of the space of twice differentiable functions in the aperture $a < \rho < b$, shown in Fig. 4.5. This property is being exploited once more in the current Section, further below. The coefficients A_0, A_n are readily obtained in terms of the aperture electric field $E_\rho(\rho, 0)$ by using the orthonormality of the radial functions $\{R_n(\rho)\}$ (see Refs. [53] and [104] for details),

$$A_0 = \frac{\omega \varepsilon_0 \varepsilon_c}{k_c} \cdot \frac{\int_a^b E_\rho(\rho, 0) \mathrm{d}\rho}{(1 - \Gamma) \ln(b/a)} , \tag{4.10}$$

$$A_n = \frac{i\omega \varepsilon_0 \varepsilon_c}{\gamma_n} \int_a^b E_\rho(\rho, 0) R_n(\rho) \mathrm{d}\rho . \tag{4.11}$$

Figure 4.6: Spatial distribution of the electric field amplitude at $f = 5$ GHz in a Si:P sample with dimensions shown in Fig. 4.1 and dielectric permittivity $\varepsilon_1 = 40$, which terminates a 2.4 mm microwave coaxial line. Computer simulation.

Figure 4.7: Spatial distribution of the electric field amplitude at $f = 10$ GHz in a Si:P sample with dimensions shown in Fig. 4.1 and dielectric permittivity $\varepsilon_1 = 40$, which terminats a 2.4 mm microwave coaxial line. Computer simulation.
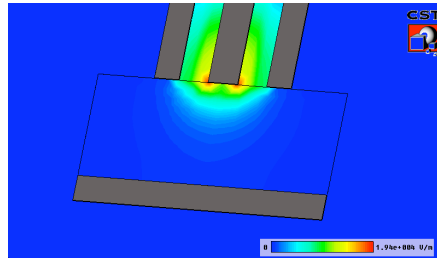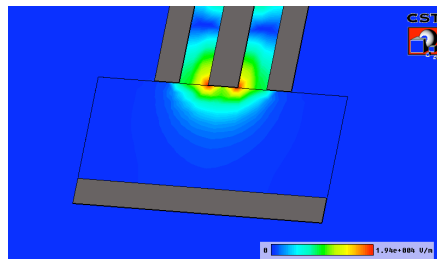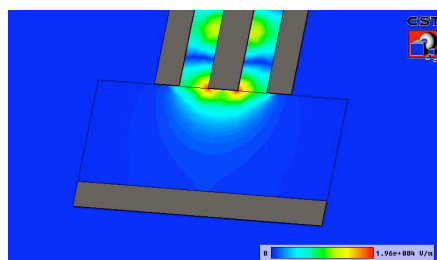

Figure 4.8: Spatial distribution of the electric field amplitude at $f = 20$ GHz in a Si:P sample with dimensions shown in Fig. 4.1 and dielectric permittivity $\varepsilon_1 = 40$, which terminates a 2.4 mm microwave coaxial line. Computer simulation.

In the sample half-space, $z \geq 0$, the integral expression for $H_\varphi^{(+)}(\rho, z)$ is derived by the Green's function method,

$$H_\varphi^{(+)}(\rho, z) = \frac{-i\omega\varepsilon_0\varepsilon}{\pi} \int_a^b \int_0^\pi E_\rho(\rho', 0)\, \rho' \cos\varphi \, \frac{\exp(ikr(z))}{r(z)} \, \mathrm{d}\varphi \, \mathrm{d}\rho' \,,$$
$$r(z) = (\rho^2 + \rho'^2 - 2\rho\rho'\cos\varphi + z^2)^{1/2} \,. \tag{4.12}$$

By setting $H_\varphi^{(-)}(\rho, 0) = H_\varphi^{(+)}(\rho, 0)$, the continuity of $H_\varphi(\rho, z)$ in the aperture is assured, cf. Figs. 4.6 - 4.8. The quantities of physical interest - current, voltage and, finally, admittance Y, - are introduced into the resulting integral equation. This is done by multiplying it with $\rho E_\rho(\rho, 0)$, integrating from $\rho = a$ to $\rho = b$, and normalizing the whole expression,

$$\frac{Y}{Y_0} = \frac{-ik^2 \ln(b/a)}{k_c \left[\int_a^b E_\rho(\rho, 0)\mathrm{d}\rho \right]^2} \left[\sum_{n=1}^\infty \frac{1}{\gamma_n} \left[\int_a^b E_\rho(\rho, 0)R_n(\rho)\rho \, \mathrm{d}\rho \right]^2 \right.$$
$$\left. + \frac{1}{\pi} \int_a^b \int_a^b \int_0^\pi \cos\varphi \, \rho E_\rho(\rho, 0)\rho' E_\rho(\rho', 0)\frac{\exp(ikr)}{r}\mathrm{d}\varphi \, \mathrm{d}\rho \, \mathrm{d}\rho' \right]. \tag{4.13}$$

For the equation (4.13), the variational principle for Y is applicable, cf. Ref. [53], because it is stationary with respect to the first variation of the aperture field $E_\rho(\rho, 0)$. In other words, the errors in Y are of the order of the squares of the errors in $E_\rho(\rho, 0)$. Thus, in our case, already the simplest approximation of $E_\rho(\rho, 0)$ in Eq. (4.13) by the leading term $R_0(\rho) = 1/\rho$ in the expansion by the orthonormal basis $\{R_n(\rho)\}$ suffices. Upon the corresponding insertion, each integral of the infinite series vanishes due to the orthogonality of the functions R_n with $n > 0$ and $n = 0$. The remaining expression is the Eq. (4.5).

The validity of the variational approximation [Eq. (4.5)] has been proven in Ref. [53] in the parameter ranges $0 < ka \leq 2$ and $1.57 \leq b/a \leq 4$ by comparison with experimental results. To obtain low-temperature microwave data on Si:P with widely varying phosphorus concentration n, we employ a coaxial probe of dimensions $2b = 1.75$ mm and $2a = 0.6$ mm, cf. Fig. 4.1. The maximum frequency range spans from 45 MHz to 40 GHz (limited by the source and test set of the network analyzer HP 8510) and the relative dielectric permittivity ε_1 reaches from 20 till 50, cf. Fig. 5.7. This corresponds to $0.001 \leq ka \leq 1.76$ and $b/a = 2.9$ and lies within the tested parameter range. The electric field distribution in a Si:P sample with $\varepsilon_1 = 40$ and dimensions as stated above is depicted using a computer simulation technology (CST) software at frequency values $f = 5$ GHz, 10 GHz and 20 GHz in Figs. 3.3, 4.6 - 4.8. Increase of the dielectric function affects the field distribution in a similar way as raising the microwave frequency, due to the wavelength dependence inside the sample via $\lambda \sim 1/\sqrt{\varepsilon_1}$. Dependence of the field distribution on ε_1 is, thus, not extra shown here.
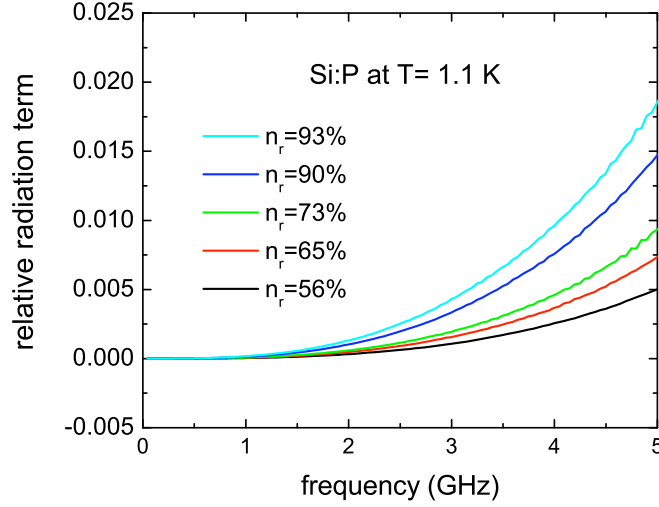
Figure 4.9: Relative contribution of the radiation term in Eq. (4.15), determined from the measured Si:P spectra at $T = 1.1$ K.

4.2.3 Solution of the inverse problem

The inverse problem of extracting ε from the measured impedance $Z = 1/Y$ by using the Eq. (4.5) has been solved in the quasi-static approximation by Misra [25] as follows[3]. For low frequencies, the exponential function in Eq. (4.5) can be approximated by the first four terms of its series expansion,

$$Y \approx \frac{-i2\omega\varepsilon_0\varepsilon}{[\ln(b/a)]^2} \int_a^b \int_a^b \int_0^\pi \left[\frac{\cos\varphi}{r} + ik\cos\varphi - \frac{k^2 r}{2}\cos\varphi \right. $$
$$\left. -i\,\frac{k^3 r^2}{6}\cos\varphi \right] \mathrm{d}\varphi\,\mathrm{d}\rho\,\mathrm{d}\rho'. \qquad (4.14)$$

The second term of Eq. (4.14) vanishes upon integration, and the last one is readily integrated; the integrals corresponding to the first and the third terms need to be numerically evaluated,

$$Y \approx \frac{-i2\omega\varepsilon_0\varepsilon}{[\ln(b/a)]^2}\left[I_1 - \frac{k^2 I_3}{2} \right] + \frac{k^3\pi\omega\varepsilon_0\varepsilon}{12}\left[\frac{b^2 - a^2}{\ln(b/a)} \right]^2, \qquad (4.15)$$

where

$$I_1 = \int_a^b \int_a^b \int_0^\pi \frac{\cos\varphi}{(\rho^2 + \rho'^2 - 2\rho\rho'\cos\varphi)^{1/2}}\mathrm{d}\varphi\,\mathrm{d}\rho\,\mathrm{d}\rho'$$

---

[3]For the different choice of sign convention see Appendix A and Ref. [103].

Table 4.1: Geometrical integrals for the coaxial probe dimensions $2a = 0.6$ mm and $2b = 1.75$ mm, numerically determined using MATLAB.

I_1 (mm)	I_3 (mm^3)	I_4 (mm^4)	I_5 (mm^5)
0.9084	-0.2100	$-(\pi/4)0.4001$	-0.4047

and

$$I_3 = \int_a^b \int_a^b \int_0^\pi \cos\varphi \, (\rho^2 + \rho'^2 - 2\rho\rho' \cos\varphi)^{1/2} \mathrm{d}\varphi \, \mathrm{d}\rho \, \mathrm{d}\rho' .$$

In our special case, the relative contribution of the last term in Eq. (4.15) to Y is below 2% up to 5 GHz for all the reported Si:P samples (cf. Fig. 4.9 and Tab. 5.1) and the formula, thus, reduces to a quadratic equation for ε,

$$\frac{1}{Z} = Y = \frac{-i2\omega\varepsilon_0\varepsilon}{[\ln(b/a)]^2} \left[I_1 - \frac{\omega^2 \mu_0 I_3 \varepsilon_0 \varepsilon}{2} \right] . \tag{4.16}$$

The values of the geometrical integrals, numerically determined using MATLAB for the special case of the coaxial probe with the inner and outer conductor diameters $2a = 0.6$ mm and $2b = 1.75$ mm are listed in Tab. 4.1. It should be mentioned that the integrand of I_1 diverges at $\rho = \rho'$, $\varphi = 0$. That integral was numerically evaluated as the limit of a series of integrals $\{I_{1,n}\}$ which lower bounds φ_n converge to $\varphi = 0$.

4.3 Our expression for the frequency dependence of the open calibration standard

The frequency dependence of the open calibration standard with a known dielectric function ε can be obtained as follows [15]. The expression (4.5) of the admittance Y as a function of ε correctly describes the open standard admittance as long as the effect of the finite sample dimensions is negligible. By using a Teflon block of the form shown in Fig. 4.1 (the same as for the Si:P samples) and assuming its dielectric function to be $\varepsilon = 2.03(1 + i\,0.0002)$ in the gigahertz frequency range, as in Ref. [105], the maximum electric field strength at the depth of 2 mm turns out to be far below 0.01 of its value at the sample surface for frequencies up to 10 GHz, so that the secondary reflections at the back side of the open standard can be neglected here.

To obtain a closed expression $Y^{\mathrm{open}}(\omega)$ from the integral equation (4.5), the series expansion of the exponential function can be used as in the previous section.

In contrast to the inverse problem discussed in Sec. 4.2, there is no need to spare at the accuracy early truncating the series here. The relative contributions of the terms, subsequent to the fifth term, are far below 10^{-4} up to 10 GHz. Thus, the ultimate expression we use is,

$$Y^{\text{open}} \approx \frac{-i2\omega\varepsilon_0\varepsilon}{[\ln(b/a)]^2} \left[I_1 - \frac{1}{2}k^2 I_3 - \frac{i}{6}k^3 I_4 + \frac{1}{24}k^4 I_5 \right], \tag{4.17}$$

where

$$I_4 = -\frac{\pi}{4}(b^2 - a^2)^2 \, ,$$

$$I_5 = \int_a^b \int_a^b \int_0^\pi \cos\varphi \, (\rho^2 + \rho'^2 - 2\rho\rho'\cos\varphi)^{3/2} \mathrm{d}\varphi \, \mathrm{d}\rho \, \mathrm{d}\rho' .$$

and k is defined in Eq. (4.7). The values of the geometrical integrals for the 2.4 mm coaxial probe are listed in Table 4.1.

The frequency-dependent reflection coefficient Γ^{open} of the open calibration standard follows by using Eq. (3.2),

$$\Gamma^{\text{open}} = \frac{Z^{\text{open}} - Z_0}{Z^{\text{open}} + Z_0} = \frac{Y_0 - Y^{\text{open}}}{Y_0 + Y^{\text{open}}} . \tag{4.18}$$

The effect of the frequency dependence of Γ^{open} on the conductivity σ_1 and permittivity ε_1 spectra compared to the dc assumption $\Gamma^{\text{open}} = 1$ is demonstrated in Figs. 4.3 and 4.4 on the example of two Si:P samples with donor concentrations n/n_c of 0.56 and 0.9 relative to the concentration value at the metal-insulator transition, $n_c = 3.5 \times 10^{18}$ cm^{-3}. For samples with larger dielectric constant ε_1 and higher losses σ_1, as n/n_c rises, the influence of this correction slightly decreases. This is also what one would expect when the electric properties of the material under investigation approach the metallic characteristics.

Chapter 5

Experimental results for the frequency-dependent hopping transport in Si:P in the zero-phonon regime and at elevated temperature, with a discussion

In this Chapter we describe our results for the dynamic transport in Si:P at effectively zero temperature in the insulating regime, where the underlying electronic states provided by the donor impurities are assumed strongly localized, as described in Sec. 2.1 of the Theory Chapter. Thermal effects, which set in when the temperature is elevated from our base temperature of 1.1 K, are also discussed here. With the experimental setup specified in Sec. 3.3 of Chapter 3, measurements of the complex reflection coefficient have been performed on Si:P samples with donor concentrations n from 56 % to 90 % of the critical concentration $n_c = 3.5 \times 10^{18}$ cm^{-3} of the zero-temperature metal-insulator transition [8]. The determination of the critical dopant density n_c in Si:P by Stupp et al. [8] appears most reliable and has been accepted by the community active in the field. (In older literature sources, a higher value of 3.72×10^{18} cm^{-3} can be found.) The obtained spectra have been evaluated by the advanced data analysis method, developed in Chapter 4 and also presented in our publication [15]. For all the reported Si:P samples, summarized in Tab. 5.1, the zero-phonon regime could be identified at our lowest measurement temperature of 1.1 K, see Sec. 5.2 further below. Thus, theoretical models for the variable-range hopping in a disordered system at effectively zero temperature with electron-electron interactions, cf. Sec. 2.1 of the Theory Chapter, are appropriate to interpret the electric
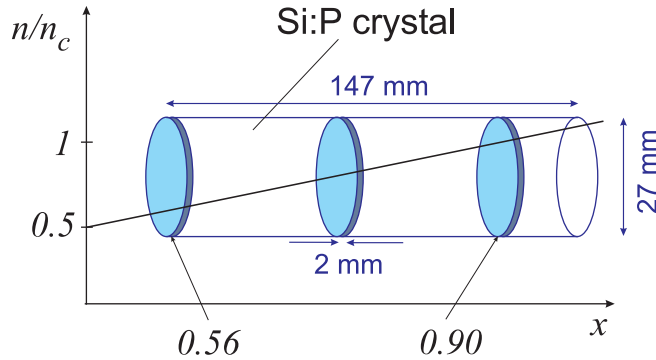
Figure 5.1: Si:P samples were cut from a 147 mm long Czochralski-grown cylindrical single crystal [106], with a dopant density gradient along its growth axis. Disc-shaped samples, 2 mm thick, of varying donor concentration n/n_c from 0.56 to 0.9 were obtained, relative to the critical value of the metal-insulator transition $n_c = 3.5 \times 10^{18}$ cm^{-3}. From those thin disc-shaped slices, the smaller dice-shaped samples shown in Fig. 5.2 were cut for the microwave spectrometer.

conductivity spectra, as also presented in our publications [15] and [16].

5.1   Si:P samples

Si:P samples for this study stem from a commercial Czochralski-grown cylindrical crystal [106], 147 mm long with a diameter of 27 mm, nominally uncompensated, with a mean phosphorus concentration gradient of $\partial n(x)/\partial x \sim 0.12 \times 10^{18}$ cm^{-4} along its axis. Cutting out thin slices (2 mm thick) with faces perpendicular to the crystal growth axis, as depicted in Fig. 5.1, we obtained relatively homogeneously doped Si:P samples of varying dopant density n from 1.97×10^{18} to 3.14×10^{18} cm^{-3}. To get rid of the distorted surface layers [33, 107], the samples were chemically and mechanically treated by well established procedures by G. Untereiner [108].

The main characteristic of the Si:P samples, the dopant density n, is extremely difficult to obtain directly and was, as usual, determined by its relation to the room-temperature direct current resistivity $\rho_{dc}(300\text{K})$, measured with a commercial four-probe measurement system (FPP 5000 by Veeco Instruments) in the master thesis by Anung [109] and in the diploma thesis by Hering [110], with the relative error $\triangle n/n$ estimated to lie below 3 %. While contact resistance is of no significant complication for the four-point resistance measurements, the geometrical shape of the sample is crucial by the calculation of the resistivity from the resistance. Correction formulae for samples of finite size with a thin disc shape like in Fig. 5.1, provided in the documentation of the instrument FPP 5000, have been employed to that end.
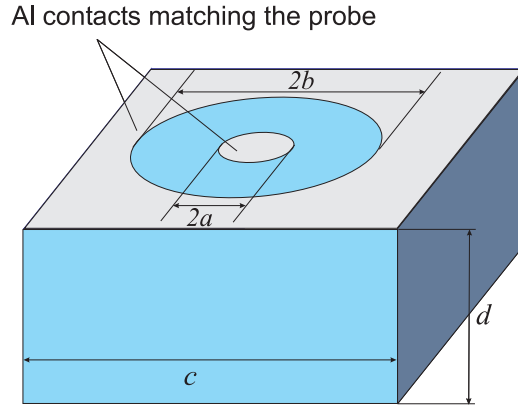
Figure 5.2: Sketch of a dice-shaped Si:P sample with the aluminum contact layer (light grey), evaporated on top of it. $2a = 0.6$ mm, $2b = 1.75$ mm, corresponding to a 2.4 mm microwave coaxial adapter; $c = 5$ mm, $d = 2$ mm. The commercial Si:P crystal, from which those samples were cut, is depicted in Fig. 5.1.

Table 5.1: Donor concentration n and the value of the room-temperature dc resistivity ρ_{dc} of the reported Si:P samples, after Refs. [109, 110]. The second column lists the relative donor concentration with respect to the critical value $n_c = 3.5 \times 10^{18}$ cm^{-3} of the zero-temperature metal-insulator transition [8]. The listed results for the exponent α of the conductivity power law $\sigma_1(\omega) \sim \omega^{\alpha}$ and the full relative dielectric constant ε_1, obtained in the present work, are also displayed in Figs. 5.4 and 5.7. (The dielectric constant ε_1 is defined relative to the vacuum permittivity ε_0.)

| n | n/n_c | $\rho_{dc}(300$ K$)$ | α | ε_1 |
$(10^{18}$ cm$^{-3})$		$(\Omega$ cm$)$		
1.97	0.56	0.0162	1.13	23.5
2.29	0.65	0.0149	1.16	24.7
2.57	0.73	0.0139	1.10	29.5
2.91	0.83	0.0130	1.08	33.4
3.04	0.87	0.0127	1.05	42
3.14	0.90	0.0124	1.04	43.4

For the conversion from the resistivity $\rho_{dc}(300$K$)$ to the donor density n, the Thurber scale [111] was used, that is a least squares fit of an analytical rational function to experimental data in a very broad doping range from 10^{13} to 10^{20} cm^{-3} at room temperature. The data used by Thurber et al. comprise donor concentration values obtained by four different measurement techniques, best suited in different overlapping doping ranges, as well as room-temperature resistivity values obtained by careful four-probe measurements on the same Si:P

samples. In the interval from 10^{18} to 10^{19} cm^{-3}, which is relevant for us, the Thurber scale is based on chemical measurements of phosphorus density by the neutron activation analysis on Si:P samples with donor concentrations from 10^{15} to 10^{20} cm^{-3} and by the photometric technique from $2{\times}10^{17}$ to $5{\times}10^{19}$ cm^{-3}. Chemical methods yield the phosphorus density solely, while electrical methods give electrically active density that may be affected by unwished factors like incomplete donor electron ionization or compensation through acceptors. For this and further reasons, found in Ref. [111], the range suited for the Hall coefficient measurement was restricted by Thurber et al. to the metallic samples with P concentrations from 10^{19} cm^{-3} on, and the range for the capacitance-voltage (C-V) measurements on junction diodes to dopant density up to 10^{18} cm^{-3}. To characterize highly doped Si:P samples, a resistivity ratio $\rho_{\mathrm{dc}}(4.2\mathrm{K})/\rho_{\mathrm{dc}}(300\mathrm{K})$ (determined from standard dc measurements) is more sensitive to dopant density changes due to high resistivity values at low temperatures. The spline fit of the corresponding resistivity ratio values plotted against the donor concentration, pre-determined using the Thurber scale, serves as a more precise calibration curve (see for more detail the works by Stupp [112] and by Hornung [113]). Low temperature dc measurements on our highly doped Si:P [109] samples are consistent with the Refs. [112, 113].

Si:P samples with dimensions $5{\times}5{\times}2$ mm^3 as in Fig. 5.2, suited for the microwave spectrometer, have been cut from the disc-shaped samples, which are shown in Fig 5.1 and characterized as described above. For those dice-shaped Si:P samples, no significant variation of the low-temperature microwave conductivity values was detected from sample to sample, as long as they stemmed from the same disc. This fact confirms the assumption of sufficient homogeneity of the dopant density inside the thin discs shown in Fig. 5.1, at least for our project reported here with the parameter range listed in Tab. 5.1.

The problem of the additional contact area resistance (mainly due to the growth of a thin oxide layer on the Si:P surface exposed to the air) is usually overcome in the dc measurements by the employment of the four-point method. In contrast to that, our frequency-dependent measurement of the complex sample impedance (or its reflection coefficient) has a two-point geometry shown in Figs. 3.1 and 5.2, i.e. the contact resistance is connected in series with the sample impedance. To avoid the disturbing increase of the measured impedance, careful optimization of the sample preparation procedure was carried out [108]. It resulted in the following steps, performed without any delay in-between, each time the new contacts needed to be evaporated on the Si:P samples for the microwave measurements described in Chapter 3,

- Removal of the old Al contacts.

- Surface polishing with the coarse-grained diamond paste (7 μm).

- Fine polishing using a polishing cloth with 1 μm diamond dust.

- Processing with the dilute hydrofluoric acid.

- Evaporation of a 100 nm Al contact layer using a mask with the dimensions as in Fig. 5.2.

5.2 Low-temperature ac measurements

Our frequency range from 100 MHz to 5 GHz for the reflection coefficient measurements contains 300 frequency points: 200 equidistant points from 0.1 GHz to 1 GHz and 100 points from 1 GHz to 5 GHz. The spectra were taken at the base temperature 1.1 K of our ^{4}He-pumped cryostat, as well as at elevated temperatures using the Temperature Controller Lake Shore 340 heating the setup up to room temperature in an automatized procedure. The experimental setup is described in detail in Sec. 3.3 of Chapter 3. In order to ensure the correct functionality of the spectrometer, test spectra of thin metallic NiCr films were measured, with test results for the whole low-temperature measurement (shown in Fig. 3.7) lying within two weeks from each Si:P sample measurement and within a few days as concerns the room temperature tests. Since no frequency dependence is expected for the conductivity of a normal metal below the optical range (Drude behavior, cf. e.g. Ref. [18]), metallic spectra yield a perfect indicator for spurious frequency dependences due to any problems with the apparatus or with the prepared calibration samples (cf. Sec. 3.1 and Ref. [108]). All Si:P samples reported in this thesis prove to be in the zero-phonon regime at $T = 1.1$ K, exhibiting a saturation of $\sigma_1(T)$ and $\varepsilon_1(T)$ in the whole measured frequency range as $T \to 1.1$ K. This is demonstrated in Fig. 5.5 at the example of the conductivity $\sigma_1(T)$ at fixed frequency values of 150 MHz and 1 GHz, measured for a Si:P sample with the relative donor concentration n/n_c of 0.83.

For each dopant density n, four to ten independent measurements have been performed. From the best spectra (lowest noise and smallest influence of standing waves) mean values of the conductivity power law exponent α and of the dielectric constant ε_1 have been determined, shown in Figs. 5.4 and 5.7.

5.3 Frequency dependence of the conductivity in the zero-phonon regime

In Fig. 5.3 the measured real part σ_1 of the frequency-dependent conductivity of Si:P samples with the relative donor concentrations n/n_c of 0.65, 0.83 and 0.9 is plotted on a log-log scale to identify the power law. The fits by the two-parameter function $\sigma_1(\omega) = \mathrm{const} \cdot \omega^\alpha$ are shown by the dashed lines. In Fig. 5.4 the mean
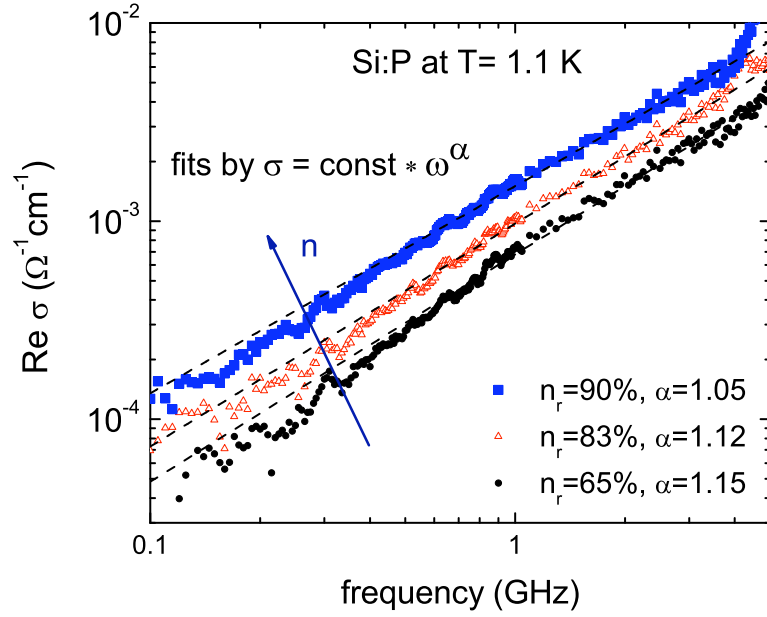
Figure 5.3: Typical spectra of the measured real part σ_1 of the conductivity of Si:P with relative donor concentrations n/n_c of 0.65, 0.83 and 0.90 at 1.1 K. ($n_c = 3.5 \times 10^{18}$ cm^{-3} corresponds to the zero-temperature metal-insulator transition.) The log-log scale is chosen to identify the conductivity power law. The dashed lines are the fits by a two-parameter power law function.

Figure 5.4: Conductivity power law exponent α, cf. Tab. 5.1, obtained from the fit with the function $\sigma_1(\omega) = \text{const} \cdot \omega^\alpha$, averaged over all the spectra taken on Si:P samples of a given dopant density n at 1.1 K, cf. Fig. 5.3. The error bars represent the corresponding standard error.
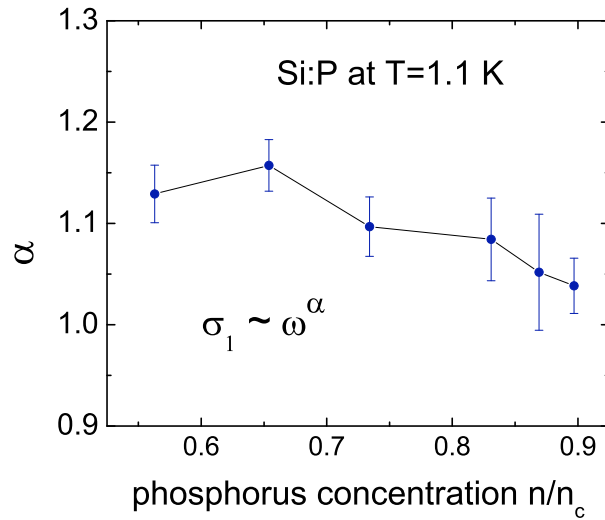
values of the exponent α are plotted against the relative donor concentration n/n_c. The frequency dependence of the conductivity clearly follows a superlinear power law in the whole reported doping range, while the exponent slightly decreases with dopant density. From $\alpha > 1$ we infer that the hopping transport takes place deep inside the Coulomb gap, corresponding to the Eq. (2.15) known from the theory.

The main source for the error bars in our case lies in the extensive calibration procedure described in Chapter 3. Due to the necessity of a complete cool down and heat up cycle for each of the three calibration standards, both contributions, the self-made calibration sample preparation instead of using a commercial calibration kit as well as performing an identical low temperature experiment on four different days, contain rather high statistical errors. The latter result in a standard error, shown in Figs. 5.4 and 5.7 as a root mean square deviation from the mean values of the most sensitive parameters of the complex conductivity spectra (the power law exponent α of the frequency dependence characterizes the real part σ_1, while the dielectric constant ε_1 comprises the imaginary part σ_2, see Sec. 5.5 further below).

A superlinear conductivity power law was previously also observed in Si:As and Si:P by Castner and collaborators [43, 44], who were using resonator techniques at several fixed frequency values within the range of the present work. Our results are also in accord with the transmission measurements by Hering et al. [34, 110] at higher frequencies (30 GHz to 3 THz), obtained by quasioptical techniques on samples cut from the same Si:P crystal [106]. In contrast to that, a sublinear frequency dependence in the zero-phonon regime has been reported by Lee and Stutzmann [78] based on experiments on Si:B in the microwave range and by Helgren et al. [32, 33] with quasioptical techniques in the terahertz range. While Lee et al. [78] are to our knowledge the only predecessors who measured an insulating semiconductor at low temperatures with a broadband microwave reflection measurement technique, their evaluation method is that suited for metallic samples only and resulted in extremely high conductivity values, as mentioned in Sec. 3.2 of Chapter 3. The complexity of the frequency-dependent measurements employing the resonator techniques consists in the independence of the experimental setup for different frequency points. Besides, the resulting spectra are then based on just about a dozen of measurement points. Nevertheless, it is even less points (between five and ten) in the transmission measurements reported by Helgren et al. for the interacting system, while our frequency range contains 300 measurement points distributed over almost two decades in frequency, as described at the beginning of Sec. 5.2. The results by Hering et al. [34, 110], which support our interpretation, are also based on more than three times as many frequency points in the regime of correlated electrons, than in a similar experiment performed by Helgren et al. [32, 33].
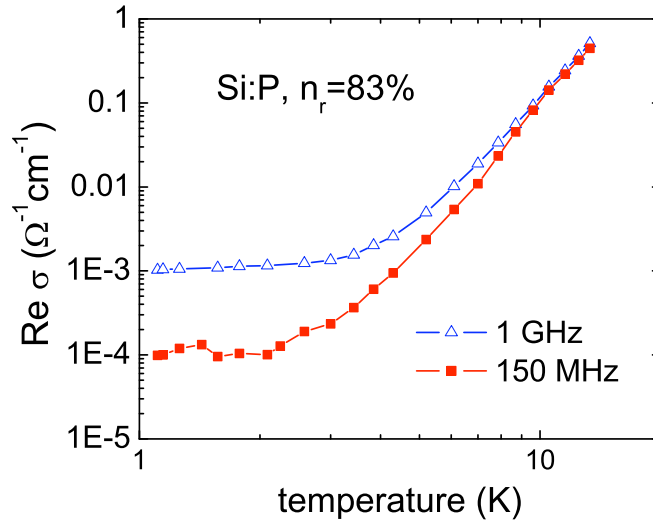
Figure 5.5: Temperature dependence of the conductivity σ_1 at fixed frequency values of 150 MHz and 1 GHz at the example of the relative dopant density $n/n_c = 0.83$, typical for all the investigated Si:P samples. The onset of the thermal effects depends on the phosphorus concentration: the higher the doping, the lower the temperature at which the temperature dependence sets in.

5.4 Temperature dependence of the conductivity

Leaving the zero-phonon regime behind by raising temperature, we observed a gradual increase of the conductivity σ_1 for all investigated Si:P samples. First, the temperature dependence is approximately linear in agreement with the prediction by Austin and Mott [1, 114]. With further growing T, it gradually becomes stronger until the charge carrier activation into the conduction band dominates over the hopping transport, cf. Fig. 2.1. The onset of the thermal effects depends on the phosphorus concentration: the higher the doping, the lower the temperature at which the temperature dependence sets in. But the way it happens is the same for all the Si:P samples we have measured.

Taking the example of the relative donor concentration $n/n_c = 0.83$, we have plotted the conductivity values σ_1 in Fig. 5.5 at fixed frequencies of 150 MHz and 1 GHz. At the low end of our frequency range, represented by $f = 150$ MHz, the conductivity of that relatively highly doped Si:P sample stays temperature-independent up to 2 K. For higher frequencies, the onset of the thermal effects shifts to still higher temperatures. Above $T = 10$ K both curves corresponding
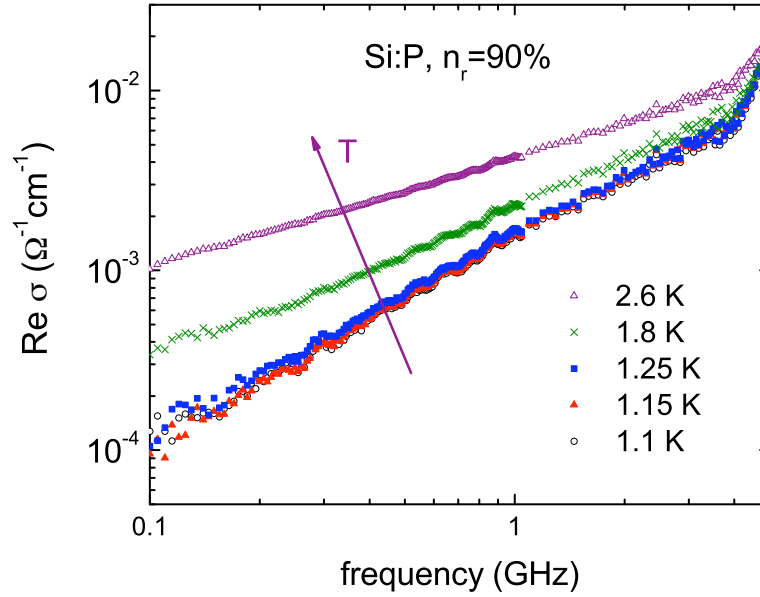
Figure 5.6: Temperature dependence of the conductivity spectra typical for all the investigated Si:P samples at the example of the highest reported relative donor concentration of $n/n_c = 0.9$. The opposite extreme of our lowest relative dopant density, $n/n_c = 0.56$, yields an almost identical picture (not shown here), with the only difference that the spectra stay completely unchanged up to the temperature as high as 7 K.

to the very different frequencies merge into one, meaning that the thermal activation dominates over the photon energy for $T > 10$ K.

In Fig. 5.6 the frequency-dependent conductivity σ_1 is plotted for different temperatures for a Si:P sample with the highest relative donor concentration $n/n_c = 0.9$ in this thesis. The conductivity power law exponent α gradually decreases with rising temperature, which is plausible, since the thermal energy scale $k_{\mathrm{B}}T$ grows with respect to the photon energy $\hbar\omega$ and starts to dominate. Without showing the very similar pictures obtained for lower dopant density in Si:P, we point out the only significant difference, taking the example of the Si:P samples with our lowest dopant density of 56 %: The spectra of the complex conductivity in the latter case stay completely unchanged up to the temperature as high as 7 K.

The transition to a sublinear power law upon raising T is in accord with previous observations [44, 114, 115]. Moreover, Pollak et al. [115] document for precise radio-frequency measurements of the complex capacitance on weakly doped Si:P and similar compounds, that a slowly decreasing slope of $\sigma_1(\omega)$ with growing temperature is typical for all the conductivity spectra. To our knowledge, a theoretical description for a gradual decrease of the exponent α is lacking though. It
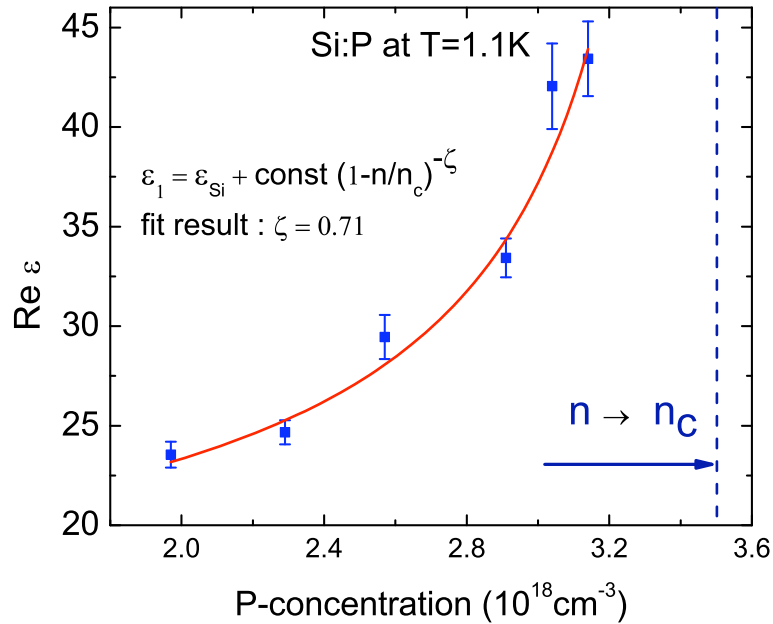
Figure 5.7: Dependence of the full relative dielectric constant ε_1 of Si:P in the zero-phonon regime on the donor concentration n, cf. Tab. 5.1. The solid line is the fit with the power law function, cf. Eq. (2.18), for the donor electron contribution $(\varepsilon_1 - \varepsilon_{Si})$, where $\varepsilon_{Si} = 11.7$ [56].

is probably extremely difficult to handle a theoretical model where both energy scales, frequency $\hbar\omega$ and temperature $k_B T$, are varied. Thus, the models yielding analytic formulae for the conductivity in a broad parameter range, describe either the dynamic behavior in the zero-phonon regime $\sigma_1(\omega)$ or the thermally activated direct current conductivity $\sigma_{dc}(T)$.

5.5   Dielectric function

From our experiments on Si:P in the zero-phonon regime, we find that the real part of the dielectric function[1] ε_1 is independent of frequency in the range of 50 MHz –10 GHz (cf. Figs. 4.4 and 5.8), taking the measurement uncertainty into account. A fit with the scaling function (2.18) results in an exponent $\zeta = 0.71$, as shown in Fig. 5.7.

In the framework of the effective medium approximation, $\zeta = 1$ is expected from the theory [55]. As mentioned in the Sec. 2.1.3 of the Theory Chapter, the non-zero frequency of our measurement $\omega/2\pi \geq 45$ MHz leads to a smoothing

---

[1]The dielectric function ε is defined relative to the vacuum permittivity ε_0 throughout this thesis.
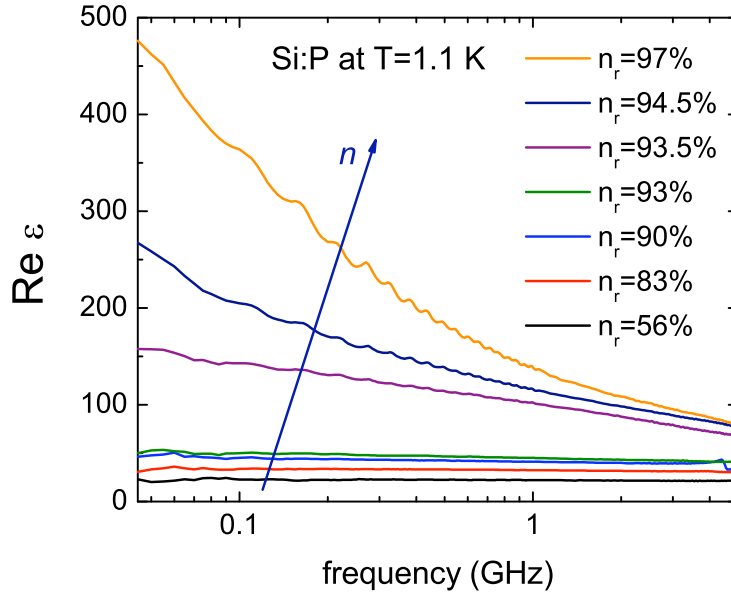
Figure 5.8: Dependence of the dielectric function spectra of Si:P at 1.1 K on the relative donor concentration n/n_c, with respect to the critical value $n_c = 3.5 \times 10^{18}$ cm^{-3} of the zero-temperature metal-insulator transition. The samples with the high doping above 90% lie beyond the scope of the present thesis and are only shown to prove that the inequality (2.19) holds for all of the reported Si:P samples with relative dopant density $n/n_c < 0.9$.

of the dielectric divergence, present for $\omega = 0$ at the critical donor concentration n_c of the metal-insulator transition, to a continuos function $\varepsilon_1(\omega, n)$ of the donor concentration n, as shown in Fig. 2.7. For parameter values $n/n_c \leq 0.9$, relevant in the present thesis, the inequality (2.19) holds in the whole frequency range reported, as can be seen from the Fig. 5.8. In that figure, the spectra of the dielectric function $\varepsilon_1(\omega, n)$ for donor concentration values close to the metal-insulator transition have been plotted together with those for the lower dopant density $n/n_c < 0.9$, which are reported in the present work, at 1.1 K. A smaller exponent ζ, obtained from a fit of our data to the scaling equation (2.18), than that predicted by the theory, is very likely caused by the considerable distance from the transition point n_c, which cannot be approached much closer at the high frequency of our experiment due to the restriction imposed by the inequality (2.19). Strictly seen, the scaling relation described by the Eq. (2.18) is only predicted close to the metal-insulator transition point n_c of the dopant density.

From the quasioptical experiments on Si:P in the terahertz range (i.e. at higher frequency) and on more dilute samples than in our work, different results are reported. Helgren et al. [33] observed a similar dependence of the values of the dielectric constant on the donor concentration (though uniformly shifted to
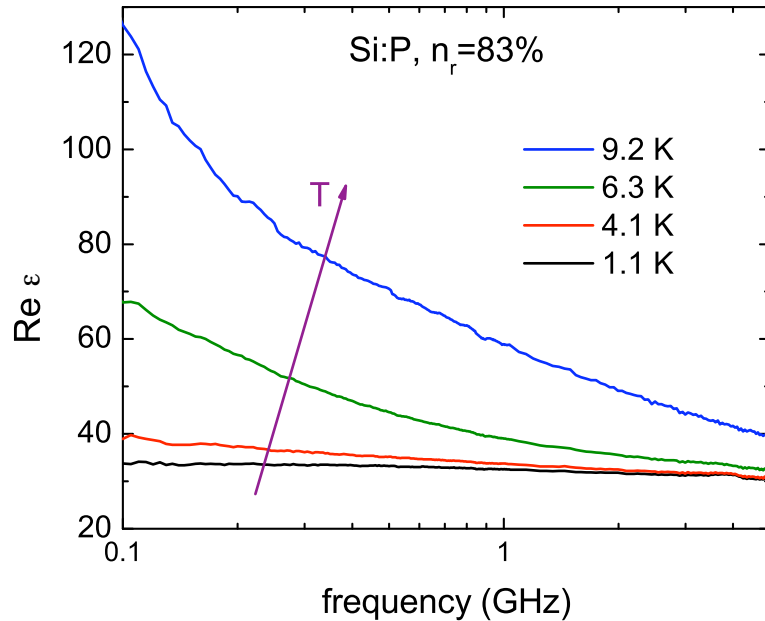
Figure 5.9: Temperature dependence of the dielectric function ε_1 typical for all the measured Si:P samples, at the example of the relative donor concentration $n/n_c = 0.83$.

lower values by 8). Hering et al. [34] have observed values of ε_1 as we have but with a much stronger dependence of the dielectric constant on dopant density, resulting in a much higher exponent $\zeta = 1.68$. It is obvious that this discrepancy still calls for further experiments which are more accurate as far as this analysis is concerned. In particular, the frequency range should be further lowered to study the divergence of the dielectric constant $\varepsilon_1(\omega = 0, n)$ (cf. Fig. 2.7 and e.g. the standard textbook by Dressel and Grüner [18]) and the metal-insulator transition should be further approached.

Leaving the zero-phonon regime behind at elevated temperatures, we observe the dielectric function spectra of Si:P to rise in the whole frequency range we measured, as shown in Fig. 5.9 at the example of the relative dopant density $n/n_c = 0.83$. This can be accounted for by the relaxation processes due to the phonons, which gain weight with rising temperature. As soon as the slope of the corresponding conductivity spectra $\sigma_1(\omega)$ drops below 1, the spectra of the dielectric function $\varepsilon_1(\omega)$ exhibit a rapid ascent to the lower frequencies, tending to diverge; this effect becoming stronger with further increase of T. In analogy to the conductivity spectra, the onset of those thermal effects is shifted to higher temperatures for lower dopant density, while the general way the spectra change is similar for all the Si:P samples. The divergence of the dielectric function, as frequency tends to zero, is also what is expected in the case of a sublinear con-

ductivity power law α from the Kramers-Kronig relations[2], cf. Ref. [116]. In the case of $\alpha < 1$, the Kramers-Kronig compatible form of the complex conductivity (provided, the power law is observed over a wide frequency range) implies the same power law for the real and imaginary parts:

$$\sigma = \sigma_1 + i\sigma_2 = A(i\omega)^\alpha = A\,\omega^\alpha \cos\left(\frac{\pi\alpha}{2}\right) + iA\,\omega^\alpha \sin\left(\frac{\pi\alpha}{2}\right) , \qquad (5.1)$$

as has already been pointed out earlier by Pollak et al. [115] or Helgren et al. [33]. A sublinear frequency dependence of σ_2 corresponds via Eq. (2.16) to a diverging real part of the dielectric function ε_1 as $\omega \to 0$.

---

[2]The Kramers-Kronig relations, cf. e.g. the standard textbook by Kittel [36], comprise an integral relation between the real and the imaginary parts of any physical response function, such as the complex dielectric susceptibility $\chi = \varepsilon - 1$, responsible for dielectric polarization in the formula for the electrical displacement $D = \varepsilon_0 \varepsilon E$ in the electric field E.

Chapter 6

Conclusions and outlook

Aiming at the low-temperature studies of the complex broadband dynamic response $\sigma(\omega)$ of the insulating doped semiconductors in the gigahertz range, we have thoroughly analyzed the problem of extracting the electrical conductivity σ_1 and the dielectric permittivity ε_1 from the complex reflection coefficient measurement in the microwave range with a vector network analyzer. While simple relations between the measured impedance Z and the searched material parameters are readily available for metallic or superconducting samples, which admit a straightforward data evaluation in those cases, up to now this powerful experimental technique could not be adequately applied to semiconducting and insulating materials under test. Although the absolute value of the complex reflection coefficient is nearly unity for an insulator with low electrical losses, $|\Gamma^{open}| \approx 1$, the electric field penetrates over an appreciable distance in such a sample and builds a three-dimensional field distribution inside it, that is quite different from that of a plane wave. A representative example of the electric vector field inside an insulating semiconducting sample ($f = 5$ GHz, $\varepsilon_1 = 40$, $\varepsilon_2/\varepsilon_1 < 0.001$) is demonstrated in Fig. 1.1.

As a first attempt to solve the problem, already our static model for the current distribution in a semiconducting sample with a simplified vector field configuration, shown in Fig. 4.2, has led to a reasonable data evaluation in the low frequency range up to 1 GHz. As our main methodic result, we present a rigorous analytical solution to the problem, in form of a closed procedure for the calibration and evaluation of data, obtained from the reflection coefficient measurement of an insulating semiconductor in the microwave range at low temperature. Basically no restricting assumptions are needed in a broad interval of the parameters, which determine the electromagnetic field distribution in the sample: the microwave frequency $\omega = 2\pi f$ and the complex dielectric constant $\varepsilon = \varepsilon_1 + i\varepsilon_2$ of the material. With our evaluation method, presented in our publication [15], we are now able to measure the complex ac conductivity $\sigma = \sigma_1 + i\sigma_2$ (or the complex dielectric function $\varepsilon = \varepsilon_1 + i\varepsilon_2$) of doped semiconductors in

the broadband frequency range from 0.1 to 5 GHz at temperature of 1.1 K and above in a broad interval of dopant density n below the metal-insulator transition.

We applied the developed data analysis to study the dynamics of donor electron states in Si:P with a dopant density n from 56 % to 90 %, relative to the critical value $n_c = 3.5 \times 10^{18}$ cm^{-3} of the $T = 0$ metal-insulator transition, and obtained the following results for the three main issues of interest, mentioned in the Introduction. Those results are also already published in our papers [15, 16],

1. All of the reported Si:P samples prove to be in the zero-phonon regime at our base temperature of 1.1 K. The conductivity $\sigma_1(\omega, n, T)$ of those samples, measured at 1.1 K, exhibits a superlinear frequency dependence in the frequency interval stated above under a careful consideration of the experimental error bars. From this we infer, that in the corresponding parameter range the Coulomb interaction $U(r_\omega)$ dominates over the photon energy $\hbar\omega$ and the hopping transport of the interacting electrons takes place inside the Coulomb gap $\triangle$ around the Fermi level.

2. The dielectric function $\varepsilon_1(\omega, n, T)$ of all the reported Si:P samples proves to be a constant with respect to the microwave frequency f and temperature T at 1.1 K as far as the measurement uncertainty of our technique reaches. The corresponding value $\varepsilon_1(n)$ of the dielectric constant at 1.1 K is observed to rapidly increase with growing doping, the donor electron contribution $(\varepsilon_1 \text{-} \varepsilon_{\text{Si}})$ follows a power law $|n - n_c|^{-\zeta}$ with the value of the exponent $\zeta = 0.71$ obtained from our experiment. This is also what one expects, since the donor electron contribution to the dielectric relaxation should rise with the increasing dopant density.

3. The conductivity power law exponent α gradually decreases with rising temperature T for all the reported Si:P samples, as soon as the zero-phonon regime is left behind for a given dopant density n. The way the spectra $\sigma_1(\omega, n, T)$ rise with growing T is the same for all the Si:P samples we measured, with the only difference that for lower doping n the thermal effects set in at a higher temperature. While a sublinear frequency dependence of the conductivity σ_1 is also expected from the theory for a thermally assisted ac hopping transport, a theoretical description of a gradual decrease of the conductivity power law with rising T is lacking. Available theoretical predictions handle only distinct limiting cases, while we have covered a broad range of the parameters (ω, n, T) in our experiment. Qualitatively, the described behavior of the conductivity spectra of Si:P appears plausible to us: With growing temperature T the frequency dependence of the conductivity $\sigma_1(\omega, n, T)$ becomes weaker due to the growing role of the thermal energy $k_{\text{B}}T$ compared to the photon energy $\hbar\omega$.

Similar to the conductivity spectra $\sigma_1(\omega, n, T)$, the spectra of the dielectric function $\varepsilon_1(\omega, n, T)$ rise with growing temperature T as soon as the zero-phonon regime is left behind. The way the spectra change with respect to T is, again, qualitatively identical for all the Si:P samples measured. The frequency dependence of the dielectric function ε_1 is in accord with that of the real part σ_1 of the conductivity as concerns the integral Kramers-Kronig relations between the real and imaginary parts of the complex response function $\sigma = \sigma_1 + i\sigma_2$.

Based on the methodical and experimental results of the work, constituting the present thesis, the project of the broadband microwave spectroscopy on semiconducting materials at low temperature can be further developed in several encouraging directions. Beside investigating different compounds like other negatively and positively doped semiconductors (Si:B, Si:As) or spin glasses, we are first of all concerned with a further expanding of our parameter range to higher frequencies f, higher dopant densities n and lower temperatures T. Application of a magnetic field B is also an issue, due to a constructional possibility in the new spectrometer on the basis of a ^{3}He cryostat, which was developed as a part of the work of this thesis. The listed parameter expansion possibilities would allow to investigate the following issues of the fundamental research on Si:P and other doped semiconductors,

- Going to higher frequency would be interesting, in order to see the crossover to the non-interacting regime in a doped semiconductor in the microwave range. By now, the only sound information concerning this crossover was obtained in the terahertz range by transmission measurements using quasioptical techniques on relatively dilutely doped Si:P samples [32]-[34]. Measurements up to 40 GHz are possible with the setup of our microwave spectrometer, provided that severe complications in the calibration and evaluation procedure, which emerge at higher frequencies than reported here, could be overcome. As concerns the calibration, standing waves in the microwave line become hardly reproducible at high frequency above 20 GHz. The evaluation procedure itself can be extended beyond the limit of 5 GHz with a considerable amount of numerical work, required to cope with the higher terms of the series expansion in the crucial analytical equations and with the disturbing resonances in the sample, caused by its finite size and the rapid increase of the distance, the electromagnetic wave penetrates to, with growing frequency.

- Increasing the relative donor concentration $n_r = n/n_c$ above the value of 0.9, i.e. beyond the highest doping level reported in this thesis, we expect to observe a gradual transition from the insulating to the metallic phase

in Si:P at temperature of 1.1 K and lower. The central issue of interest here is the special regime known as *quantum critical*, which lies between the insulating and the metallic phases in the parameter space at a finite temperature $T > 0$ (for reference consult [64, 74, 75]). Only at the absolute zero of temperature, $T = 0$, the metal-insulator transition is restricted to a single value n_c of the driving parameter n, at which quantum fluctuations of a diverging size take the system between the two distinct ground states. This point is known as the Quantum Critical Point. At elevated temperature, in the regime lying above the Quantum Critical Point, the thermal energy $k_{\mathrm{B}}T$ suppresses the quantum fluctuations.

Measurement of the complex microwave ac conductivity of highly doped Si:P samples across the metal-insulator transition would yield a completely new information about the behavior of such a system in the intermediate, *quantum critical*, regime. As already mentioned above, the parameter range (ω, n, T) that we can cover with our method and technique had been hardly available before. In particular, the shape of the boundary between the insulating and the critical phases in the parameter space is an open and intriguing issue. The only predecessor information concerning it stems from the submillimeter measurements [33] with a transmission measurement technique far away from the critical donor concentration n_c.

- Measurements at lower temperature than 1.1 K are desirable to further approach the $T = 0$ metal-insulator transition. Analysis of the behavior of the system in the *quantum critical regime* can only be done at sufficiently low temperature, as long as the thermal effects can be described by the quantum thermodynamics. To determine the critical exponents and the boundary shape in the phase space of the system, the useable temperature interval for this analysis should be as broad as possible, cf. Ref. [75]. The only way to increase the suitable temperature interval in our experiment is to go to lower temperature than the base temperature of 1.1 K of the [4]He spectrometer. With the new microwave measurement insert, which I constructed and built in this work for the new spectrometer based on a [3]He cryostat with the support of the workshops [93, 94], a stable base temperature as low as 450 mK was measured and held for over 10 minutes in the first thermal tests with a completely equipped microwave insert together with a sample. My successors are completing the preparations and tests of this setup for the ultimate microwave measurements similar to those performed at the [4]He setup. For the careful low temperature calibration of a semiconducting sample measurement, the [3]He microwave insert is going to be moved out of the stationary [3]He cryostat by a mechanical mechanism, which I designed with the support of the mechanical workshop [88], without disconnecting the microwave line between the probe head and the vector

network analyzer.

- As is known from the theory, cf. for instance Ref. [2], in a magnetic field B the wave functions of the donor electrons are squeezed in the transverse direction. A sharp decrease in the overlap of the donor electron functions and, as a consequence, an exponential increase of the resistivity (magnetoresistance) are expected. This effect can be used to tune the metal-insulator transition, with the advantage of an in situ variation of the driving parameter B, in contrast to the necessity of changing the samples in order to vary the donor concentration n. Constructionally, application of a magnetic field is supported by the new spectrometer, where the ^{3}He cryostat is stationary and there is sufficient space around it for the magnetic coils.

Appendix A

Complementary sign conventions for complex-valued electric quantities

The complementary sign choice for the imaginary part of the Fourier transformed of the real-valued electrical quantities leads to a different form of all the expressions and equations that make use of the Fourier transformation. Although this formal choice does not affect the physical results of the calculations, inadvertent mixing of both sing conventions would severely distort the substantial content of all the physical expressions that would follow. Unfortunately, within the scope of problems discussed in this work, both conventions are almost equally shared in the relevant literature. To avoid possible confusion, here we state our choice and list the relevant formulae in both conventions, in comparison.

To define the sign convention, we consider the electric field $\vec{E}(x,t)$ that oscillates with frequency ω. Without loss of generality, we restrict its propagation to only one spatial dimension x and denote by E its arbitrary spatial component,

$$\text{Physics:} \qquad E(x,t) = \frac{1}{\sqrt{2\pi}} \int \widetilde{E}_{\text{ph}}(k) e^{i(kx-\omega t)} \mathrm{d}k \,, \qquad (\text{A.1})$$

$$\text{Engineering:} \qquad E(x,t) = \frac{1}{\sqrt{2\pi}} \int \widetilde{E}_{\text{eng}}(k) e^{j(\omega t-kx)} \mathrm{d}k \,. \qquad (\text{A.2})$$

We hold to the first convention for the definition of the Fourier transformed $\widetilde{E}$, in accordance with references [18], [51]-[53], which is to our experience often preferred in physics and mathematics sources. The opposite sign convention is common in engineering literature and is used in Refs. [17, 25, 54] and by the network analyzer.
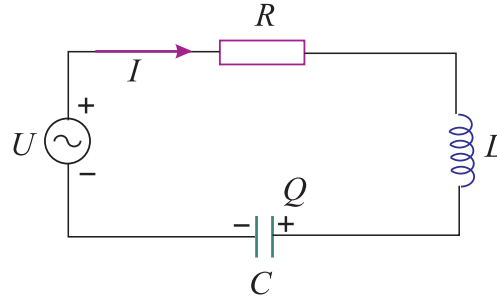
Figure A.1: Lumped-element circuit diagram of a driven electric oscillator with losses.

The basic expressions within the scope of our work, whose form depends on the sign convention, are summarized in Tab. A.1. As one already can see at the initial formulae (A.1) and (A.2), the change from the physicist to the engineering convention is easily performed by exchanging in all the expressions and equations the imaginary unity i by $-j$.

Table A.1: Comparison of the basic expressions affected by the sign convention.

expression	physics (our convention)	engineering
ideal capacitor	$Z_C = \frac{i}{\omega C}$	$Z_C = \frac{-j}{\omega C}$
ideal coil	$Z_L = -i\omega L$	$Z_L = j\omega L$
complex permittivity (SI units)	$\varepsilon = \varepsilon_0 + i\frac{\sigma}{\omega}$	$\varepsilon = \varepsilon_0 - j\frac{\sigma}{\omega}$

Both first expressions are obtained in the standard courses, see for instance Ref. [117], from the equation that gives the ac voltage U applied to the circuit of ideal lumped elements resistor R, capacitor with capacitance C and coil with inductance L, depicted in Fig. A.1,

$$U = RI + L\frac{\mathrm{d}I}{\mathrm{d}t} + \frac{Q}{C} = RI + L\frac{\mathrm{d}I}{\mathrm{d}t} + \frac{1}{C}\int I\mathrm{d}t\,, \tag{A.3}$$

where I is the ac current flowing in the circuit and Q is the charge accumulated on the capacitor plates. Denoting by U_0 and I_0 the complex valued amplitudes of voltage and current, respectively, one obtains the well-known expressions for the complex impedance $Z = U_0/I_0$ in both sign conventions,

Physics: $U = U_0 e^{-i\omega t}, I = I_0 e^{-i\omega t}$ $\Rightarrow$ $Z = R - i\omega L + \dfrac{i}{\omega C}$,

Engineering: $U = U_0 e^{j\omega t}, I = I_0 e^{j\omega t}$ $\Rightarrow$ $Z = R + j\omega L - \dfrac{j}{\omega C}$.

The sign of the imaginary part of the impedance Z directly corresponds to that of the reflection coefficient Γ via the relation (3.2). It is

$$\frac{Z}{Z_0} = \frac{1+\Gamma}{1-\Gamma} = \frac{1-(\mathrm{Re}\Gamma)^2-(\mathrm{Im}\Gamma)^2}{(1-\mathrm{Re}\Gamma)^2+(\mathrm{Im}\Gamma)^2} + i\frac{2\mathrm{Im}\Gamma}{(1-\mathrm{Re}\Gamma)^2+(\mathrm{Im}\Gamma)^2} \ . \qquad (A.4)$$

The derivation of the expression for the complex dielectric function ε can be found in Refs. [18] or [51].

Appendix B

Standard basics of microwave engineering necessary to evaluate the reflection coefficient measurements

In this Appendix we briefly recall the standard deduction of the formulae (3.1) and (3.2) as it can be found for instance in Refs. [17, 76] and in Ref. [19]. The latter gives a comprehensive description of a setup, which is parent to the spectrometer built in our group [20]. Throughout the present thesis, we denote the scattering parameter S_{11} of the two-port vector network analyzer (VNA), which stands for the reflection coefficient where radiation is generated and detected at the same port (port 1), for brevity with Γ in accordance with Ref. [17].

Because of the high frequencies (and short wavelengths), standard circuit theory with the lumped-element approach as a common tool cannot be used directly to solve microwave network problems. Circuit analysis assumes that the physical dimensions of a network are much smaller than the electrical wavelength, while microwave transmission lines may be a considerable fraction of a wavelength, or many wavelengths, in size. (In our case of a cryogenic waveguide with the length of about 1 m and the sample dimensions of a few millimeters, the frequency range of the microwave signal reaches from 45 MHz to 40 GHz, that corresponds to wavelength range from roughly 10 mm to roughly 10 m in vacuum.) In microwave engineering, then, one must begin with Maxwell's equations and their solutions. Since, however, one is often only interested in terminal quantities such as power, impedance, voltage and current, the complexity of the general field solutions and equations in those cases decreases. One usually replaces the lumped elements resistance R, capacitance C and inductance L by corresponding distributed parameters per unit length of the microwave line. Adding an additional element shunt conductance G and applying the well-known Kirchhoff's rules to a
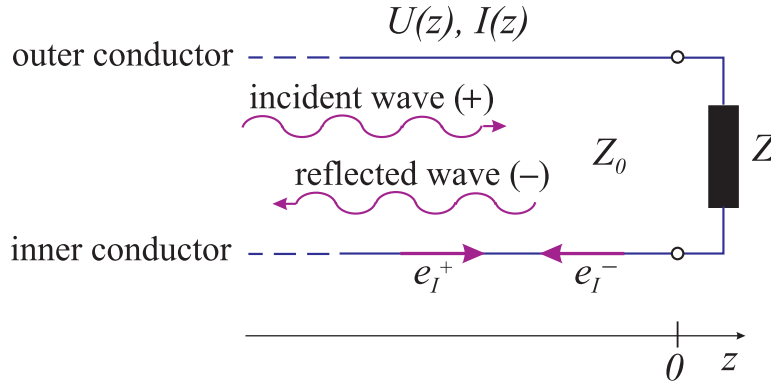
Figure B.1: Schematic diagram of a coaxial waveguide, terminated by a sample with impedance Z, after Ref. [17]. The corresponding experimental arrangement for the reflection coefficient measurement using a VNA is shown in Fig. 3.1.

representative section of such a transmission line, one obtains the so-called telegrapher equations. The other extreme of frequency can be identified as optical engineering, in which the wavelength is much shorter than the dimensions of the components and the Maxwell's equations can be simplified to the geometrical optics.

B.1 Relation between the reflection coefficient and the complex impedance of the sample

Telegrapher equations are the wave equations for current $I(z)$ and voltage $U(z)$ at an arbitrary position z along the microwave line [17]. In our case, a sample with a complex impedance Z terminates a coaxial transmission line at $z = 0$ as depicted in Fig. B.1. The solution at $z = 0$ only contains the amplitudes U_0^+, I_0^+ and U_0^-, I_0^- of the waves propagating in the positive and negative z-direction, respectively,

$$U(z = 0) = U_0^+ + U_0^- , \tag{B.1}$$

$$I(z = 0) = I_0^+ - I_0^- = \frac{U_0^+}{Z_0} - \frac{U_0^-}{Z_0} , \tag{B.2}$$

$$Z_0 = \frac{U_0^+}{I_0^+} = \frac{U_0^-}{I_0^-} = \sqrt{\frac{R - iwL}{G - iwC}} .$$

Equations (B.1) and (B.2) reveal that, while the voltages of the incident and the reflected waves are added in order to obtain the total voltage at the load impedance Z, the current value of the reflected wave I_0^- is subtracted from that of the incident wave I_0^+. In other words, while the choice of the ground reference
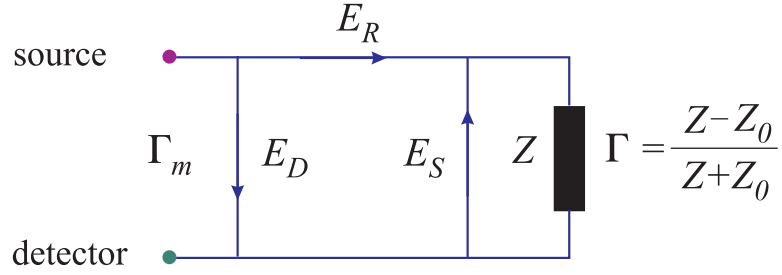
Figure B.2: General error model, cf. Ref. [19]. The measured reflection coefficient Γ_m, as it is detected by a VNA, is related to the actual reflection coefficient Γ at the sample surface via three independent complex error coefficients E_D, E_R and E_S, by which the influence of the coaxial waveguide is completely accounted for.

for the voltage (usually the outer conductor) naturally does not change with the direction of the wave propagation, the definition of the positive current direction does depend on it, as an immediate consequence of the wave equations. In our case of a coaxial waveguide with inner conductor of radius a, outer conductor of radius b and a relative dielectric constant ε_c of the dielectric between them, the characteristic impedance Z_0 of the cable can be concretely written in terms of those waveguide parameters [17],

$$Z_0 = \sqrt{\frac{\mu_0}{\varepsilon_0 \varepsilon_c}} \cdot \frac{\ln(b/a)}{2\pi} \; . \tag{B.3}$$

Here, μ_0 and ε_0 stand for the vacuum permeability and permittivity, correspondingly. To avoid any impedance mismatch, the characteristic impedance of the coaxial cables employed in the radio frequency and high frequency engineering is usually made equal to 50 Ω. This is also the case for all of our microwave components.

Put together, equations (B.1) and (B.2) yield a basic formula of the microwave engineering, that connects the reflection coefficient Γ at the surface of the sample which is terminating a general transmission line, to the complex impedance Z of the sample, cf. Eq. (3.2),

$$Z = \frac{U_0^+ + U_0^-}{U_0^+ - U_0^-} Z_0 \quad \Longrightarrow$$
$$\Gamma = \frac{U_0^-}{U_0^+} = \frac{Z - Z_0}{Z + Z_0} \; . \tag{B.4}$$

B.2 General error model for a reflection coefficient measurement

The expression for the reflection coefficient Γ of the sample given by Eq. (B.4) is valid only if the measurement is performed directly at the sample surface $z = 0$, cf. Fig. B.1. In practice, the experimentally measured reflection coefficient Γ_m will include effects of the intervening coaxial cable system and microwave connectors, such as attenuation and multiple reflections on the way, as well as errors in the detection apparatus. It turns out that those disturbing measurement effects as a whole can be described by just three general complex-valued error coefficients E_R, E_D and E_S as depicted in Fig. B.2 (for more detail see Ref. [19]),

$$\Gamma_m = E_D + \frac{E_R \Gamma}{1 - E_S \Gamma} \, . \tag{B.5}$$

The error term E_R is called the reflection tracking, and corrects principally for the attenuation and phase delay introduced by the transmission line. The error coefficient E_D is the directivity, which arises from the imperfect nature of the directional couplers and additional reflections inside the test set of the network analyzer. These effects result in a small "leakage" of the signal from the source directly into the detector, by-passing the load Z altogether. The third error term E_S is referred to as the source match, which arises due to the re-reflection of a portion of the signal at the measurement port as well as at the adapter-connector and connector-cable interfaces of the sample holder, cf. Fig. 3.1, caused by the inevitable slight impedance mismatches between microwave components. For a long transmission line made of stainless steel as in our case, cf. Sections 3.3 and 3.4, E_R serves for huge signal losses above 90 % for signal traveling between the test set and the sample. In this case additional multiple reflections at the test set are negligible, and E_S may be considered as due to re-reflections close to the sample only, cf. Fig. B.2. Taking into account that obvious consideration for E_S, we can easily deduce the formula (3.1) in our case of long and lossy microwave transmission line as follows.

We denote by U_{in} the complex voltage measured by the test set for the initial microwave signal, which enters the transmission line, and by U_{out} the voltage of the returning signal, as detected by the test set. By definition, the measured reflection coefficient is given by the quotient $\Gamma_m = U_{out} / U_{in}$, while the actual reflection coefficient Γ applies to the signal arriving at the sample, cf. Fig. B.2. We can write U_{out} in terms of U_{in} and Γ using the complex error coefficients as follows,

$$
\begin{aligned}
U_{out} &= \Gamma_m U_{in} = \left(E_D + \Gamma E_R + \Gamma E_S \Gamma E_R + ... + (\Gamma E_S)^n \Gamma E_R + ...\right) U_{in} \\
&= \left(E_D + \Gamma E_R \sum_{n=0}^{\infty} (\Gamma E_S)^n\right) U_{in} = \left(E_D + \frac{\Gamma E_R}{1 - \Gamma E_S}\right) U_{in} \qquad \text{(B.6)}
\end{aligned}
$$

The infinite sum is a converging geometrical series due to the fact, that the absolute value of both, the reflection coefficient Γ and the attenuation error coefficient E_R, is smaller than one. From (B.6), the formula (B.5) immediately follows.

Eq. (B.5) enables the calculation of the actual reflection coefficient of the sample Γ from the measured reflection coefficient Γ_m, provided that the complex error coefficients E_R, E_D and E_S of the setup are known at each frequency point of the measurement frequency range. To determine the error coefficients, three independent calibration measurements at samples with known actual reflection coefficients are required. As described in Chapter 3, the three suited calibration standards are the short, the open and the load, characterized in detail in the main text. Those calibration measurements lead to a system of three non-linear algebraic equations for the unknowns E_R, E_D and E_S,

$$
\Gamma_m^j = E_D + \frac{E_R \Gamma^j}{1 - E_S \Gamma^j}, \quad j = s(\text{short}), o(\text{open}), l(\text{load}). \qquad \text{(B.7)}
$$

while Γ_m^j and Γ^j are in general frequency-dependent complex coefficients. For the sake of convenience of the calculations to follow, at this point we rename the measured reflection coefficients Γ_m^j by M_j and the known actual reflection coefficients Γ^j by A_j. The resulting equation system in its general form,

$$
(M_j - E_D)(1 - E_S A_j) = E_R A_j, \quad j = s, o, l, \qquad \text{(B.8)}
$$

is easily solved for E_R, E_D and E_S, for instance, with the help of Maple software. The general solution for the unknown error coefficients E_R, E_D and E_S is,

$$
\begin{aligned}
Q := \quad &-M_l A_l A_s + M_l A_l A_o + M_o A_o A_s - A_o M_s A_s + A_l M_s A_s - A_l A_o M_o \,, \\
&\text{the common denomenator} \,;
\end{aligned}
$$

$$
E_S \cdot Q = -A_o M_s + A_l M_s - M_l A_s + M_o A_s - A_l M_o + M_l A_o \,,
$$

$$
\begin{aligned}
E_D \cdot Q = \quad &M_l A_s A_o M_o - M_l A_s A_o M_s - M_l A_l M_o A_s \\
&+ M_l A_l A_o M_s - A_l M_s A_o M_o + A_l M_s M_o A_s \,,
\end{aligned}
$$

$$
\begin{aligned}
E_R \cdot Q^2 \;=\; & A_l M_s M_o^2 A_s^2 - A_l^2 M_s M_o^2 A_s + M_l^2 A_l A_o^2 M_s + A_l M_s^2 A_o^2 M_o \\
& - A_l^2 M_s^2 A_o M_o + A_l^2 M_s A_o M_o^2 + A_l^2 M_s^2 M_o A_s - M_l A_l M_o^2 A_s^2 \\
& + M_l A_l^2 M_o^2 A_s - M_l A_l A_o^2 M_s^2 + M_l A_l^2 A_o M_s^2 - M_l^2 A_s^2 A_o M_o \\
& + M_l^2 A_s A_o^2 M_o + M_l A_s A_o^2 M_s^2 + M_l^2 A_s^2 A_o M_s + M_l A_s^2 A_o M_o^2 \\
& - M_s^2 A_s^2 M_o A_l - M_s A_s^2 M_o^2 A_o - M_l^2 A_o^2 M_o A_l + M_s^2 A_s^2 M_l A_l \\
& - M_s^2 A_s^2 M_l A_o + M_s^2 A_s^2 M_o A_o - M_l^2 A_l^2 M_o A_s + M_l^2 A_l^2 M_o A_o \\
& + M_l A_o^2 M_o^2 A_l - M_l A_s A_o^2 M_o^2 - M_s A_s^2 M_l^2 A_l - M_s M_o^2 A_o^2 A_l \\
& - M_s M_l^2 A_l^2 A_o - M_o A_o^2 A_s M_s^2 + M_s M_l^2 A_l^2 A_s + M_s M_o^2 A_o^2 A_s \\
& - M_l A_l^2 A_s M_s^2 - M_l A_l^2 M_o^2 A_o - M_l^2 A_s A_o^2 M_s + M_l^2 A_l M_o A_s^2 \,.
\end{aligned}
$$

This general solution for E_S, E_D and E_R takes on a significantly simpler form in cases, when at least one of the coefficients A_j can be assigned a concrete numeric value in advance, such as $A_s = \text{-}1$.

Bibliography

[1] B. I. Shklovskii and A. L. Efros, Zh. Eksp. Teor. Fiz. **81**, 406 (1981) [Sov. Phys. JETP **54**, 218 (1981)].

[2] B. I. Shklovskii and A. L. Efros, *Electronic Properties of Doped Semiconductors* (Springer, Berlin, 1984).

[3] *Electron-Electron Interactions in Disordered Systems*, edited by A. L. Efros and M. Pollak (North-Holland Physics Publishing, Amsterdam, 1985).

[4] M. Pollak, Phil. Mag. B **65**, 657 (1992).

[5] *Charge Transport in Disordered Solids with Applications in Electronics*, edited by S. Baranovski (John Wiley & Sons, Chichester, West Sussex, 2006).

[6] N. F. Mott, Festkörperprobleme **9**, 22 (1960).

[7] N. F. Mott and E. A. Davis, Phil. Mag. **17**, 1269 (1968).

[8] H. Stupp, M. Hornung, M. Lakner, O. Madel, and H. v. Löhneysen, Phys. Rev. Lett. **71**, 2634 (1993).

[9] M. Hornung, M. Iqbal, S. Waffenschmidt, and H. v. L"ohneysen, Phys. Status Solidi B **218**, 75 (2000).

[10] N. F. Mott, J. Non-Cryst. Solids. **1**, 1 (1968).

[11] N. F. Mott and E. A. Davis, *Electronic Processes in Non-Crystalline Materials*, 2nd edition (Clarendon Press, Oxford, 1979).

[12] A. L. Efros and B. I. Shklovskii, J. Phys. C **8**, L49 (1975).

[13] P. W. Anderson, Phys. Rev. **109**, 1492 (1958).

[14] *Compound Semiconductor Electronics*, edited by S. Shur (World Scientific, Singapore, 1996); *RF and Microwave Semiconductor Device Handbook*, edited by M. Golio (CRC Press, Boca Rato 2003).

[15] E. Ritz and M. Dressel, J. Appl. Phys. **103**, 084902 (2008); e-print arXiv:0712.0741 .

[16] E. Ritz and M. Dressel, Phys. Status Solidi C **5**(3), 703 (2008); e-print arXiv:0711.1256.

[17] D. M. Pozar, *Microwave Engineering*, 3rd edition (John Wiley & Sons, 2005).

[18] M. Dressel and G. Grüner, *Electrodynamics of Solids* (Cambridge University Press, Cambridge, 2002).

[19] J. C. Booth, D. H. Wu, and S. M. Anlage, Rev. Sci. Instrum. **65**, 2082 (1994).

[20] M. Scheffler and M. Dressel, Rev. Sci. Instrum. **76**, 074702 (2005); M. Scheffler, PhD thesis, Universität Stuttgart (2004).

[21] M. A. Stuchly and S. S. Stuchly, IEEE Trans. Instrum. Meas. **IM-29**, 176 (1980).

[22] J. R. Mosig, J. C. E. Besson, M. Gex-Fabry, and F. E. Gardiol, IEEE Trans. Instr. Meas. **IM-30**, 46 (1981).

[23] G. B. Gajda and S. S. Stuchly, IEEE Trans. Microwave Theory Tech. **MTT-31**, 380 (1983).

[24] L. S. Anderson, G. B. Gajda and S. S. Stuchly, IEEE Trans. Instrum. Meas. **IM-35**, 13 (1986).

[25] D. K. Misra, IEEE Trans. Microwave Theory Tech. **MTT-35**, 925 (1987).

[26] J. P. Grant, R. N. Clarke, G. T. Symm, and N. M. Spyrou, J. Phys. E: Sci. Instrum. **22**, 757 (1989).

[27] S. Fan, K. Staebell, and D. Misra, IEEE Trans. Instr. Meas. **39**, 435 (1990).

[28] G. Q. Jiang, W. H. Wong, E. Y. Raskovich, W. G. Clark, W. A. Hines, and J. Sanny, Rev. Sci. Instrum. **64**, 1614 (1993).

[29] G. Q. Jiang, W. H. Wong, E. Y. Raskovich, W. G. Clark, W. A. Hines, and J. Sanny, Rev. Sci. Instrum. **64**, 1622 (1993).

[30] S. Evans and S. C. Michelson, Meas. Sci. Technol. **6**, 1721 (1995).

[31] C. L. Pournaropoulos and D. K. Misra, Meas. Sci. Technol. **8**, 1191 (1997).

[32] E. Helgren, N. P. Armitage, and G. Grüner, Phys. Rev. Lett. **89**, 246601-1 (2002).

[33] E. Helgren, N. P. Armitage, and G. Grüner, Phys. Rev. B **69**, 014201 (2004).

[34] M. Hering, M. Scheffler, M. Dressel and H. v. Löhneysen, Phys. Rev. B **75**, 205203 (2007); M. Hering, M. Scheffler, M. Dressel, and H. v. Löhneysen, Physica B **359**, 1469 (2005).

[35] A. Miller and E. Abrahams, Phys. Rev. **120**, 745 (1960).

[36] Ch. Kittel, *Introduction to Solid State Physics*, 5th. edition, (John Wiley & Sons, New York, 1976).

[37] S. D. Baranovskii and A. A. Uzakov, Fiz. Tekh. Poluprovodn. **16**, 1026 (1982).

[38] I. Zvyagin, Chapters 1 and 9 in *Charge Transport in Disordered Solids with Applications in Electronics*, edited by S. Baranovski (John Wiley & Sons, Chichester, West Sussex, 2006).

[39] S. Baranovski and O. Rubel, Chapter 2 in *Charge Transport in Disordered Solids with Applications in Electronics*, edited by S. Baranovski (John Wiley & Sons, Chichester, West Sussex, 2006).

[40] N. F. Mott, Phil. Mag. **22**, 7 (1970).

[41] N. F. Mott, Phil. Mag. **19**, 835 (1969).

[42] J. Matulewski, S. D. Baranovskii, and P. Thomas, Phys. Status Solidi C **3**, 279 (2006).

[43] R. J. Deri and T. G. Castner, Phys. Rev. Lett. **57**, 134 (1986).

[44] M. Migliuolo and T. G. Castner, Phys. Rev. B **38**, 11593 (1988); M. Migliuolo and T. G. Castner, Solid State Commun. **67**, 863 (1988).

[45] M. Pollak, Disc. Faraday Soc. **50**, 13 (1970).

[46] S. D. Baranovskii, A. L. Efros, B. L. Gelmont, and B. I. Shklovskii, Solid State Commun. **27**, 1 (1978); J. Phys. C **12**, 1023 (1979).

[47] A. L. Efros, N. V. Lien, and B. I. Shklovskii, J. Phys. C **12**, 1869 (1979).

[48] I. Shlimak, M. Kaveh, R. Ussyshkin, V. Ginodman, S. D. Baranovski, H. Vaupel, P. Thomas, and R. W. van der Heijden, Phys. Rev. Lett. **75**, 4764 (1995).

[49] B. L. Altshuler, A. G. Aronov, Zh. Eksp. Theor. Fiz. **77**, 2028 (1979) [Sov. Phys. JETP **50**, 968 (1979)].

[50] M. Lee, J. G. Massey, V. L. Nguyen, and B. I. Shklovskii, Phys. Rev. B **60**, 1582 (1999).

[51] see, for instance, N. W. Ashcroft and N. D. Mermin *Solid State Physics*, p. 17 (Saunders College Publishing, Fort Worth, 1976).

[52] J. D. Jackson, *Classical Electrodynamics*, 3rd edition (John Wiley & Sons, New York, 1999).

[53] H. Levine and C. H. Papas, J. Appl. Phys. **22**, 29 (1951).

[54] H. C. F. Martens, J. A. Reedijk, and H. B. Brom, Rev. Sci. Instrum. **71**, 473 (2000).

[55] A. L. Efros and B. I. Shklovskii, Phys. Status Solidi B **76**, 475 (1976).

[56] W. C. Dunlap, Jr., and R. L. Watters, Phys. Rev. **92**, 1396 (1953).

[57] V. E. Dubrov, M. E. Levinshtein, and M. S. Shur, Zh. Eksp. Theor. Fiz. **70**, 2014 (1976) [Sov. Phys. JETP **43**, 1050 (1976)].

[58] J. M. Ziman, J. Phys. C: Solid St. Phys. **2**, 1230 (1969).

[59] P. W. Anderson, Comments on Solid St. Phys. **2**, 193 (1970).

[60] D. J. Thouless, Phys. Rev. C **13**, 94 (1974).

[61] A. F. Ioffe and A. R. Regel, Prog. Semicond. **4**, 237 (1960).

[62] R. Peierls, *Quantum Theory of Solids* (Clarendon, Oxford, 1955).

[63] J. M. Ziman, *Principles of the Theory of Solids*, 2nd edition (Cambridge University Press, Cambridge, 1972).

[64] S. Sachdev, *Quantum Phase Transitions* (Cambridge University Press, New York, 1999).

[65] P. G. de Gennes, P. Lafore, and J. P. Millot, J. Phys. Chem. Solids **11**, 105 (1959); J. Phys. Radium **20**, 624 (1959).

[66] J. M. Ziman, J. Phys. C: Solid St. Phys. **1**, 1532 (1968).

[67] N. F. Mott and W. D. Twose, Adv. Phys. **10**, 107 (1961).

[68] R. E. Borland, Proc. Roy. Soc. **A274**, 529 (1963).

[69] B. I. Halperin, Adv. Chem. Phys. **13**, 123 (1967).

[70] A. P. Young, J. Phys. C. **8**, L309 (1975).

[71] M. Suzuki, Prog. Theor. Phys. **56**, 1454 (1976).

[72] J. A. Hertz, Phys. Rev. B **14**, 1165 (1976).

[73] S. Chakravarty, B. I. Halperin, and D. R. Nelson, Phys. Rev. B **39**, 2344 (1989).

[74] S. Sachdev, in *Proceedings of the 19th IUPAP International Conference on Statistical Physics*, Xiamen, China, Juli 31 - August 4 1995, edited by H. Bailin (World Scientific, Singapore, 1996), [cond-mat/9508080].

[75] S. L. Sondhi, S. M. Girvin, J. P. Carini, D. Shahar, Rev. Mod. Phys. **69**, 315 (1997).

[76] *Taschenbuch der Hochfrequenztechnik*, edited by K. Lange and K.-H. Löcherer (Springer-Verlag, Berlin, 1992).

[77] In literature (e.g., [19]), a simplified formula can be found that follows from the equation (3.6) if ε_0 is neglected and the sign of the imaginary part of Z_S is defined in a different way according to the complementary sign convention $\exp[i(\omega t - \vec{k}\vec{x})]$ in the exponent of the Fourier transformed of the electromagnetic fields (cf. [103]).

[78] M. Lee and M. L. Stutzmann, Phys. Rev. Lett. **87**, 056402 (2001).

[79] F. Pobell, *Matter and Methods at Low Temperatures*, 2nd edition (Springer-Verlag, Berlin, 1996).

[80] Cernox$^{\text{TM}}$ thin film resistance temperature sensor by LakeShore. For the ^{4}He-environment with temperature down to 1 K, the type CX-1050-AA was employed, with dimensions 3 mm dia. x 8.5 mm long.

[81] UT 85C-TP-LL by Rosenberger Micro-Coax; center conductor SPC (Silver-Plated Copper), diam. 0.574 mm; outer conductor Copper, inner diam. 1.676 mm, outer diam. 2.197 mm; LL stands for low density, and, thus, low-loss dielectric LD PTFE. For further information consult Ref. [84].

[82] UT 85-B-SS by Rosenberger Micro-Coax; center conductor SPBeCu (Silver-Plated BeCu), diam. 0.51 mm; outer conductor SS 304 (stainless steel), inner diam. 1.68 mm, outer diam. 2.2 mm. Special order product.

[83] O. V. Lounasmaa, *Experimental Principles and Methods Below 1 K* (Academic Press, London and New York, 1974).

[84] Micro-Coax[R] Catalog, *Semi-Rigid Coaxial Cable*, by Rosenberger Micro-Coax, Berkshire, England.

[85] UT 85-SS by Micro-Coax; center conductor SPCW (silvered copper-covered steel, known as Silver-Plated Copper-Weld), diam. 0.51 mm; outer conductor SS 304 (stainless steel), inner diam. 1.68 mm, outer diam. 2.2 mm. For further information consult Ref. [84].

[86] UT 85-B-B by Micro-Coax; center conductor SPBeCu (Silver-Plated BeCu), diam. 0.51 mm; outer conductor BeCu, inner diam. 1.68 mm, outer diam. 2.2 mm. For further information consult Ref. [84].

[87] Microwave connector OS-50, Type 8502-7885-02, M/A-COM, distributed by AMP Incorporated. Microwave adapter RPC-2.40, Type 09S121-K00S3; RPC-1.85 Type 08S121-K00S3, Rosenberger Hochfrequenztechnik GmbH.

[88] with support of the foreman Markus Neuwirth of the mechanical workshop of the University Stuttgart.

[89] Brazing flux 157 N, Castolin GmbH. Solder for stainless steel Castolin 157, *Sonderweichlot für Eisen- und Kupferwerkstoffe (insb. für nichtrostende Stähle geeignet)*, Castolin GmbH. Norm L-SnAg 5 DIN 1707.

[90] with support of the foreman Jochen Brenner of the mechanical workshop of the University Stuttgart.

[91] M. Welte, *Spektrale Eigenschaften supraleitender Aluminiumtunneldioden als Phononengeneratoren und -detektoren*, Dissertation, Universität Stuttgart, 1976.

[92] F. Maier, *Phononenspektroskopie an GaAs:O*, Dissertation, Universität Stuttgart, 1999.

[93] with constructional advice and support of the foreman Günter Dietrich of the mechanical workshop of the University Stuttgart.

[94] with constructional advice and support of the foreman Jürgen Maurer of the low-temperature workshop of the University Stuttgart.

[95] *Matter and Methods at Low Temperatures*, edited by R. C. Richardson and E. N. Smith (Key-Westview, 1998).

[96] elastic contact stripes, Kontaktfederstreifen, Feuerherdt GmbH.

[97] elastic metallic spring sealing, Federelastische Metalldichtung *Helicoflex* Typ HN 100, Ummantelung: Aluminium, Feder: Nimonic 90 (H), Garlock Sealing Technologies.

[98] Microwave connectors RPC-2.40, Types 09S121-271S3 and 09K121-271S3, Rosenberger Hochfrequenztechnik GmbH.

[99] Model 370 AC Resistance Bridge with Temperature Control by LakeShore. With 21 excitation levels from 3.16 pA to 31.6 mA for the temperature sensors and unique noise-reduction elements, this device has been selected as best suited for the microwave spectrometer, based on the ^{3}He-bath cryostat.

[100] Cernox^{TM} thin film resistance temperature sensor by LakeShore. For the ^{3}He-environment with temperature down to 0.3 K, the type CX-1030-AA was employed, with dimensions 3 mm dia. x 8.5 mm long. The commercially calibrated one is called CX-1030-AA-0.3L, calibrated from 0.3 K to 325 K by LakeShore.

[101] The variational approximation applied by Levine and Papas [53] leads to a vanishing contribution of the integral terms corresponding to the evanescent higher order terms of the electromagnetic wave inside the coaxial sensor. The parameter range, where the corresponding uncertainty in the resulting capacitances is below 1%, as proved by Levine and Papas, includes our range of frequency and dielectric function. Moreover, Misra [25] has critically compared the method with the results obtained by Mosig [22] under consideration of higher order modes, yielding a parameter range where the variational approximation is justified.

[102] For effectively smaller samples, a full wave treatment considered by Martens *et al.* [54] is necessary, which takes secondary reflections at the sample back into account.

[103] We hold to the convention $\exp[i(\vec{k}\vec{x} - \omega t)]$ in the integrand of the Fourier transformed of the electromagnetic field in accordance with Refs. [18], [51]-[53]. The opposite sign convention is used in Refs. [17, 25, 54] and by the network analyzer. For detailed comparison of both sign conventions see Appendix A.

[104] J. Galejs, *Antennas in Inhomogeneous Media* (Pergamon Press, Oxford, 1969).

[105] Micro-Coax data on the solid polytetrafluoroethylene as a dielectric of the semirigid cable UT 085B-SS [85], at frequency of 1 GHz, $\varepsilon = 2.03(1 + i0.0002)$.

[106] Single Si:P crystal, grown by Société Générale Métallurgique de Hoboken by a Czochralski technique and provided by D. Schweitzer.

[107] Y. Ootuka, F. Komori, Y. Monden, S. Kobayashi, and W. Sasaki, Solid State Commun. **36**, 827 (1980).

[108] preparation of all the samples mentioned in this thesis has been performed by the technical assistant Gabriele Untereiner of the 1. Physikalisches Institut, University Stuttgart.

[109] Anung W. A., Master thesis, Universität Stuttgart (2003).

[110] M. Hering, Diploma thesis, Universität Karlsruhe (TH) und Universität Stuttgart (2004).

[111] W. R. Thurber, R. L. Mattis, Y. M. Liu, and J. J. Filliben, J. Elechtrochem. Soc. **127**, 1807 (1980).

[112] H. Stupp, Diploma thesis, Universität Karlsruhe (TH) (1992).

[113] M. Hornung, Diploma thesis, Universität Karlsruhe (TH) (1993).

[114] I. G. Austin and N. F. Mott, Adv. Phys. **18**, 41 (1969).

[115] M. Pollak and T. H. Geballe, Phys. Rev. **122**, 1742 (1961).

[116] see, for instance, H. W. Bode, *Network Analysis and Feedback Amplifiers Design*, p. 314 (D. Van Nostrand Company, Inc., Princeton, New Jersey, 1945).

[117] W. Greiner, *Klassische Elektrodynamik*, 5. Auflage (Verlag Harry Deutsch, Frankfurt am Main, 1991).

Kurzfassung

Si:P begegnet einem oft als akademisches Beispiel für einen negativ dotierten Halbleiter und ist als Material für die Elektronikindustrie unentbehrlich. Dennoch gibt es für die Grundlagenforschung an Si:P und verwandten Systemen immer noch offene Diskussionen über die niederenergetischen Anregungen aus dem Grundzustand. Kristallines Silizium, unterschiedlich stark dotiert mit Phosphor mit etablierten Methoden, ist ein beliebtes Objekt für die Forschung auf dem Gebiet der ungeordneten Festkörper. Insbesondere hat der Einfluß der Elektronenwechselwirkung auf die elektrische Hüpfleitfähigkeit in dotierten Halbleitern bei tiefen Temperaturen nahe des absoluten Nullpunkts seit Jahrzehnten viel Aufmerksamkeit auf sich gezogen [1]-[5]. Neben den Korrelationseffekten ist auch das kritische Verhalten in der der Nähe des Metall-Isolator-Übergangs (MIT) bei $T \rightarrow 0$ ein wichtiges Thema in der Physik ungeordneter Festkörper [6, 7]. Sogar in klar definierten Systemen wie den hoch dotierten Halbleitern, wo die Unordnung von der statistischen Verteilung der Donatoren (oder der Akzeptoren) mit der Konzentration n in dem Wirtskristall stammt, ist das Verhalten der komplexwertigen elektrischen Leitfähigkeit σ kaum verstanden, wenn man in die Nähe der kritischen Dotierungskonzentration n_c des Metall-Isolator-Übergangs kommt. Die Gleichstromleitfähigkeit σ_{dc} von dotierten Halbleitern ist gut dokumentiert auf der isolierenden Seite des MIT [8, 9]. Die temperaturabhängige Gleichstromleitfähigkeit ist für $n < n_c$ beobachtet, den Gesetzabhängigkeiten für das Variable-Range-Hopping $\sigma_{\mathrm{dc}}(T) = \sigma_0 \exp[-(T_0/T)^m]$ zu folgen, wo der Exponent m gleich 1/4 nach der Vorhersage durch Mott [10, 11] für nicht wechselwirkende Elektronen und gleich 1/2 nach Efros und Shklovskii [2, 12] bei Berücksichtigung der weitreichenden Coulomb-Wechselwirkung ist. Die frequenzabhängige Leitfähigkeit $\sigma(\omega)$ der isolierenden dotierten Halbleiter ist allerdings noch nicht vollständig verstanden, und mit diesem faszinierenden Thema haben wir uns in dieser Arbeit[1] befasst.

Bei Phosphorkonzentrationen in Silizium unter dem kritischen Wert von $n_c = 3.5 \times 10^{18}$ cm^{-3} [8] sind die Elektronenzustände der Dotierungselektronen lokalisiert im Sinne von Anderson durch die Unordnung [2, 6, 11, 13] (im Gegensatz zu

---

[1]Teile dieser Dissertation sind bereits veröffentlicht in unseren Publikationen in the Journal of Applied Physics [15] und in the Physica Status Solidi C [16].

den ausgedehnten Bloch-Zuständen, die typisch für ein periodisches Atomgitter sind). Dies führt zu dem isolierenden Verhalten, definiert durch die verschwindende Gleichstromleitfähigkeit $\sigma_{dc}(T \to 0) = 0$ bei der Annäherung an den Temperaturnullpunkt. Für solch ein System haben die theoretischen Modelle in den letzten Jahrzehnten zu bedeutsamen analytischen Formeln für die frequenzabhängige Antwort $\sigma(\omega)$ bei $T \to 0$ geführt [1, 2, 3, 5]. Verglichen mit der durchgeführten theoretischen Arbeit, bleiben die experimentellen Daten zu der dynamischen Leitfähigkeit der isolierenden dotierten Halbleiter allerdings knapp und die Ergebnisse, die in verschiedenen Gruppen und in verschiedenen Parameterbereichen erhalten wurden, sind widersprüchlig. Besonders ist der Mikrowellenbereich (mit der Frequenz der elektromagnetischen Strahlung von 100 Megahertz bis 100 Gigahertz entsprechend der Wellenlänge von 10 mm bis 10 m), bestens geeignet für die Untersuchungen der Coulomb-Wechselwirkung der Ladungsträger, ist schwer zu erreichen in einem Experiment, wo die dynamische Antwortfunktion $\sigma(\omega)$ bei tiefen Temperaturen bestimmt werden soll. Lange Zeit gab es keine besseren Mittel als die Resonatortechnik (eine präzise Methode, allerdings beschränkt auf die bestimmte Resonanzfrequenz des verwendeten Resonators), um die frequenzabhängige Leitfähigkeit $\sigma(\omega)$ von dotierten Halbleitern im Gigahertzbereich zu messen. Für jeden Messpunkt benötigte man einen weiteren Resonator.

Abgesehen von der Grundlagenforschung, fordert auch die rasche Entwicklung der industriellen, medizinischen und der Kommunikationstechnologien eine akkurate Charakterisierung der Komponenten bei immer höheren Frequenzen, über den weitgehend erforschten Radiofrequenzbereich hinaus, der bis zu 1 MHz reicht. Dies betrifft insbesondere die isolierenden und halbleitenden Werkstoffe [5, 14], die in elektronischen Geräten und rauscharmen Sensoren verwendet werden, die bei tiefen Temperaturen betrieben werden. Auf der makroskopischen Skala und unter den Gleichgewichtsbedingungen ist die Wechselwirkung eines Materials mit dem elektrischen Feld definiert durch die elektrische Leitfähigkeit σ_1 und die dielektrische Permittivität ε_1, beide zusammengefasst in einer komplexwertigen Gröse $\sigma = \sigma_1 + i\sigma_2$ (alternativ $\varepsilon = \varepsilon_1 + i\varepsilon_2$) durch die Gl. (2.16). Die gewünschte breitbandige Charakterisierung dieser Parameter wird zu einer Herausforderung mit steigender Frequenz, weil dann die Verluste und die räumliche Variation von Strom und Spannung an Bedeutung gewinnen.

Im Mikrowellenbereich ist die Wellenlänge vergleichbar mit den Abmessungen der elektrischen Leitungen und der Proben; Wellenleiter müssen verwendet werden, wie in der Abb. 1.1 gezeigt, und der Reflexionskoeffizient wird gemessen [17]. Das passende Messgerät in diesem Frequenzbereich ist der Vektornetzwerkanalysator (VNA). Er erlaubt phasensensitive Messungen des Reflexionskoeffizienten Γ, der durch eine direkte Beziehung (3.2) mit der complexen Impedanz Z der Probe zusammenhängt (unter der Voraussetzung, dass die Mikrowellenleitung korrekt

kalibriert ist). Während die Auswertung der interessanten Materialparameter, d.h. der komplexwertigen Leitfähigkeit σ, aus den gemessenen Impedanzdaten Z relativ einfach für Metalle und Supraleiter ist [18]-[20], ist im Fall isolierender Proben keine direkte Lösung für dieses Problem möglich. Diese ernsthafte Komplikation liegt an einer nicht trivialen Verteilung des elektromagnetischen Vektorfeldes innerhalb einer isolierenden Probe, die einen Coaxialleiter elektrisch abschließt. Dies is in der Abb. 1.1 für eine halbleitende Probe demonstriert. Nur Näherungslösungen und Modelle wurden in der Vergangenheit zur Untersuchung von dielektrischen Substanzen entwickelt [21]-[31], in den meisten Fällen für Flüssigkeiten und weiche Stoffe bei Raumtemperatur.

Als Ergebnis konnte die leistungsfähige Technik der Messung des komplexwertigen Reflexionskoeffitienten im Gigahertzbereich mit einem Vektornetzwerkanalysator bisher zur Bestimmung der komplexwertigen Leitfähigkeit $\sigma(\omega)$ der Festkörper bei tiefen Temperaturen nur im Fall von Metallen und Supraleitern erfolgreich angewendet werden, während die komplizierte Stromverteilung in einer isolierenden halbleitenden Probe die entsprechende Datenauswertung verhinderte. Im Laufe der Arbeit an dieser Dissertation haben wir die bereits existierenden Betrachtungsweisen zu den verwandten sowie zu den komplementären Problemen analysiert und eine abgeschlossene und rigorose Methode zur Auswertung solcher Messungen an isolierenden Halbleitern ausgearbeitet, mit einem optimierten theoretischen und experimentellen Aufwand [15].

Dieses unser wichtigstes methodisches Ergebnis ist im Kapitel 4 dargestellt. Ein einfaches statisches Modell für die Stromverteilung in einer halbleitenden Probe, das wir als ersten Versuch entwickelt haben und das sich später als korrekt bei niedrigen Frequenzen bis zu 1 GHz erwiesen hat, ist im Abschnitt 4.1 beschrieben. In den darauffolgenden Abschnitten 4.2 und 4.3 folgt die rigorose Lösung des Problems, wobei wir keine großen Vereinfachungen in einem streng definierten Parameterbereich machen.

Wir haben diese entwickelte Auswertungsmethode zum Studium der komplexwertigen dynamischen Hüpfleitfähigkeit $\sigma(\omega)$ des dotierten Halbleiters Si:P in einem breitbandigen Frequenzbereich von 0.1 bis 5 GHz bei Temperaturen von 1.1 K und höher mit Dotierungskonzentrationen n von 0.56 bis 0.9 relativ zu der kritischen Konzentration $n_c = 3.5 \times 10^{18}$ cm^{-3} des Metall-Isolator-Übergangs angewandt [16]. Die entsprechenden experimentellen Ergebnisse sind im Kapitel 5 besprochen.

Mit diesen Messungen haben wir folgende Ergebnisse zu einigen offenen fundamentalen Fragestellungen über Si:P erzielt [16]:

1. Für alle berichteten Si:P-Proben wurde bei unserer tiefsten Messtemperatur von 1.1 K das phononenfreie (d.h. temperaturunabhängige) Regime identi-

fiziert. Somit konnte der Einfluß der weitreichenden Coulomb-Wechselwirkung $U(r_\omega)$ auf die dynamische Hüpfleitfähigkeit $\sigma_1(\omega, n, T)$ im System lokalisierter Dotierungselektronen mit Anregung nur durch die Photonen untersucht werden. Die Korrelationseffekte sind in dem Exponenten α der frequenzabhängigen Hüpfleitfähigkeit $\sigma_1(\omega) \sim \omega^\alpha$ kodiert, siehe das Theoriekapitel. Aus der supralinearen Frequenzabhängigkeit, die an allen berichteten Si:P-Proben bei 1.1 K beobachtet wurde, schließen wir, dass der Ladungstransport im genannten Parameterintervall durch wechselwirkende Elektronen innerhalb der Coulomb-Lücke stattfindet.

2. Die dielektrische Funktion $\varepsilon_1(\omega, n)$ aller berichteten Si:P-Proben ist als unabhängig von der Frequenz f der Mikrowellenstrahlung und von der Temperatur T bei 1.1 K befunden worden, mit Berücksichtigung unserer Messgenauigkeit. Für die entsprechenden Werte $\varepsilon_1(n)$ der dielektrischen Konstanten bei 1.1 K ist ein rascher Anstieg mit wachsender Dotierungskonzentration beobachtet worden. Der Beitrag durch die Dotierungselektronen ($\varepsilon_1 - \varepsilon_{\mathrm{Si}}$) folgt einem Skalierungsgesetz $|n - n_c|^{-\zeta}$ mit dem Exponenten $\zeta = 0.71$ aus unserem Experimet. Dies entspricht auch der Erwartung, denn der Beitrag der Dotierungselektronen zu der dielektrischen Relaxation sollte mit steigender Dotierung wachsen.

3. Der Exponent α des Potenzgesetzes der dynamischen Leitfähigkeit fällt mit steigender Temperatur T für alle berichteten Si:P-Proben ab, sobald das phononenfreie Regime für die jeweiligen Dotierungskonzentration n verlassen wird. Die Art, wie die Spektren $\sigma_1(\omega, n, T)$ mit steigender Temperatur ansteigen, ist die gleiche für alle gemessenen Si:P-Proben, mit dem einzigen Unterschied, dass für niedrigere Dotierung n die thermischen Effekte bei einer höheren Temperatur einsetzen. Während die sublineare Frequenzabhängigkeit der Hüpfleitfähigkeit σ_1 in einem durch Phononen unterstützten Regime auch von der Theorie vorhegesagt ist, ist eine theoretische Beschreibung für eine monotone Abnahme des Potenzgesetzes der dynamischen Leitfähigkeit mit steigender Temperatur nach unserer Kenntnis nicht vorhanden. Vorhandene theoretische Vorhersagen beziehen sich lediglich auf die einzelnen Grenzfälle der Parameter Temperatur T und Frequenz f, während wir in unserem Experiment ein breites Parameterintervall (ω, n, T) abgedeckt haben. Qualitativ erscheint uns das beschriebene Verhalten der Spektren $\sigma_1(\omega, n, T)$ von Si:P als plausibel: Mit steigender Temperatur T wird die Frequenzabhängigkeit der Leitfähigkeit allmählich schwächer wegen der wachsenden Rolle der thermischen Energie $k_{\mathrm{B}}T$ im Vergleich zu der Photonenergie $\hbar\omega$.

Ähnlich zu der Leitfähigkeit $\sigma_1(\omega, n, T)$, steigen die Spektren der dielektrischen Funktion $\varepsilon_1(\omega, n, T)$ mit wachsender Temperatur T an, sobald das

phononenfreie Regime verlassen wird. Die Art, wie sich die Spektren mit der Temperatur verändern, ist erneut qualitativ gleich für alle gemessenen Si:P-Proben. Die Frequenzabhängigkeit der dielektrischen Funktion ε_1 ist im Einklang mit der des Realteils σ_1 der Leitfähigkeit, was die Kramers-Kronig-Retationen zwischen dem Real- und dem Imaginärteil der komplexwertigen Antwortfunktion $\sigma = \sigma_1 + i\sigma_2$ betrifft.

Versicherung

Ich erkläre: Ich habe die vorgelegte Dissertation selbständig und ohne uner-
laubte fremde Hilfe und nur mit den Hilfen angefertigt, die ich in der Dissertation
angegeben habe.
Alle Textstellen, die wörtlich oder sinngemäß aus veröffentlichten Schriften ent-
nommen sind, und alle Angaben, die auf mündlichen Auskünften beruhen, sind
als solche kenntlich gemacht.
Bei den von mir durchgeführten und in der Dissertation erwähnten Untersuchun-
gen habe ich die Grundsätze guter wissenschaftlicher Praxis, wie sie in der "Satzung
der Justus-Liebig-Universität Gießen zur Sicherung guter wissenschaftlicher Praxis"
niedergelegt sind, eingehalten.

Gießen, den 17. März 2009

Elvira Ritz